A Ray Tracing Study of VLF Phenomena

W.K.M.Rice

Submitted in partial fulfilment of the
requirements for the degree of
Doctor of Philosophy
in the
Space Physics Research Institute,
Department of Physics,
University of Natal

Durban
South Africa
December 1997

Acknowledgements

The author wishes to thank the following people without whose help this project would not have been completed:

- My Supervisor, Prof. A.R.W.Hughes, for all his guidance, counsel and friendship and for sending me to some of the most interesting places in the world.
- Mr. Willem de Beer and all the staff of the mechanical and electronic workshop for their assistance and support.
- Dr. Mark Clilverd, British Antarctic Survey, for his collaboration on the Marion Island campaign, for allowing me to use the VLF Doppler data and for all his suggestions and advice.
- Dr. Erhard Mravlag for all his help and advice.
- Members of S.P.R.I. for their friendship and for making it a fun and enjoyable workplace.
- Duncan and Jeanette for all they have done for me and for allowing me to marry their daughter.
- My parents for having faith in my abilities and for supporting me through all my endeavours.
- Last, but definitely not least, my wife Paula for all her patience and encouragement.

Abstract

Whistlers have, for many years, been used as probes of the ionosphere and magnetosphere. Whistlers received on the ground have been shown (Smith [1961], Helliwell [1965]) to have propagated, in almost all cases, through ducts of enhanced ionisation aligned along the magnetic field direction. Analysis of these whistlers, using for example the Ho and Bernard [1973] method, allows determination of the L-value of the field line along which the signal has propagated, the equatorial electron density and the time of the initiating lightning strike.

Satellite received whistlers, known as fractional-hop whistlers, are not restricted to propagating through ducts and, in this case, ducted whistlers are probably rarer than unducted whistlers. Analysis of these whistlers is consequently much more difficult as the propagation path is often not known. This study is an attempt to understand some of the characteristics of whistlers received on the ISIS2 satellite at low latitudes during October 1976.

Haselgrove's [1954] ray tracing equations, together with realistic density and magnetic field models, have been used to determine the ray paths and travel times. The whistler dispersions, calculated from the travel times, are compared with the results obtained from analysis of the ISIS2 data. Values given by the density models used were also compared with density values obtained from other models and values recorded by ionosondes during the same period and at locations close to the latitude and longitude of the ISIS2 satellite.

Another part of this study considers the cyclotron resonance interaction between ducted whistler mode waves and energetic electrons. During this interaction, electrons can diffuse into the loss cone and will then precipitate into the upper atmosphere causing secondary ionisation. This ionisation patch modifies the earth-ionosphere wave guide and can be observed as phase and/or amplitude perturbations on VLF transmitter signals, known as Trimpi events (Helliwell et al [1973], Dowden and Adams [1988], Inan and Carpenter [1987]).

Trimpi events and associated whistlers were observed at Marion Island ($46^{o}53"S$, $37^{o}52"E$, $L = 2.63$) during May 1996. Analysis of the associated whistler groups confirms that the Trimpi events can be explained by the above mentioned cyclotron resonance interaction and subsequent electron precipitation. During this process the whistlers were propagating towards Marion Island while the electrons were propagating away. The electrons must therefore have mirrored in the northern hemisphere before precipitating near Marion Island causing the observed Trimpi. The calculated time delays are shown to confirm this process.

During the unusual 2-hour period of observation, the Trimpi associated whistler groups were, in all cases, followed by a second, fainter whistler group which has

been called a whistler 'ghost'. The dispersion of whistlers within this second whistler group are shown to be the same as those within the initial whistler group indicating that these whistlers must have propagated through common ducts at different times and hence must have been caused by different atmospheric discharges. It is thought that during the wave-particle interaction, which caused the observed Trimpi, some of the energetic electrons may have precipitated into the northern hemipshere triggering this second discharge. The timing between the two whistler groups is such that, if the above triggering is correct, the interaction must have taken place about 10^{o} from the equatorial plane.

Contents

List of Figures

Chapter 1

Introduction

1.1 Ionosphere and Magnetosphere

The ionosphere and magnetosphere are the regions immediately surrounding the earth. There is no clear distinction between the two regions with the ionosphere regarded as being the region where the plasma dominates and the magnetosphere the region where the magnetic field dominates. The ionosphere extends from an altitude of about 100 km to an altitude of about 1000 km and the magnetosphere extends from the top of the ionosphere to the magnetopause.

The magnetopause is the outer boundary of the magnetosphere and is formed by the interaction between the solar wind and the earth's magnetosphere. On the sunward side, the magnetosphere is compressed to a thickness of about 10 earth radii. On the anti-sunward side the earth's magnetic field line's are frozen in to the plasma and are dragged by the solar wind into a long tail that may extend hundreds of earth radii.

Within the magnetosphere there are also electric fields. Two of these are the corotation electric field and the convection electric field. In the inner magnetosphere and ionosphere the corotation electric field dominates and the plasma rotates with the earth. In the outer magnetosphere the convection electric field dominates and the plasma takes part in general magnetospheric convection.

At the boundary between the two regions, known as the plasmapause, the plasma density drops by $1-2$ orders of magnitude. All of the phenomena discussed in this thesis are related to conditions and events within the plasmasphere. Figure 1.1 shows the earth's magnetosphere and illustrates all the regions discussed above.

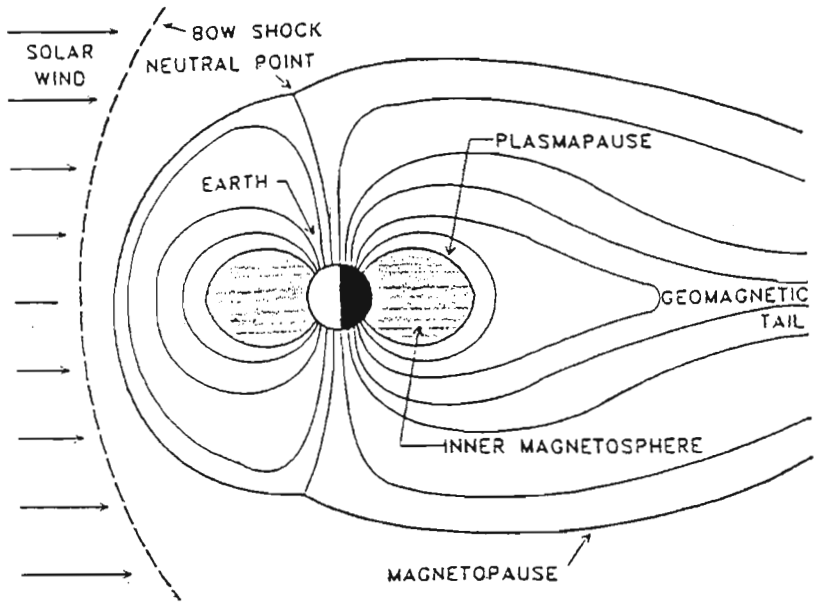

Figure 1.1: The earth's magnetosphere

1.2 Whistlers

Whistlers are radio waves in the audio frequency band (30 Hz−30 kHz) that, when converted to sound waves by an audio amplifier, sound like a whistle. They are generated when energy from a lightning discharge, or spheric, enters the ionosphere and is guided through the magnetosphere by the earth's magnetic field. The magnetosphere is a dispersive medium and when the signal is received, different frequencies arrive at different times resulting in the whistling sound. Although the term whistlers generally refers to natural whistlers, any wave with a frequency below the electron gyrofrequency and above the ion gyrofrequencies will propagate through the ionosphere and magnetosphere in the whistler mode. VLF transmitter signals are examples of such waves.

Whistlers were possibly first reported by Preece [1894]. Barkhausen [1919] reported noises that were unmistakably whistlers after hearing them on telephone lines during World War I. Eckersley [1935] showed that they are produced by the dispersion of natural radio waves from lightning, propagating in the mode below the electron gyrofrequency. Storey [1953] found that their ray paths follow the lines of the earth's magnetic field and that the electron density in near earth space needed to be much higher than previously expected in order to explain the dispersion. This was the first evidence of the existence of the magnetosphere. Whistlers have, since then, been used as probes for determining electron density profiles in the magnetosphere (Carpenter et al [1972], Park [1972], Sagredo et al [1973]) and sometimes also to measure electric fields by following the drifting of whistler ducts.

The use of whistlers in analysing the magnetosphere was further enhanced by the discovery of the nose whistler (Helliwell [1956]). The nose whistler has a frequency, known as the nose frequency, at which the travel time is a minimum and which is strongly dependent on the whistler path. The knee whistler discovered by Carpenter [1963], a nose whistler with a much smaller travel time than expected, led to the discovery of the plasmapause.

Most of the lightning energy that enters the ionosphere is only partially guided by the earth's magnetic field. The fact that energy from a single lightning discharge follows discrete paths through the magnetosphere suggests that whistlers observed on the ground are guided by ducts (Smith [1961], Helliwell [1965]). Theory shows that below the half-gyrofrequency these must be ducts of enhanced ionisation. It is, however, also thought that whistlers propagating in the pro-longitudinal (PL) mode (Thomson [1977]) may also be observed on the ground.

Figure 1.2 is a spectrogram of a whistler group received at the South African National Antarctic Expedition (SANAE) base in 1994. The frequency range is from 0 kHz−10 kHz, the time is 5 s and each spectra lasts 10 ms. All of these parameters are variable depending on the time scales and frequency ranges of interest. In figure 1.2 the discreteness of the whistler traces is clearly visible, indicating the multi path propagation. The nose frequency can also be seen on the later whistlers in the group.

1.2.1 Low Latitude Whistlers

At low magnetic latitudes it is more difficult for whistlers to be trapped by ducts because the refraction of the waves on entering the ionosphere results in a large angle between the wave normal and the magnetic field direction, along which the ducts are aligned. Cerisier [1973] studied whistlers received on the FR-1 satellite and found evidence of both ducted and unducted propagation above $L = 1.7$ but found only unducted propagation below $L = 1.7$. Hayakawa et al [1985], by studying the ionospheric exit points of many low latitude whistlers, showed that whistlers received on the ground at low latitudes are probably ducted. Ondoh [1979] showed that ducted propagation may be possible at low latitudes by using an IGRF field model in his ray tracing calculations. Singh and Tantry [1973] and Tanaka and Hayakawa [1985] showed that the excitation of ducts at low latitudes may require density enhancements of 100% or more. Hayakawa and Iwai [1975] showed that such enhancements may exist during sunset. Tanaka and Hayakawa [1973] suggested that waves could be trapped in ducts with enhancements of a few tens of percent if the wave normal was tilted favourably at the duct entrance. Andrews [1978] and Thomson [1987], studying whistler mode signals from VLF transmitters, suggested that certain discrete, non ducted paths, that allow the

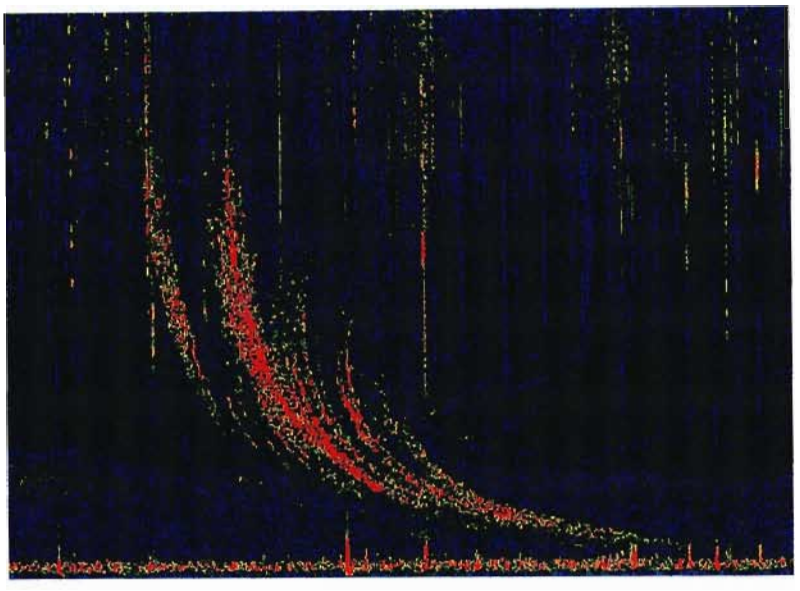

Figure 1.2: Spectrogram showing multi path whistlers. Frequency, on the y-axis, is from 0 kHz to 10 kHz and time, on the x-axis, is 5 s. The nose frequency can clearly be seen on the later whistlers.

wave to reenter the earth's atmosphere, may exist. Tanaka and Cairo [1980] also suggested that negative density gradients due to the equatorial anomaly may be involved in guiding whistlers observed on the ground.

The whistlers discussed above, which exist below the electron gyrofrequency, should, more correctly, be called electron whistlers. Below each of the ion gyrofrequencies 'ion' whistlers exist and can be observed on satellites but not on the ground. These 'ion' whistlers can be used to determine the local ion gyrofrequencies, by measuring their maximum frequency, and the ion concentrations, by measuring the crossover frequency (Gurnett et al [1965]).

The problems associated with whistlers observed on the ground at low latitudes makes satellite observations very useful. Whistlers observed on satellites may be ducted or unducted. Hayakawa and Tanaka [1978] in their review of the work on low latitude whistlers conclude that ducted whistlers represent only a small proportion of those observed on satellites. Sonwalker et al [1984] observed pulse stretching on VLF transmitter signals received on the ISEE 1 satellite and showed how this could be explained by multi path propagation of nonducted VLF waves. Observation of 'ion' whistlers also allows determination of the local ion concentrations and the local ion gyrofrequencies.

This thesis will attempt to understand some of the characteristics of whistlers

observed on the ISIS2 satellite during October 1976 (Hughes [1981] and Hughes and Rice [1997]) by ray tracing unducted signals through realistic density and magnetic field models. Hughes [1981] observed whistler dispersions which seemed to indicate that direct signals from both hemispheres and echoes were received on the satellite. The dispersions calculated by ray tracing signals from the ground to the satellite are compared with those obtained by analysis of the ISIS2 data. The satellite observations were made over a latitude range of between 30° and 0°. The density model was chosen such that the results obtained through ray tracing match those obtained from analysis of the satellite data at all of these latitudes and in all cases. Unducted whistlers are not constrained to propagate along the magnetic field direction and hence it is thought that unducted whistlers may give information regarding the density profile and latitudinal gradients that may be difficult to obtain from ducted signals. An advantage of satellite observations is that the whistlers are received over a large latitudinal range and not only at a single point.

This study was initially prompted by the idea that the position of the lightning source on the ground may be deduced from the whistler observed on the satellite. This would complement the optical studies of lightning which are hindered by, for example, cloud cover.

1.3 Energetic Particles

The plasma densities determined by whistler analysis are known as the background plasma or the cold plasma densities. Although not actually a cold plasma, the distribution function describing the plasma can be approximated by a delta function without introducing any significant errors. Data collected on the Explorer I satellite in 1958 allowed Van Allen [1959] to discover energetic trapped particles within the plasmapause. These particles consist of protons and electrons with energies of a few tens of keV to over 30 MeV. When mapped in terms of energy, these particles are shown to exist in particular bands known as the Van Allen belts with the lower energy particles almost continuous within the plasmasphere. These particle populations vary with magnetic activity and indeed their presence modifies the earth's magnetic field.

1.3.1 Whistler Induced Electron Precipitation

These energetic particles are trapped by the earth's magnetic field and both bounce back and forth along the earth's field lines and drift around the earth

under the action of $\overrightarrow{E} \times \overrightarrow{B}$ and $grad\overrightarrow{B}$ forces. They precipitate into the earth's atmosphere if their mirror height is at an altitude at which the neutral density is high enough for collisions to occur. The mirror height can be lowered, causing precipitation, if an interaction or energy exchange takes place. Of particular interest in this study is the cyclotron resonance interaction in which whistler mode waves exchange energy with counterstreaming electrons. During the subsequent precipitation the electrons cause secondary ionisation within the earth's atmosphere, modifying the earth-ionosphere wave guide and causing perturbations, known as Trimpi events, on sub-ionospheric VLF transmitter signals. Amplitude Trimpis were first noticed by M.L.Trimpi in Antarctica in 1963 and were first reported by Helliwell et al [1973]. Phase Trimpis were later reported by Lohrey and Kaiser [1979]. Trimpis have been studied in detail by, to mention a few, Carpenter et al [1984], Dowden and Adams [1988] and Inan and Carpenter [1987].

Whistler mode waves can also be amplified through the cyclotron resonance interaction. The rising tones in figure 1.2 are thought to be generated by resonating electrons after they have been phase bunched by the preceding whistlers (Helliwell [1967]). The change in frequency occurs as the resonance region drifts, in this case, away from the equatorial plane.

In this thesis we study Trimpis and whistlers observed during a campaign on Marion Island ($46°53"S$, $37°52"E$, $L = 2.63$) in May 1996. The timing between the Trimpis and whistlers is accurately determined and electron precipitation times are obtained and are compared with the start time of the Trimpis. The electron energies are also calculated.

1.3.2 Triggered Atmospheric Discharges

Armstrong [1987] suggested that almost in phase whistler echo trains could indicate that particle precipitation may trigger lightning strikes. Dowden et al [1996c] studied sprites and associated Trimpis and also suggested that there may be a connection between the sprite discharge and the duct along which the whistler, and the energetic particles, propagate. During the campaign on Marion Island it was noticed that the Trimpi associated whistlers were followed, after a time of between 500 ms−700 ms, by a second whistler group which we have called a whistler 'ghost' group. It is thought that the initiating atmospheric for the 'ghost' group may have been triggered by energetic electrons precipitated after a cyclotron resonance interaction with the first whistler group. This possibility is studied by calculating the particle bounce times and by ray tracing whistler mode waves through ducts of enhanced ionisation to determine the whistler travel times.

1.4 Synopsis of this Thesis

Chapter 2 discusses the whistler mode phase refractive index and the techniques for tracing whistler mode signals through the ionosphere and magnetosphere. It also describes the computer programme that was used to trace these signals.

Chapter 3 introduces the density and magnetic field models used in the ray tracing and describes how they may be varied to produce models for use in the different situations. The introduction of ducts and latitudinal density gradients is also discussed.

Chapter 4 describes the fractional hop whistlers observed on the ISIS2 satellite and discusses the results obtained using the ray tracing techniques. These results are compared with those obtained by Hughes [1981] and Hughes and Rice [1997].

Chapter 5 introduces wave particle interactions, concentrating on the cyclotron resonance interaction.

Chapter 6 presents the results obtained from studying Trimpis and associated whistlers observed on Marion Island during May 1996.

Chapter 7 introduces what we have called a whistler 'ghost' and studies the hypothesis that energetic particle precipitation may trigger atmospheric discharges that can be observed as whistlers.

Chapter 8 is a summary of the results and a conclusion. It also gives suggestions for future work.

Chapter 2

Waves in a Cold Magnetoplasma

2.1 Introduction

This study uses the propagation of whistler mode waves through a cold magnetoplasma to understand the characteristics of signals received on a satellite. The magnetoplasma is assumed to be homogeneous (varies slowly in the space of one wavelength) and anisotropic. In such a medium the wave's phase refractive index depends on the electron and ion densities and on the magnetic field configuration. Density and magnetic field models for this magnetoplasma will be discussed in the next chapter. In this chapter we will review the techniques for determining ray paths and travel times. The standard Haselgrove [1954] ray tracing equations are used. These require the phase refractive index and its derivatives at each point in the medium which are found using the dispersion relation from Stix [1962, 1992]. MKS units have been used in the ray tracing and refractive index equations. In some cases centimetres or kilometres have be used when the numerical values of certain quantities are given.

2.2 Phase Refractive Index

The phase refractive index is found by solving Maxwell's equations for an anisotropic, homogeneous medium in which collisions between neutrals and ions are neglected. This assumption is valid above the D and E regions of the ionosphere. Although this study considers propagation through the D and E regions, it is assumed that the time spent in these regions is small enough for the effect of collisions to be ignored.

The dispersion relation for the medium has the following form

$$A\mu^4 - B\mu^2 + C = 0 \tag{2.1}$$

where μ is the phase refractive index and

$$\begin{aligned} A &= S\sin^2\psi + P\cos^2\psi \\ B &= RL\sin^2\psi + PS\left(1+\cos^2\psi\right) \\ C &= PRL \end{aligned} \tag{2.2}$$

ψ is the angle between the wave normal and the magnetic field direction and R, L, P and S depend on the wave frequency (ω) and are defined in terms of the electron and ion plasmafrequencies (π_k) and gyrofrequencies (Ω_k) in the following way

$$\begin{aligned} S &\equiv \frac{1}{2}(R+L) \qquad D \equiv \frac{1}{2}(R-L) \\ R &\equiv 1 - \sum_k \frac{\pi_k^2}{\omega^2}\left(\frac{\omega}{\omega + \varepsilon_k\Omega_k}\right) \\ L &\equiv 1 - \sum_k \frac{\pi_k^2}{\omega^2}\left(\frac{\omega}{\omega - \varepsilon_k\Omega_k}\right) \\ P &\equiv 1 - \sum_k \frac{\pi_k^2}{\omega^2} \end{aligned} \tag{2.3}$$

The plasmafrequency (π_k) and gyrofrequency (Ω_k) of the k^{th} species (in rad.s^{-1}), are $\left(\frac{n_k e^2}{\epsilon_o m_k}\right)^{\frac{1}{2}}$ and $\frac{eB}{m_k}$ respectively, where e is the electron charge, ϵ_o is the dielectric constant of free space, m_k is the mass of the k^{th} species, n_k is the density of the k^{th} species and B is the magnetic field strength. Both n_k and B are determined using the density and magnetic field models that will be discussed in the next chapter. The term ε_k in equations (2.3) is -1 for the electrons and $+1$ for the ions. All the above frequencies are angular frequencies (measured in rad.s^{-1}) and can be converted to a frequency in Hertz using $f = \frac{\omega}{2\pi}$. The numerical values for the wave frequency, the gyrofrequencies and the plasma frequencies that will be cited later in the text will be in kHz or MHz.

Equation (2.1) can be solved to give

$$\mu^2 = \frac{B \pm F}{2A} \tag{2.4}$$

where

$$F^2 = (RL - PS)^2 \sin^4\psi + 4P^2D^2\cos^2\psi \tag{2.5}$$

For each value of the wave normal angle (ψ), equation (2.4) has two solutions corresponding to two different polarisations. For the longitudinal case ($\psi = 0$), $\mu^2 = R$ or $\mu^2 = L$ and for the transverse case ($\psi = \frac{\pi}{2}$), $\mu^2 = \frac{RL}{S}$ or $\mu^2 = P$. This study will consider mainly the mode that would have $\mu^2 = R$ if it were propagating longitudinally. This is known as the electron whistler mode. Waves propagating in the mode that would have $\mu^2 = L$ if they were propagating longitudinally are ion-cyclotron whistlers. A very good review on 'ion' cyclotron whistlers is given in Jones [1972].

The wave polarisation is given by

$$\rho = \frac{E_x}{E_y} = \frac{\mu^2 - S}{D} \tag{2.6}$$

For the longitudinal case the wave corresponding to $\mu^2 = R$ has a polarisation $\rho = 1$ and the wave with $\mu^2 = L$ has a polarisation $\rho = -1$. Both of these waves are therefore circularly polarised: the R, or electron whistler, in the right hand sense and the L, or 'ion' whistler, in the left hand sense. For cases other than the longitudinal case, the polarisation becomes elliptical for both modes.

Figure 2.1 shows the square of the refractive index against frequency (normalised with respect to the proton gyrofrequency) for a wave with a longitudinal wave normal. For frequencies greater than the proton gyrofrequency the square of the refractive index has a single positive value. This is the R mode and it is the only mode that can propagate above the proton gyrofrequency. It is continuous and positive for all frequencies shown in figure 2.1. It has a resonance ($\mu = \infty$) at the electron gyrofrequency. This is not shown in the figure as this study will concern frequencies well below the electron gyrofrequency.

The plasma considered here has three ion species and consequently, the L mode exists in three frequency bands. These bands are below the atomic oxygen gyrofrequency, between the atomic oxygen and helium gyrofrequencies and between the helium and proton gyrofrequencies. At each gyrofrequency the L mode has a resonance. Between two ion gyrofrequencies there is a cut-off ($\mu = 0$) and the

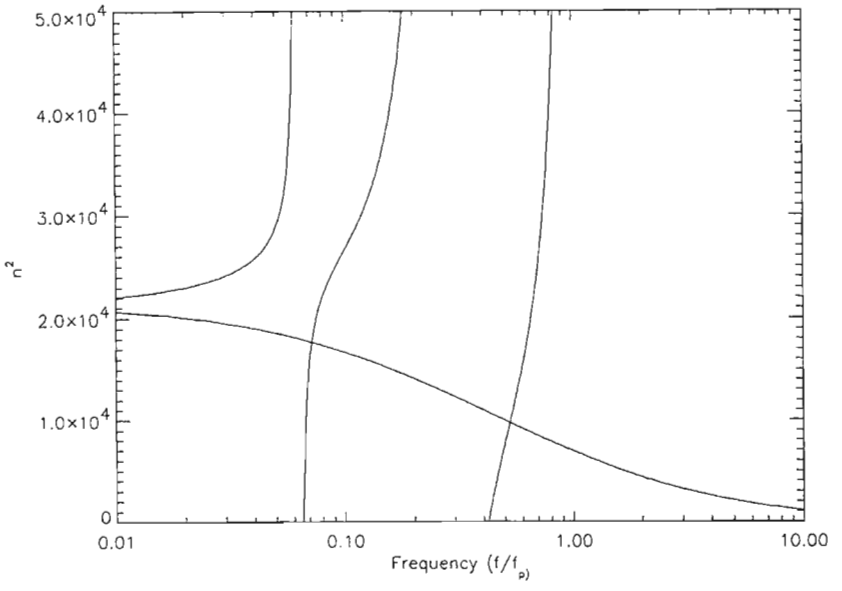

Figure 2.1: Square of the refractive index against frequency, normalised w.r.t. the proton gyrofrequency, for $\psi = 0^o$.

wave is evanescent between the lower of the two ion gyrofrequencies and this cut-off frequency. Between the oxygen and helium gyrofrequencies the cut-off frequency is given by

$$\omega_{co} = \alpha_o \pi_o + \alpha_{He} \pi_{He} \tag{2.7}$$

where α_o and α_{He} are the atomic oxygen and helium ion concentrations and π_o and π_{He} are their gyrofrequencies. Between ω_{co} and the helium gyrofrequency the L mode can propagate and in this frequency range there is a crossover frequency where the L mode refractive index and the R mode refractive index are the same. This cross-over frequency is given by

$$\omega_c^2 = \alpha_o \pi_o^2 + \alpha_{He} \pi_{He}^2 \tag{2.8}$$

At the cut off frequency the resultant wave is linearly polarised.

Between the helium and proton gyrofrequencies there is another cut-off frequency and another cross-over frequency. These frequencies are given by equations that are exactly analogous to equations (2.7) and (2.8).

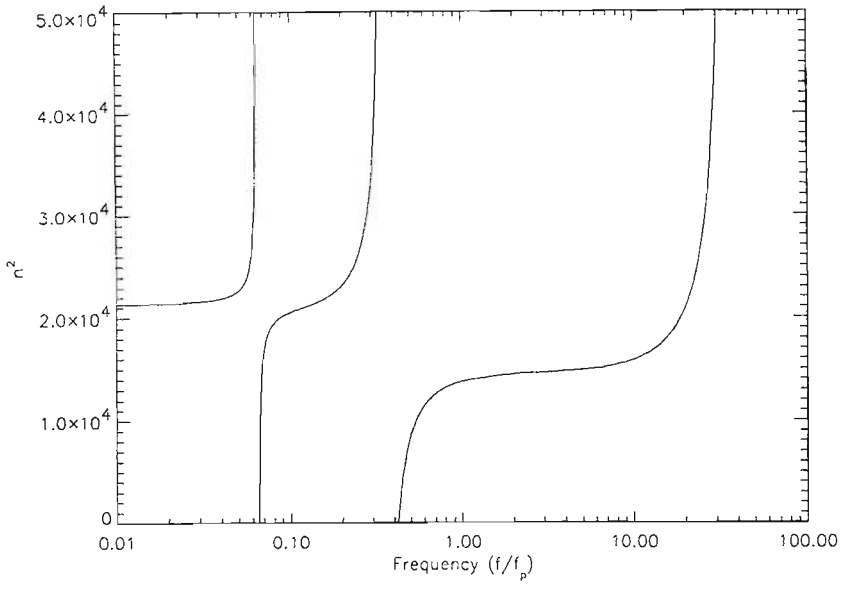

Figure 2.2: Square of the refractive index against frequency, normalised w.r.t. the proton gyrofrequency, for $\psi = 90^o$.

Figure 2.2 is similar to figure 2.1 except it is for the transverse case ($\psi = 90^o$). In this case, only a single mode exists and is known as the extraordinary mode. It has a resonance whenever $S = 0$. The highest of the resonance frequencies shown in figure 2.2 is the 'lower hybrid resonance frequency' while the resonances at frequencies lower than this are known as the 'two-ion hybrid resonances' or the 'ion-ion hybrid resonances'. The actual resonance frequencies depend on the relative concentrations of the different ion species. There is an 'upper hybrid resonance', not shown in the figure, above the electron plasma frequency. The extraordinary mode is evanescent between each 'lower hybrid resonance' and a cut-off frequency given by equation (2.7). For frequencies between the greater of the 'lower hybrid resonances' and the 'upper hybrid resonance' the wave is evanescent.

If the ion terms in equations (2.3) are neglected (which is sometimes done to simplify the expression for the phase refractive index) waves with transverse wave normals cannot propagate for all frequencies below the 'upper hybrid resonance'. If the ion terms are taken into account, transverse propagation is possible in one or more frequency bands below the 'lower hybrid resonance'. It is still, however, impossible at all frequencies between the 'upper' and 'lower hybrid resonances'.

2.2.1 Refractive Index Surfaces

As a result of the anisotropy of the magnetoplasma, the refractive index does not have a unique value at every point in space but depends on the wave normal angle. The refractive index of a wave of frequency ω at a position x, y and with wave normal ψ can be written as $\mu(x, y, \psi, \omega)$. This can be regarded as consisting of two components μ_x and μ_y given by $\mu\cos\psi$ and $\mu\sin\psi$ respectively. These two components, μ_x and μ_y, can be considered as belonging to a co-ordinate system, known as refractive index space, such that (μ_x, μ_y) is a point in this space. By varying the value of the wave normal angle, ψ, a complete set of possible points (μ_x, μ_y) can be determined for each position in real space. These points trace out a curve in refractive index space. Since the refractive index depends only on ψ, this curve can be rotated about the magnetic field direction to give a surface known as a refractive index surface. In this refractive index space the magnetic field lies along the direction defined by $\psi = 0$.

The equation for the refractive index surface (from the definitions for μ_x and μ_y) can be written as

$$G\left(x, y; \mu_x, \mu_y\right) \equiv \frac{\left(\mu_x^2 + \mu_y^2\right)^{\frac{1}{2}}}{\mu\left(x, y, \psi, \omega\right)} = 1 \tag{2.9}$$

Each point in real space has a frequency dependent, refractive index surface associated with it. This surface is defined such that a vector from the origin to the refractive index surface, in the direction of the wave normal, has a magnitude equal to the phase refractive index. It also has the property (Poeverlein [1948]) that the ray direction is perpendicular to the refractive index surface at the point at which the vector touches the surface. Figure 2.3 illustrates a slice through the upper portion of a refractive index surface showing the wave normal and ray directions.

This property of the refractive index surface is the basis for ray tracing. If the initial wave normal angle is known then the refractive index and ray direction can be determined from the refractive index surface. The wave then propagates an infinitesimal distance in the ray direction to a new point at which the refractive index surface must also be known. The wave normal angle at this new position is determined from Snell's law $\left(\mu_1\left(\psi_1\right)\sin\psi_1 = \mu_2\left(\psi_2\right)\sin\psi_2\right)$ where ψ_1 and ψ_2 are measured relative to local stratifications. Using the new refractive index surface and the new wave normal angle, the ray direction at this new position can be determined and the process repeated.

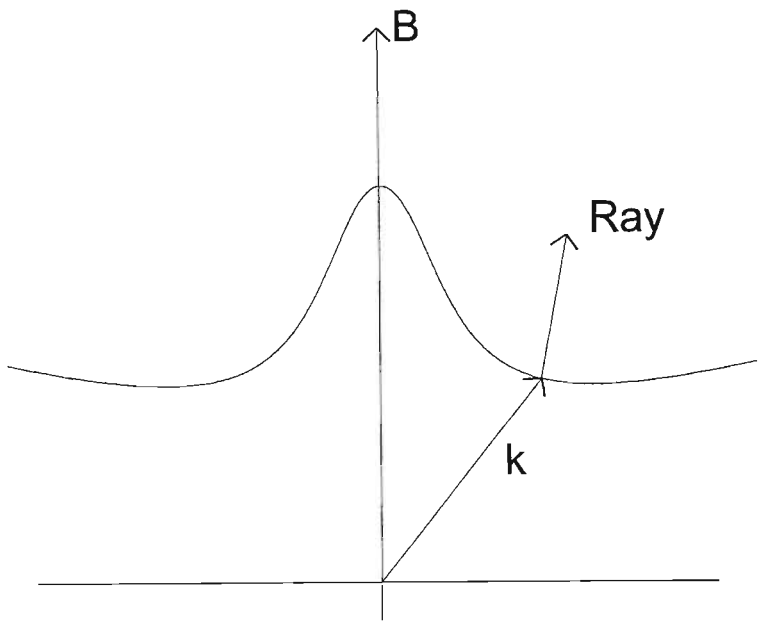

Figure 2.3: Diagram of the refractive index surface showing the wave normal and ray directions.

This method is rather cumbersome and not particularly practical. To simplify matters a set of differential equations describing how the ray position and wave normal angle vary with 'time' were derived by Haselgrove [1954].

2.2.2 Effect of Ions on the Refractive Index Surface

Storey [1953] showed that if ions are ignored and the wave frequency is much less than the electron gyrofrequency, which in turn must be less than the electron plasma frequency, the ray direction could not make an angle of greater than 19°29′ with the magnetic field direction. Hines [1957] showed that if ions are included in the refractive index then this no longer applies and showed that even transverse propagation is allowed in bands below each of the lower hybrid resonance frequencies. This is illustrated in figure 2.2. In terms of refractive index surfaces, this means that the refractive index surface is closed for these frequencies. This is illustrated in figure 2.4 which shows two refractive index surfaces, one corresponding to a frequency above the 'lower hybrid resonance' frequency and the other to a frequency below the 'lower hybrid resonance' frequency. If a wave has a frequency for which the refractive index surface is closed, then this wave will be reflected if its wave normal becomes perpendicular to the magnetic field direction. Kimura [1966] studied the effect of ions in whistler-mode ray tracing.

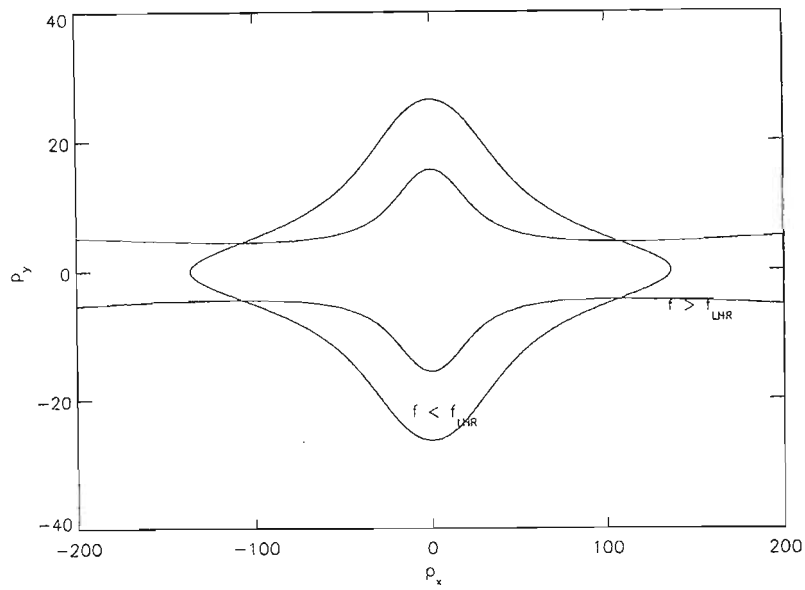

Figure 2.4: Diagram showing refractive index surfaces for frequencies above and below the lower hybrid resonance frequency.

For frequencies above the lower hybrid resonance frequency, a maximum wave normal angle exists. Revolving this about the magnetic field direction forms a cone known as the resonance cone. All possible wave normal angles must fall within the resonance cone.

2.3 Ray Tracing Equations

As was seen in the previous section, the energy of an electromagnetic wave does not in general travel in the wave normal direction. In an inhomogeneous, anisotropic medium, like the ionosphere and magnetosphere, the energy follows a curved path known as the ray path.

The equations that determine the path of a ray in a magnetoplasma were first derived by Haselgrove [1954]. A good derivation and explanation of the ray tracing equations is also given in Budden [1961, 1985]. The equations are derived using Fermat's principle of stationary time. If m is the ray refractive index ($m = \mu \cos\alpha$, where α is the angle between the ray direction and the wave normal direction) then the ray path must be such that the integral of m along this path is an extremum (minimum or maximum). This can be written as

$$\delta \int m ds = 0 \tag{2.10}$$

A spherical polar coordinate system has been used (r, θ, ϕ) with azimuthal symmetry (no ϕ dependence) and with θ measured from the pole. This reduces the ray tracing to effectively 2 dimensions. The equations also use χ, the angle between the wave normal direction and the radial direction, instead of ψ, the angle between the wave normal direction and the magnetic field direction. The equations are as follows

$$\begin{aligned}
\frac{dr}{dt} &= \frac{1}{\mu^2}\left(\mu\cos\chi + \frac{\partial\mu}{\partial\chi}\sin\chi\right) \\
\frac{d\theta}{dt} &= \frac{1}{r\mu^2}\left(\mu\sin\chi - \frac{\partial\mu}{\partial\chi}\cos\chi\right) \\
\frac{d\chi}{dt} &= \frac{1}{r\mu^2}\left(\frac{\partial\mu}{\partial\theta}\cos\chi - \left[r\frac{\partial\mu}{\partial r} + \mu\right]\sin\chi\right)
\end{aligned} \tag{2.11}$$

These equations can be simplified since χ and ψ differ by a constant and therefore $\frac{\partial\mu}{\partial\chi} = \frac{\partial\mu}{\partial\psi}$. As can be seen from equation (2.2), $\frac{\partial\mu}{\partial\psi}$ is much easier to evaluate than $\frac{\partial\mu}{\partial\chi}$.

2.3.1 Ray Travel Time

The time of flight of a pulse of energy along a ray path is

$$\frac{1}{c}\int \mu_g \cos\alpha ds = \int \left(\frac{\mu_g}{\mu}\right) dt \tag{2.12}$$

where μ_g is the group refractive index and α is the angle between the ray direction and the wave normal direction. The right hand side of the above equation was derived using that $\frac{ds}{dt} = ray\ velocity = \frac{c}{\mu\cos\alpha}$.

The group refractive index (in the direction of the phase refractive index) is given by

$$\mu_g = \frac{\partial(\mu\omega)}{\partial\omega} = \mu + \omega\frac{\partial\mu}{\partial\omega} \tag{2.13}$$

Using equation (2.12) a new variable P, called the 'equivalent path', is defined such that

$$\frac{dP}{dt} = \frac{\mu_g}{\mu} = 1 + \frac{\omega}{\mu}\frac{\partial \mu}{\partial \omega} \tag{2.14}$$

The wave travel time is then given by $\frac{P}{c}$ where c is the free space speed of light.

2.4 Derivatives of μ

The calculation of the ray path requires the derivatives of the phase refractive index (μ) with respect to r, θ, ψ and ω. It must be remembered that the derivative w.r.t. ψ is the same as the derivative w.r.t. χ. μ depends explicitly on ψ and ω and implicitly on r and θ. The derivative of μ w.r.t. ψ is found by differentiating equation (2.4) to get

$$\frac{\partial \mu}{\partial \psi} = \frac{1}{2\mu}\left(\frac{\frac{\partial B}{\partial \psi} \pm \frac{\partial F}{\partial \psi}}{2A} - 2\frac{\partial A}{\partial \psi}\frac{B \pm F}{2A^2}\right) \tag{2.15}$$

where B, F and A are defined in equations (2.2) and (2.5). The derivative of μ w.r.t. ω has the same form as equation (2.15). In this case B, F and A do not depend explicitly on ω but are defined in terms of R, L, P, S and D (equations (2.3)) which do depend explicitly on ω.

Determining $\frac{\partial \mu}{\partial r}$ and $\frac{\partial \mu}{\partial \theta}$ was done numerically from first principles. If x is either r or θ then

$$\frac{\partial \mu}{\partial x} = \frac{\mu\left(x + \frac{\delta x}{2}\right) - \mu\left(x - \frac{\delta x}{2}\right)}{\delta x} \tag{2.16}$$

where all variables other than x are kept constant. To test this numerical differentiation, the derivative of μ w.r.t. ψ computed analytically was compared with the result obtained using the above numerical technique. The results obtained numerically were very close to those obtained analytically.

2.5 Computing the Ray Paths

To compute the path of a whistler mode wave, of frequency ω, through the ionosphere and magnetosphere, equations (2.11) are used. As can be seen from these three equations, the refractive index, together with its derivatives with respect to r, θ and ψ, is needed at every point along the path.

If the wave starts at an initial point r_o, θ_o with initial wave normal angle χ_o, the first step is to calculate the refractive index at this position. This requires the wave normal angle with respect to the magnetic field direction (ψ), the ion and electron densities and the magnetic field strength (B). The value of B and ψ depend on the chosen magnetic field model. The values of the ion and electron densities depend on the density model. Both the magnetic field and density model will be discussed in more detail in the next chapter.

The derivatives of μ w.r.t. r, θ and ψ are then calculated at $r_o, \theta_o$and these values, together with the value of μ, are then used in equations (2.11) to determine new values for r, θ and χ. The procedure is then repeated using this new position and wave normal angle until the wave has reached its desired destination.

The travel time of the wave is calculated using equation (2.14) which uses the value of the phase refractive index and its derivative with respect to wave frequency ω.

To perform the above procedure a Fortran programme was written. This programme uses a Runge-Kutta procedure (Press et al [1986]), with a user defined step size, to numerically solve the four ray-tracing equations. The initial position and wave normal angle are input by the user and the programme calculates the ray path and travel time until either a predefined position is reached or a certain number of steps have passed.

A copy of the computer programme and a short explanation of how it works is in Appendix A.

Chapter 3

Magnetospheric Models

3.1 Introduction

The previous chapter discussed the propagation of whistler mode waves through a magnetoplasma. Equations for calculating the phase refractive index and its derivatives were given together with a technique for determining the ray paths and travel times. To determine the phase refractive and its derivatives, values for the electron and ion densities and the magnetic field strength are needed at every point of the medium through which the signal is propagating. In this study the medium is the ionosphere and magnetosphere and hence density and magnetic field models for these regions will be considered in this chapter.

3.2 Density Models

In the ionosphere the production of ions and electrons by photoionisation is balanced by recombination and is modelled by the Chapman ion production function. In the magnetosphere, production is negligible and the ion and electron densities are determined using the diffusive equilibrium model of Angerami and Thomas [1964]. The two models are matched at an altitude of 500 km.

3.2.1 Ionospheric Model

The ionosphere is modelled using a Chapman layer. The rate of ionisation, at an altitude h, of the j^{th} neutral component can be shown to be given by

$$q_j = q_{mj} \exp\left\{1 - \frac{(h - h_{mj})}{H_j} - \exp\left[\frac{-(h - h_{mj})}{H_j}\right]\right\} \tag{3.1}$$

where h_{mj} is the height where maximum production occurs, q_{mj} is the rate of maximum production and H_j is the scale height of the j^{th}component given by $\frac{kT}{m_j g}$. k is the Boltzmann constant, m_j is the mass of the j^{th} component and T and g are the temperature and gravitational acceleration both of which depend on h.

The ionisation is balanced by the recombination of electrons and ions. The rate of recombination of the j^{th} ion species is given by $L_j = \alpha_j n_e n_j$ where α_j is the recombination coefficient of the j^{th} species, n_e is the electron density and n_j is the density of the j^{th} ion species. If the rate of recombination (L_j) is equated with the rate of ionisation (q_j) N simultaneous non-linear equations are obtained for the N+1 densities. The electron density, n_e, can be eliminated by assuming quasi-neutrality ($n_e = \sum n_j$). The ion densities can then be found by solving the simultaneous equations iteratively. This is, however, rather difficult and can be simplified by assuming that $n_e = n_j$ independently for each ion species giving $L_j = \alpha_j n_j^2$. This is then equated with equation (3.1) to give each ion density

$$n_j = n_{mj} \exp\left\{1 - \frac{h - h_{mj}}{H_j} - \exp\left[\frac{-(h - h_{mj})}{H_j}\right]\right\}^{\frac{1}{2}} \tag{3.2}$$

n_{mj} is the maximum ion density and occurs at a height of h_{mj}. By assuming quasi-neutrality, the electron density is given by $\sum n_j$. Although the above simplification is not strictly correct it will probably result in an ionospheric model that is good enough for use in this study.

Knowing the intensity of the ionizing radiation, the solar zenith angle, the density of each neutral atomic species and the ionisation cross section for each species, values for n_{mj} and h_{mj} could be calculated. This is rather complicated and in our case these values are obtained by specifying that the ionospheric model must match the magnetospheric model, at an altitude of 500 km, in both magnitude and slope for each ion species and for the electrons.

3.2.2 Magnetospheric Models

The magnetosphere, above 500 km, is modelled using the diffusive equilibrium model derived by Angerami and Thomas [1964]. Diffusive equilibrium assumes that the partial pressures for each species is balanced by the earth's gravitational force, the centrifugal force and the force due to the electric field arising from charge separation. The diffusive equilibrium model assumes the following :

- The charged particles are only able to move along the lines of force of the earth's magnetic field.
- No electrons are produced by the action of the sun's rays above 500km.
- The electron recombination rate is so small that it can be ignored.
- The axis of rotation of the earth coincides with the magnetic dipole axis.
- The ion species are all singly ionised.

Using the above assumptions, and following the method of Angerami and Thomas [1964], the diffusive equilibrium equations were derived and the following was obtained for the electron and ion densities at a position s along a magnetic field line as shown in figure 3.1.

$$n_e(s) = \frac{1}{T}\left\{n_{eo}T_o \sum_i \left[n_{io}T_o \exp\left(\frac{-z}{H_i}\right)\right]\right\}^{\frac{1}{2}} \tag{3.3}$$

$$n_i(s) = \frac{1}{n_e T^2}(n_e T)_o (n_i T)_o \exp\left(\frac{-z}{H_i}\right) \tag{3.4}$$

T is the electron and ion plasma temperature which are assumed to be the same. The subscript o refers to a reference point (r_o, θ_o) at which the temperature (T_o) and the electron and ion densities (n_{eo} and n_{io}) are known. This reference point lies on the magnetic field line that passes through the point s. In this study the reference height is constant but the reference latitude depends on the field line along which the density is to be determined. H_i is the scale height of the i^{th} ion species at this reference height and is given by $\frac{kT_o}{m_i g_o}$. k is once again the Boltzmann constant, m_i is the mass of the i^{th} ion species and T_o and g_o are the temperature and gravitational acceleration at the reference height. In this case the scale height is constant as opposed to the ionospheric model in which the scale height varied with altitude. In general, the scale height is the height over which the density decreases by e^{-1}. It depends on temperature and on the gravitational strength and is not constant with height. The use of a constant scale height term in this case is possible because of the definition of z, the 'temperature modified geopotential height'. z is defined as

$$z = \int_{s=0}^{s=s'} \frac{f(s)\,T_o}{g_o T} ds \tag{3.5}$$

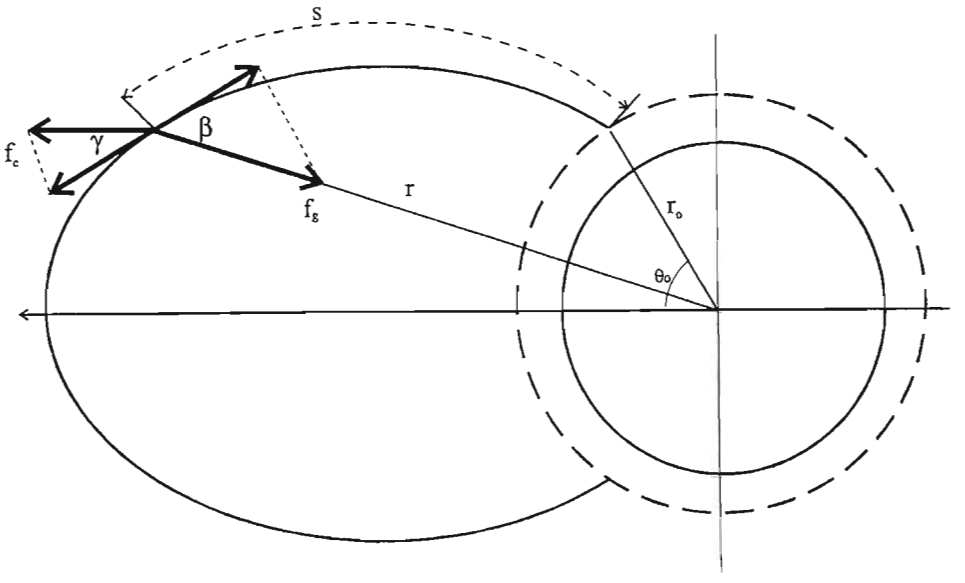

Figure 3.1: Gravitational and centrifugal forces acting on a unit mass at position r, θ.

where the integration is carried out along the magnetic line of force. $f(s)$ is the total force, directed along the field line, acting on a unit mass at a position s and includes the centrifugal and gravitational forces. This is illustrated in figure 3.1.

The total force $f(s)$ is given by the sum of the field aligned components of the gravitational and centrifugal forces and hence z can be divided into a gravitational term and a centrifugal term both of which can be solved independently. Since the integration must be carried out along the magnetic field line, each term will depend on the choice of magnetic field model. The magnetic field model will be discussed in more detail in the next section, but the simplest, in our case, is a centered dipole. If the temperature along the field lines is isothermal (it need not be isothermal across field lines) the gravitational and centrifugal force terms are given by

$$z_g = r_o \left(1 - \frac{r_o}{r}\right) \tag{3.6}$$

$$z_c = \frac{\Omega^2 r_o^2}{2g_o} \left[\cos^2 \theta_o - \frac{\cos^6 \theta}{\cos^4 \theta_o}\right] \tag{3.7}$$

where Ω is the angular velocity of rotation of the earth about its geographic axis and θ_o is the latitude of the field line at the reference height as shown in figure

3.1. The total 'temperature modified geopotential height' is then given by the sum of the above two terms.

Satellite observations have shown that an isothermal temperature assumption is not valid. For altitudes below about 2000 km the plasma temperature increases with height. To model this the following function was used

$$T = T_o + m(r - r_o) \tag{3.8}$$

where m is the temperature gradient (1.85 K.km^{-1} in our case). This temperature model is similar to the one used by Thomson [1987].

Using equation (3.8), the gravitational force term must be recalculated and is found to be

$$z_g = T_o r_o^2 \left\{ \frac{m}{(T_o - m r_o)^2} \ln\left[\frac{T r_o}{T_o r}\right] + \frac{1}{(T_o - m r_o)} \left(\frac{r - r_o}{r r_o}\right) \right\} \tag{3.9}$$

The centrifugal force term is not as simple and, with the above temperature model, must be found by numerically integrating the following equation

$$z_c = \frac{3 T_o \Omega^2 r_o^2}{g_o \cos^4 \theta_o} \int_{\theta_o}^{\theta} \frac{\sin\theta' \cos^5\theta'}{\left[T_o + m r_o \left(\frac{\cos^2\theta'}{\cos^2\theta_o - 1}\right)\right]} d\theta' \tag{3.10}$$

If m is set to zero (isothermal magnetosphere) equations (3.9) and (3.10) reduce to equations (3.6) and (3.7).

It can be seen from equations (3.6) and (3.9) that z_g depends only on altitude and not on latitude and hence is independent of the choice of magnetic field model. At low altitudes θ_o and θ are reasonably close and hence z_c can sometimes be ignored.

To determine the electron and ion densities at a point r, θ using an isothermal temperature, the 'temperature modified geopotential height' must be calculated by adding the results of equations (3.6) and (3.7). Equations (3.3) and (3.4) are then used, with the temperature and the electron and ion densities at the relevant reference point, to calculate the electron and ion densities at position r, θ. If the non-isothermal temperature model is used then equation (3.8) must be used in equations (3.9) and (3.10) to determine the 'temperature modified geopotential height'. The densities are, once again, calculated using equations (3.3) and (3.4).

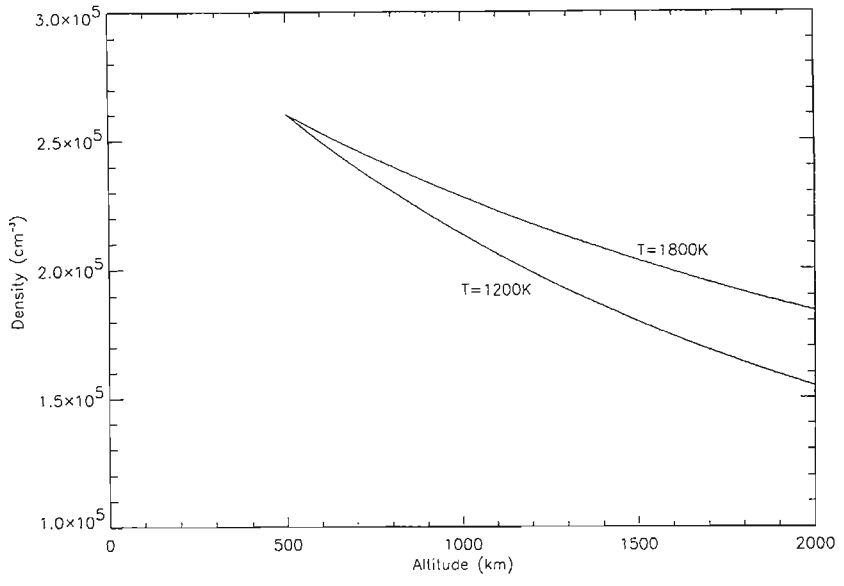

Figure 3.2: Electron densities in an isothermal magnetosphere at two different temperatures.

3.2.2.1 Effect of Temperature on Magnetospheric Model

If we consider an isothermal magnetosphere then equations (3.6) and (3.7) are used to determine the 'temperature modified geopotential height'. For a given set of reference (r_o, θ_o) electron and ion densities, the densities at a new position (r, θ) will vary according to the choice of temperature. For an isothermal magnetosphere ($T = T_o$) with a single ion species, equation (3.3) shows that the scale height ($H_i = \frac{kT_o}{m_i g_o}$) is the height over which the electron density decreases by $e^{-\frac{1}{2}}$. If the temperature is increased, the scale height increases and the density at a given position also increases. This is illustrated in figure 3.2.

If a non isothermal temperature model, such as equation (3.8), is used, equation (3.3) shows that, since $T > T_o$, the electron density will actually decrease by more that $e^{-\frac{1}{2}}$ in a distance equal to the scale height. This is illustrated in figure 3.3 where the temperature in the isothermal case is the same as the reference temperature in the non-isothermal case.

Since it has been assumed that the magnetosphere contains only one ion species and that the plasma is quasi-neutral, the above profiles are the same for the ions and for the electrons.

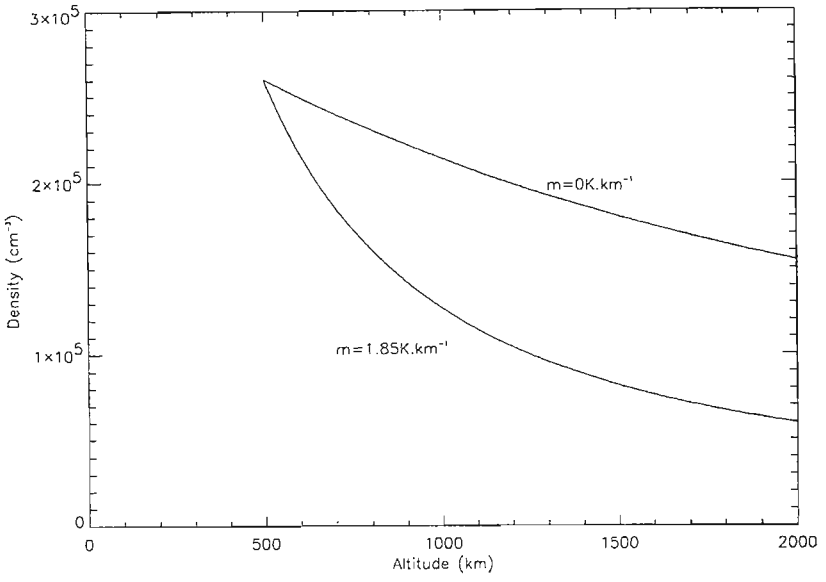

Figure 3.3: Comparison between electron densities in non-isothermal and isothermal magnetospheres with the same intial temperature.

3.2.2.2 Effect of Ion Concentration on Magnetospheric Model

In section 3.2.2.1, single ion isothermal and non-isothermal magnetospheres were discussed. If there is more than one ion the situation is slightly more complicated as each ion species has its own scale height ($H_i = \frac{kT_o}{m_i g_o}$) and each term in the sum in equation (3.3) decreases by e^{-1} over a different height. The rate at which the electron density (n_e) decreases depends on the relative proportion of each ion species at the reference height. The lightest ion species has the greatest scale height and hence the greater the proportion of the lightest ion species, the greater the height over which the electron density decreases by a fixed amount. This is illustrated in figure 3.4 where a magnetosphere with two different ion species (H^+ and O^+) are considered with two different concentrations. As can be seen, in the case where the H^+ and O^+ concentrations are both $0.5n_{eo}$ the electron density falls off more slowly than in the case where the H^+ concentration is lower than the O^+ concentration.

3.2.3 Matching the Two Density Models

The final magnetospheric model contains electrons and 3 ion species, protons, atomic oxygen ions and helium ions. For the study of low latitude fractional-hop

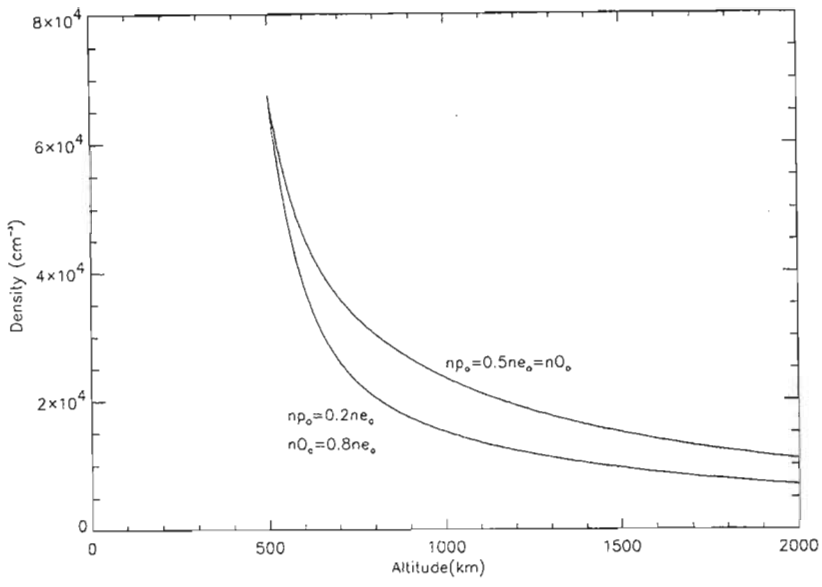

Figure 3.4: Comparison between the electron densities with two different reference ion concentrations.

whistlers, the reference altitude was chosen to be 500 km. The reference ion concentrations were chosen to be 9% protons, 7% helium ions and 84% atomic oxygen ions. The reason for this will be discussed in more detail in chapter 4. The temperature gradient was chosen to be 1.85 K.km^{-1} with a reference temperature of 1200 K which gives a similar temperature gradient to that given by International Reference Ionosphere 1990 for the same time of day and location.

For the study of ducted whistlers at middle latitudes the reference altitude was chosen to be 1000 km with reference ion concentrations of 8% protons, 2% helium ions and 90% oxygen ions as in Park [1972]. An isothermal temperature of 1600 K was used. The actual reference electron densities for both the fractional-hop whistler case and the ducted whistler case will be discussed in later chapters.

In both cases the ionospheric and magnetospheric density models are matched at an altitude of 500 km. The initial conditions (temperature and electron and ion densities at the reference height) are pre-defined for the magnetospheric model. The parameters for the ionospheric model (h_{mj}, n_{mj}) are then chosen in such a way that the three ion species (H^+,O^+ and He^+) are matched in both magnitude and slope. To simplify matters further, the ionospheric model in both cases is chosen to be isothermal and the ionospheric temperature is chosen such that the two models can be matched (there are certain temperatures for which it is not possible to match the two models) and such that the height of maximum electron

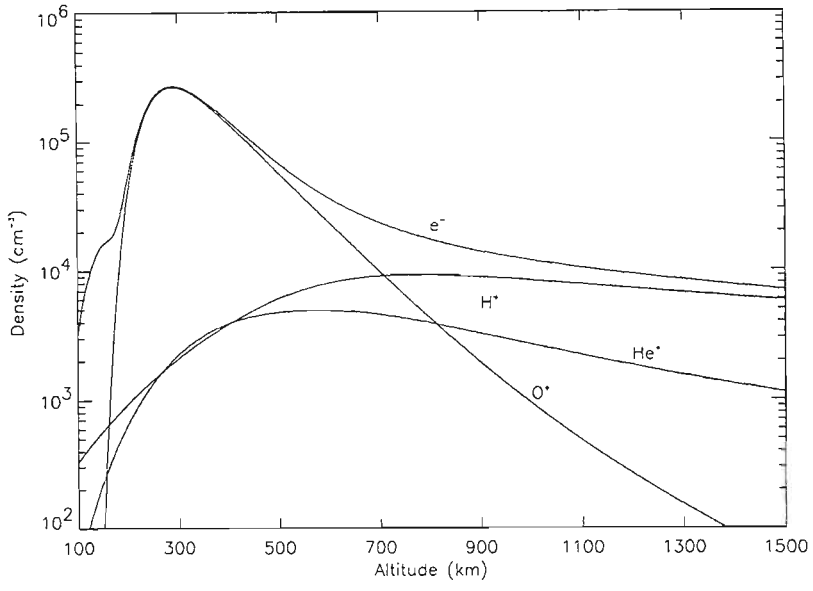

Figure 3.5: Electron and ion density profiles against altitude.

density is reasonable. This height was selected to be approximately 300 km and the resultant ionospheric temperatures were 843 K, for the study of fractional-hop whistlers, and 1380 K for the study of ducted whistlers. Using this technique it was found that the electron density below an altitude of about 150 km was too low. This was solved by including heavy ions (NO^+ and O_2^+) in the ionospheric models and choosing their height of maximum production (h_{mj}) and maximum density (n_{mj}) such that the electron density in the lower ionosphere was more reasonable. This is allowed an E layer to be included. The NO^+ and O_2^+ ions were not included in the matching as their densities at the matching height were so low as to be negligible. They were also not included when determining the phase refractive index as their gyrofrequencies are very low and hence their effect is negligible. A resultant density profile (including ions and electron) is shown in figure 3.5. The actual density values depend on the choice of the reference electron density.

3.2.4 Latitudinal Gradients

The electron and ion densities at a point s along a field line depend on the density values at a reference point on the same field line. The densities also depend on the force terms used in the 'temperature modified geopotential height'. Since the centrifugal force term (Equations (3.7) and (3.10)) has a latitudinal dependence,

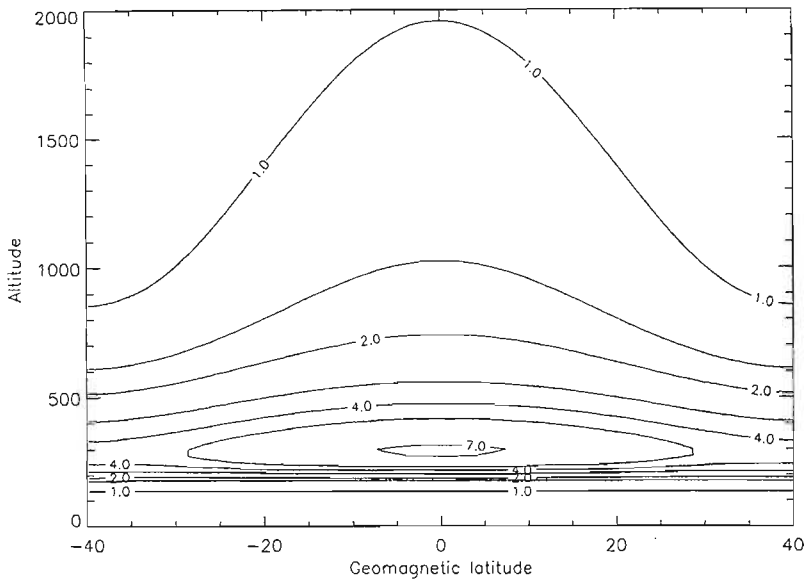

Figure 3.6: Contour plot showing the latitudinal variation in electron density. The contours are labelled in terms of the plasma frequency (MHz).

the electron and ion densities an altitude h above the earth's surface will have a latitudinal dependence, even if the reference values are latitudinally independent. At low altitudes and latitudes (as is the case in this study) the centripetal force term is, however, very small compared to the gravitational force term and this latitudinal gradient is almost negligible.

Latitudinal gradients can be introduced by choosing reference values that have a latitudinal dependence. In this study the reference electron density at a latitude θ was defined by the following equation (Thomson [1987])

$$n_{eo}(\theta) = n_{eo}\left(\theta_o'\right)\left[1 + E\cos\left(\frac{\pi}{2}\frac{\theta}{\theta_o'}\right)\right] \tag{3.11}$$

where θ_o' is a reference latitude at which the electron density is $n_{eo}\left(\theta_o'\right)$and E is the equatorial enhancement factor which was chosen to be 0.5. Equation (3.11) is a sinusoidal function and hence θ_o' must be chosen such that the reference electron densities do not oscillate over the latitudinal range of interest. The value used in this study and used by Thomson [1987] was 20^o. A contour plot illustrating the variation of electron density is shown in figure 3.6. The contours are labelled in MHz which refers to the electron plasma frequency.

3.2.5 Introducing Ducts

Ducts can be introduced into the density models in a way similar to the introduction of latitudinal gradients. Since the density along a field line depends on the density at a reference point on the same field line, ducts can be introduced by superimposing a duct like enhancement on the reference electron densities. The reference electron density is modified using the following equation from Yabroff [1961]

$$[n_{eo}(\theta)]_{duct} = n_{eo}(\theta)\left[1 + C\exp\left\{\frac{-(L-L_o)^2}{2W^2}\right\}\right] \tag{3.12}$$

where C is the enhancement factor, L_o is the L-value of the duct centre, L is the L-value at θ and W is the duct width at the reference height. Since the density along a field line depends on the density at the reference point and since field lines diverge towards the equatorial plane, the duct width will be greater at the equatorial plane than at the reference height. This satisfies the condition that the magnetic flux through the duct must remain constant. $n_{eo}(\theta)$ may be given by equation (3.11). L-values are used to describe magnetic field lines and will be discussed in more detail in the next section. Figure 3.7 shows a duct like enhancement superimposed on the reference electron density. The duct width, W, is 50 km and the enhancement factor, C, is 0.15.

Figure 3.8 shows a contour plot of the electron density resulting from the reference density shown in figure 3.7. It clearly shows how the duct aligns along the magnetic line on which the enhancement is centred.

Ducts will not be used in the study of low latitude fractional-hop whistlers, but will be used in the study of the interaction between whistler mode waves and energetic radiation belt electrons.

3.3 Magnetic Field Models

The ionosphere and magnetosphere are permeated by a magnetic field originating in the earth's core. This magnetic field has a strong influence of the propagation of waves through these regions and hence a model describing the magnetic field must be used. The earth's magnetic dipole axis makes an angle of 11.7° with the earth's rotation axis and does not pass through the centre of the earth. To simplify matters for the ray tracing, this discrepancy is ignored and a centered dipole model is used.

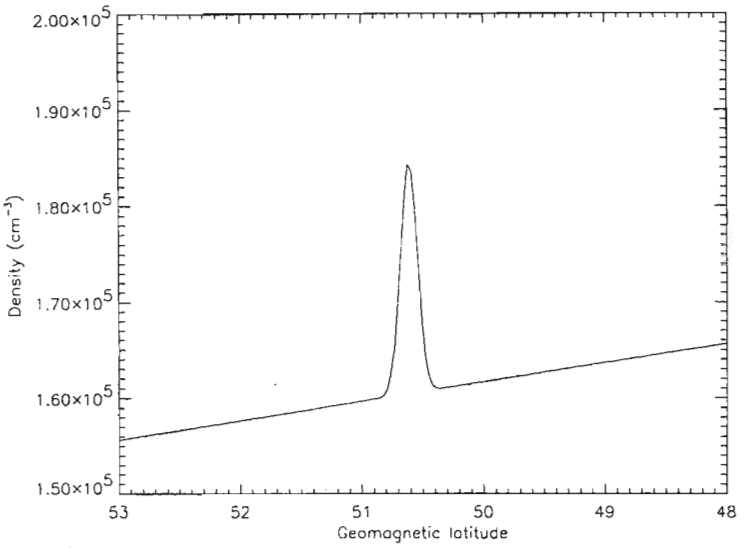

Figure 3.7: Duct like enhancement superimposed on the reference electron density.

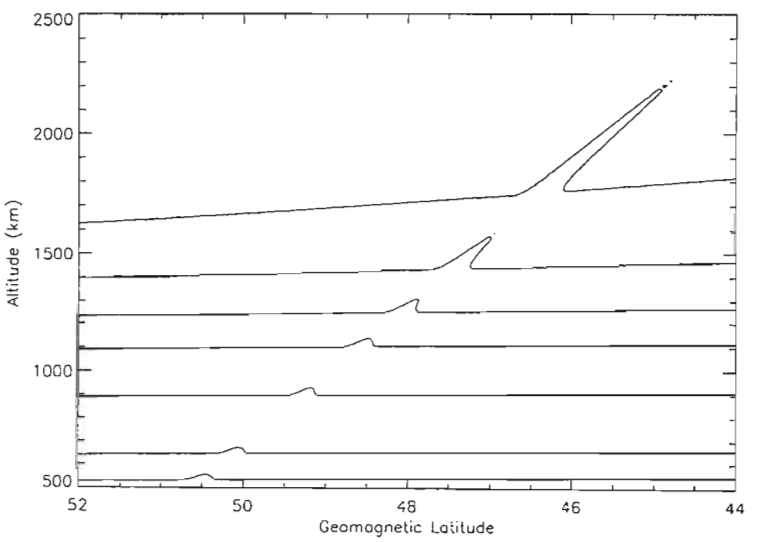

Figure 3.8: Contour plot of the electron density showing how the duct aligns with the magnetic field direction.

A more accurate model for low and middle geomagnetic latitudes is the International Geomagnetic Reference Field (IGRF). This is not used for the ray tracing but is used to determine the magnetic field strength at points on the earth's surface, to convert between geomagnetic and geographic co-ordinates and to calculate conjugate points.

3.3.1 Centered Dipole Field

The centered dipole model assumes that the dipole field is centered at the earth's centre. It also assumes axial symmetry and hence there are only two field components, one in the r direction and one in the θ direction with θ measured with respect to the geomagnetic equator. The components of the field at a point r,θ are

$$B_r = -2B_o\frac{r_e^3}{r^3}\sin\theta \tag{3.13}$$

$$B_\theta = B_o\frac{r_e^3}{r^3}\cos\theta$$

where r_e is the earth's radius and B_o is the magnitude of the field on the earth's surface at the geomagnetic equator. The resultant field strength is then given by

$$B = B_o\frac{r_e^3}{r^3}\sqrt{4-3\cos^2\theta} \tag{3.14}$$

The equation of a field line, in polar co-ordinates, is

$$\begin{aligned} r &= r_o\cos^2\theta \\ \varphi &= const \end{aligned} \tag{3.15}$$

where r_o is the distance from the centre of the earth at which the field line intersects the equatorial plane. Field lines are generally described by a dimensionless parameter, called the $L-value$. This is the maximum distance, in earth radii, of the field line from the earth's centre and is given by

$$L = \frac{r_o}{r_e} \tag{3.16}$$

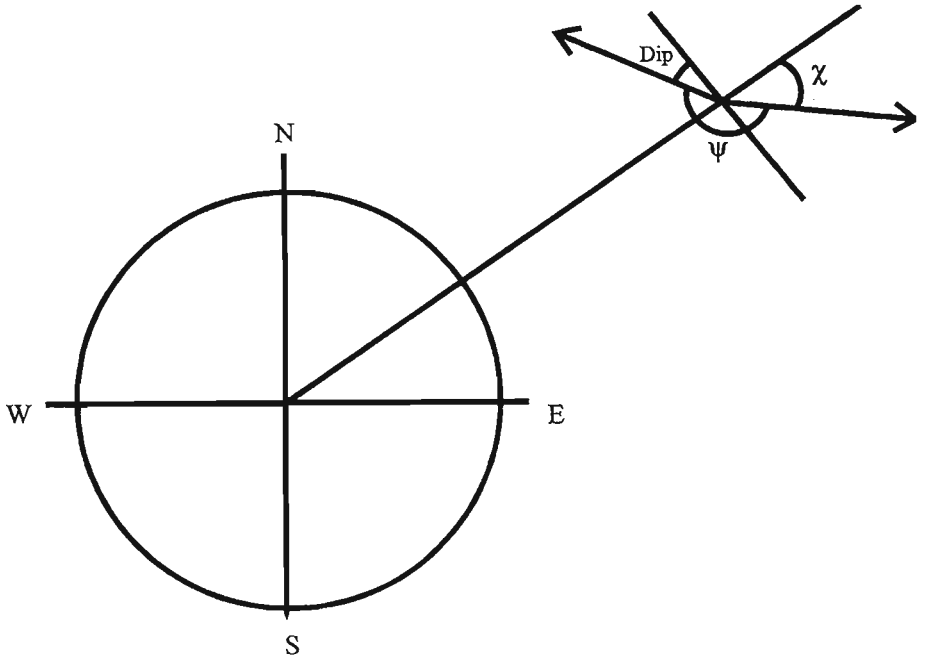

Figure 3.9: Geometry of the wave normal and magnetic dip angle.

Using equation (3.15) and (3.16), equation (3.14) can be rewritten as

$$B = \frac{B_o}{L^3} \frac{(4 - 3\cos^2\theta)}{\cos^6\theta} \tag{3.17}$$

To determine the phase refractive index, the angle between the wave normal and the magnetic field direction is needed. The wave normal, χ, used in the ray tracing equations is the measured relative to the radial direction. The magnetic field direction is given in terms of the dip angle. This is the angle between the magnetic field direction and the horizontal ($r = constant$) and is given by $\arctan(2\tan\theta)$. These angles are illustrated in figure 3.9.

As is shown in the figure, the angle (ψ) between the wave normal and the magnetic field is $\frac{3\pi}{2} - Dip - \chi$.

3.3.2 IGRF Model

The IGRF model is an empirical model that uses the assumption that there are no currents on the earth's surface. This is reasonably valid during quiet magnetic periods. Ampere's curl equation reduces to $\nabla \times \overrightarrow{H} = 0$. A scalar potential

therefore exists such that $\overrightarrow{H} = -\nabla\psi$ and hence $\nabla^2\psi = 0$. This can be solved in spherical polar co-ordinates (r,θ,ϕ) using separation of variables to give

$$\psi = r_e \sum_{l=0}^{n} \sum_{m=0}^{l} P_l^m(\cos\theta) \left(\frac{r_e}{r}\right)^{l+1} [A_l^m \cos m\phi + B_l^m \sin m\phi] \tag{3.18}$$

$P_l^m(\cos\theta)$ are the Legendre polynomials and A_l^m and B_l^m are the Gauss coefficients which can be determined empirically from magnetic field values recorded by ground based magnetometers. The value of n depends on the number of coefficients used. The magnetic field components are

$$\begin{aligned} B_r &= -\mu_o \frac{\partial\psi}{\partial r} \\ B_\theta &= -\frac{\mu_o}{r}\frac{\partial\psi}{\partial\theta} \\ B_\phi &= -\frac{\mu_o}{r\sin\theta}\frac{\partial\psi}{\partial\phi} \end{aligned} \tag{3.19}$$

If axial symmetry is assumed and if $n = 1$ then equation (3.19) reduces to equation (3.13). If the Gauss coefficients are determined empirically then geographic co-ordinates must be used (the geomagnetic co-ordinates are not known) and generally $n = 10$ resulting in 118 Gauss coefficients.

Field lines must be determined numerically as an analytical solution doesn't exist. This is done by determining the field components and their direction cosines at the starting point, moving an infinitesimal distance in the field line direction and repeating the procedure. The L-value is, once again, defined as the ratio of the longest radial distance of the field line to the earth radius. The geomagnetic latitude of a point on the earth's surface is found from the L-value of the field line passing through that point using equation (3.15). This may seem strange as equation (3.15) is not a valid equation for an IGRF field line but it does give the geomagnetic latitude once the L-value is known. The geomagnetic longitude is given by the difference between the geographic longitude of the field line at its furthest point and the geographic longitude of the magnetic meridian which is currently about $72W$.

The IGRF model has mainly been used to convert from geographic to geomagnetic co-ordinates and to determine L-values. Ray tracing using an IGRF model is difficult as the diffusive equilibrium density model depends on the magnetic model and, as can be seen from equation (3.5), is simplified if the field lines are described by an analytic equation. Some ray tracing has been done using an IGRF model (Kimura [1985]) and may be undertaken by us in future work.

3.4 Summary

The above models are used in two different ray tracing situations. The first considers whistlers received on a satellite at a low altitude (1400 km) and at low geomagnetic latitudes ($< 30^o$). These whistlers are assumed to be unducted and since the satellite is at a low altitude, equation (3.8) is used for the temperature model. Latitudinal density gradients are introduced using equation (3.11). The second considers the interaction between whistler mode waves and energetic electrons at middle latitudes ($\sim 50^o$). The whistlers are ducted and hence equation (3.12) must be used to introduce ducts into the density model. An isothermal temperature of 1600 K together with ion concentrations of $90\%O^+$, $8\%H^+$ and $2\%He^+$. This gives a diffusive equilibrium model that is the same as that used by Park [1972] which is matched, at 500 km, with a Chapman layer.

Chapter 4

Low Latitude Fractional-hop Whistlers

4.1 Introduction

Fractional-hop whistlers are whistlers received on satellites. This study will attempt to understand some characteristics of fractional-hop whistlers received on the ISIS2 satellite during October 1976. The altitude of this satellite was about 1400 km and the whistlers that will be considered in this study were received by the satellite at geomagnetic latitudes of less than 30^o and at local times of between 07:30 and 08:30. The geographic longitude of the satellite varied from 70^oW to 90^oW as the data were transmitted to ground at Quito, Ecuador. Many of the observed fractional-hop whistlers had coincident proton whistlers. Measurement of the cross-over frequency allows determination of the proton concentration at the satellite height (Gurnett et al [1965]). This information was used to determine the ion concentrations in the density models used in the ray-tracing calculations. A spectrogram showing a number of fractional-hop whistlers, together with proton whistlers, is shown in figure 4.1. The frequency range (y-axis) is from $0 - 5$ kHz and the time on the x-axis is about 5 s. The proton whistlers are the rising tones below about 500 Hz.

One of the goals of this study is to see whether it is possible, from the whistlers, to determine the position, on the ground, of the initiating atmospheric.

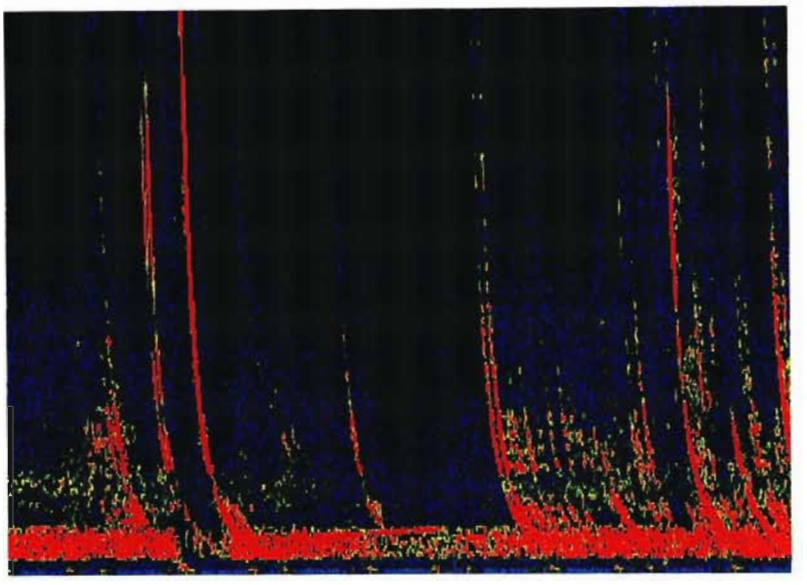

Figure 4.1: Spectrogram showing fractional hop whistlers received on the ISIS2 satellite. Time,on the x-axis, is 2.5 s and frequency, on the y-axis, is from 0 - 5 kHz. Proton whistlers can be seen below about 500 Hz.

4.2 Dispersion

If it is assumed that the wave is travelling tangential to the magnetic field direction then equation (2.4) reduces to $\mu^2 = R$ where R is given in equations (2.3). This can be further simplified by ignoring the ions, the 1 and the ω in the brackets of the numerator, giving

$$\mu^2 = \frac{\pi_e^2}{\omega\Omega_e} \tag{4.1}$$

The group velocity of the wave is given by $\frac{c}{\mu_g}$ where μ_g is the group refractive index defined as $\frac{\partial(\mu\omega)}{\partial\omega}$. The travel time is then given by the integral of the inverse of the group velocity over the path of the wave (for longitudinal propagation the ray direction and wave normal direction are the same and the $\cos\alpha$ in equation (2.12) can be ignored) and can be shown to be given by

$$t = \int_{path} \frac{\mu_g}{c} ds \simeq \frac{1}{2c} \frac{\langle \pi_e \rangle}{\langle \Omega_e \rangle^{\frac{1}{2}} \omega^{\frac{1}{2}}} \Delta s \tag{4.2}$$

where the brackets indicate an average value over the path. As can be seen from the above equation, the travel time is approximately proportional to the inverse square root of the frequency and can be written as

$$t = Df^{-\frac{1}{2}} \tag{4.3}$$

The term D in the above equation is what is referred to as the dispersion and f is the wave frequency in Hertz given by $f = \frac{\omega}{2\pi}$. The above relation was first determined by Eckersley [1935] and is known as the Eckersley relation. It is reasonably valid for frequencies much greater than the ion gyrofrequency and much less than the electron gyrofrequency. To determine the dispersion of a whistler, the time can be measured relative to an arbitrary origin. The gradient of the straight line graph of t vs $f^{-\frac{1}{2}}$ is then the dispersion and the extrapolation to infinite frequency gives the time of the initiating atmospheric. Previously the wave frequency has been an angular frequency. When considering dispersion the wave frequency will be in *Hertz* making the units of dispersion $\mathrm{s}^{\frac{1}{2}}$.

4.3 Analysis of ISIS2 Satellite Data

Hughes [1981] and Hughes and Rice [1997] studied the dispersion of fractional-hop whistlers received on ISIS2 at geomagnetic latitudes between 30^o and 0^o. Values for t and f were measured on the whistler traces with t relative to an arbitrary time origin. The dispersion was determined by plotting t against $f^{-\frac{1}{2}}$, fitting a straight line and calculating the gradient. They showed that the dispersion varied from about 4.5 $\mathrm{s}^{\frac{1}{2}}$ at a latitude of 30^o to 12 $\mathrm{s}^{\frac{1}{2}}$ at the equator. A second group of dispersions which varied from about 25 $\mathrm{s}^{\frac{1}{2}}$ at a latitude of 30^o to 12 $\mathrm{s}^{\frac{1}{2}}$ at the equator was also present. This is illustrated in figure 4.2. Most of the whistlers in figure 4.1 have dispersions that would fall into the lower dispersion branch. There is a whistler, about 1 s after the start of figure 4.1, that has a dispersion that would fall into the upper dispersion branch. The whistlers analysed in figure 4.2 were recorded between 11:58 and 12:10 UT on 26 October 1976. The satellite was at a geographic longitude of about 70^oW making the local time about 07:30.

The two dispersion branches are explained qualitatively by Hughes [1981] as being the result of fractional-hop whistlers from both hemispheres. The lower branch corresponding to those from the near hemisphere and the upper branch to those from the far hemisphere. In this study the explanation given by Hughes [1981] is tested by tracing signals from a point on the earth's surface to a satellite in the magnetosphere using the density and magnetic field models discussed in the previous chapter. Ray paths and travel times are calculated. The dispersion is

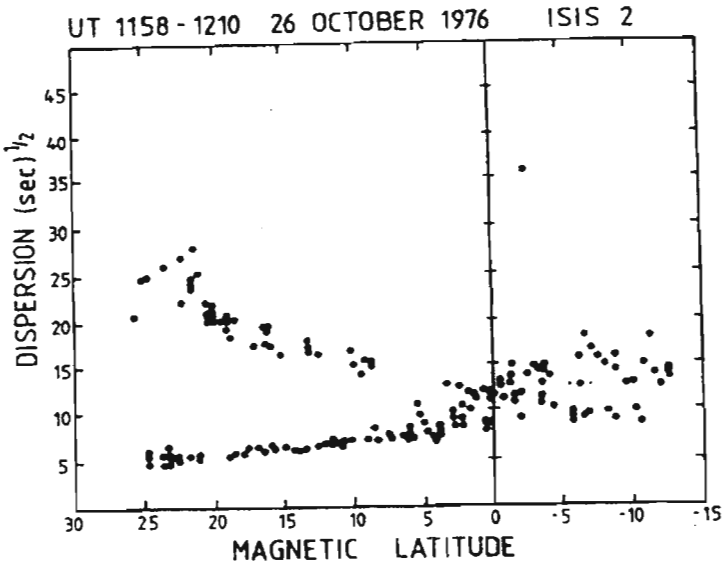

Figure 4.2: Whistler dispersion measured on ISIS2 (Hughes [1981]).

determined from the travel time. The results obtained from the ray tracing are compared with those obtained from the ISIS2 satellite data. In the ray tracing it has been assumed that the signals propagate in an unducted mode. This was assumed because the whistlers were observed almost continuously between latitudes of 0^o and 30^o without any discrete changes in dispersion. Smith and Angerami [1968] used the discreteness of the whistler dispersion as one of the tests for the ducting of whistlers received on the OGO-1 satellite. Tanaka and Hayakawa [1985] also showed that, at low latitudes, ducts need to have density enhancements of 100% or more to trap whistlers due to the large angle between the wave normal direction and the magnetic field direction, along which the ducts are aligned. Cerisier [1973] analysed artificial narrow-band signals from a ground transmitter received on the FR-1 satellite and found no evidence of ducted propagation below $L = 1.7$. The L-value of ISIS2 during the period of interest varies from $L = 1.22$ at the equator to $L = 1.62$ at 30^o.

4.4 Initial Conditions for Ray Tracing

The fractional-hop whistlers received on board the ISIS2 satellite were generated by an impulse (lightning strike) in the earth's atmosphere. In this study it is assumed that the impulse occurs on the earth's surface and that the signal propagates in a straight line, at an angle β to the vertical, until it reaches the base of

the ionosphere. On reaching the base of the ionosphere the signal is refracted into the ionosphere and propagates in an unducted mode until it reaches the satellite at a height of 1400 km, the position of the satellite having been predetermined. It has been suggested that ray tracing through the lower ionosphere is not valid and that either a full wave model should be used as done by Tsuruda [1972] or the signal should be started at an altitude of about 500 km with a vertical wave normal.

A problem with ray tracing through the lower ionosphere is that ray tracing assumes that the phase refractive does not change much over a distance of the order of a wavelength. In the lower ionosphere ($\sim$ 120 km) the phase refractive index of a 2 kHz wave is about 20 giving a wavelength of 7500 m. At this altitude the phase refractive index changes by about 13% over this distance. For a 10 kHz signal the wavelength at an altitude of about 120 km is about 3000 m and the change in phase refractive index is about 8%. Although these changes are not insignificant, they reduce rapidly to less than 1% at 250 km. What is of particular interest in this study is the wave travel time and, to a lesser extent, the ray path. Starting at 500 km would necessitate approximating the travel time through the lower ionosphere. Ray tracing through this region gives an idea of the travel time and, since this time is quite small, the error introduced is probably negligible. Some authors such as Thomson [1987] and Kimura [1985] have ray traced through the lower ionosphere and have obtained reasonable results.

The refractive index in the ionosphere is much greater than in the atmosphere and the wave is strongly refracted on entering the ionosphere. Snell's law (equation (4.4)) is used to determine the refracted angle. The refractive index in the ionosphere depends on the wave normal angle and the refractive index in the atmosphere is unity.

$$\sin \chi_i = \mu \left(\chi_{refr} \right) \sin \chi_{refr} \tag{4.4}$$

Figure 4.3 illustrates the geometry of the initial conditions. The impulse is on the earth's surface at a point A ($r = R_e$) and the signal propagates with an initial wave normal angle β. The point at which the signal intersects the base of the ionosphere is at B. If the point A is at a latitude of λ' and if the atmospheric thickness is h, then B will have a latitude of $\lambda' - \alpha$ where α is given by

$$\alpha = \arccos \left[\frac{R \sin^2 \beta \mp \cos \beta \sqrt{(R+h)^2 - R^2 \sin^2 \beta}}{(R+h)} \right] \tag{4.5}$$

The wave normal at B w.r.t. the radial direction is $\chi_i = \beta - \alpha$ and the distance of B from the origin is $r = R_e + h$. Using equation (4.4) the refracted angle, χ_{refr},

is determined. The initial conditions for the ray tracing (using the co-latitude rather than the latitude) are

$$\begin{aligned} r_o &= R_e + h \\ \lambda_o &= 90^o - (\lambda^{'} - \alpha) \\ \chi_o &= \chi_{refr} \end{aligned} \tag{4.6}$$

The signal is then traced until it reaches the altitude of the satellite. If, once it reaches this altitude, it is not at the same latitude as the satellite, the initial conditions are varied until both the final altitude and latitude of the wave coincide with the predefined position of the satellite. The signal is regarded as having reached the satellite if its final latitude is within 0.0005^o of the predefined satellite latitude. At an altitude of 1400 km this corresponds to a distance of 68 m.

The initial conditions that can be varied are the point A, the wave normal angle β or both. This study concerns frequencies between 2 kHz and 10 kHz and it was initially decided that the position A should be such that a 6 kHz signal would have an initial wave normal angle, β, of 0^o. The initial position, A, is therefore varied until the 6 kHz signal, started vertically, reaches the satellite. For frequencies other than 6 kHz, the initial point is the same but the initial wave normal angle, β, is varied until these signals reach the same predefined satellite position. This results in different ionospheric entry points for different frequencies. Since the signals propagate in an unducted mode, this also means that different frequencies propagate along different paths. This allows determination of the ray paths and travel times of signals, with frequencies between 2 kHz and 10 kHz, received on the satellite at 1400 km and starting at a common point A on the ground.

The above procedure was repeated for satellite latitudes of 0^o, 5^o, 10^o, 15^o, 20^o, 25^o and 30^o and for signals starting in both hemispheres.

The effect of moving the point A such that the 6 kHz signal does not start vertically was then also studied. This was firstly done to see what effect this would have on the ray paths and travel times, but was also done to see if it is possible to establish the approximate position of the initiating atmospheric from characteristics of the low latitude whistlers.

4.5 Ionospheric and Magnetospheric Densities

The density model, as explained in Chapter 4, is a Chapman layer for the ionosphere matched, at an altitude of 500 km, with a diffusive equilibrium model

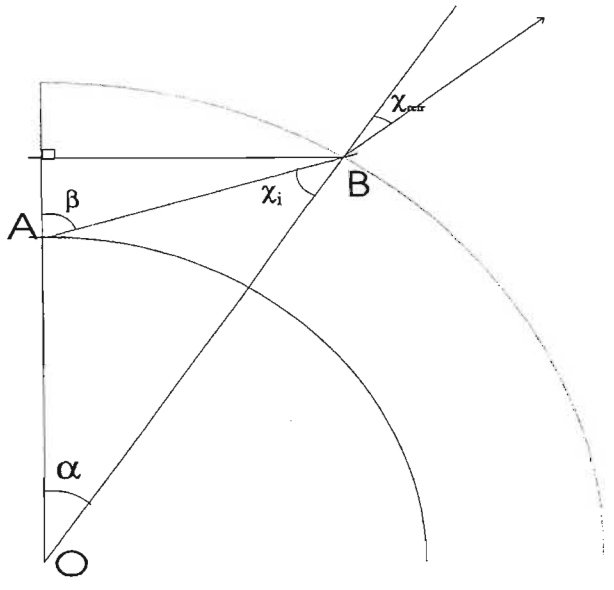

Figure 4.3: Geometry of the ionospheric entry.

for the magnetosphere. In order to calculate the actual ion and electron densities, values for these, and for the temperature, are needed at a reference height. The DE-1 model, used by Park [1972], uses a reference height of 1000 km with ion concentrations of 0.90 O^+, 0.08 H^+ and 0.02 He^+ and an isothermal temperature of 1600 K.

Gurnett et al [1965] showed that by measuring the cross-over frequency the approximate proton concentration can be calculated from

$$\alpha_p = \frac{n_p}{n_e} = \frac{264}{255}\left[1 - \left(\frac{f_x}{f_p}\right)^2\right] \tag{4.7}$$

where n_p and n_e are the proton and electron densities respectively, f_x is the cross-over frequency and f_p is the proton gyrofrequency. Using this technique Hughes [1981] showed that the average proton concentration at the ISIS2 satellite height varied from about 0.77 at 30° to about 0.88 at the equator. This is shown in figure 4.4 for an ISIS2 pass on day 278 (1976) between 1511 UT and 1523 UT.

In this study the latitudinal variation in proton concentration was ignored and a concentration of $0.81H^+$ at the satellite altitude was used as an average. The ion concentrations at the reference height of 500 km were then chosen to give this concentration at the satellite height. The ion concentrations at the reference height were $0.84O^+$, $0.09H^+$ and $0.07He^+$. Equation (3.8) was used for the

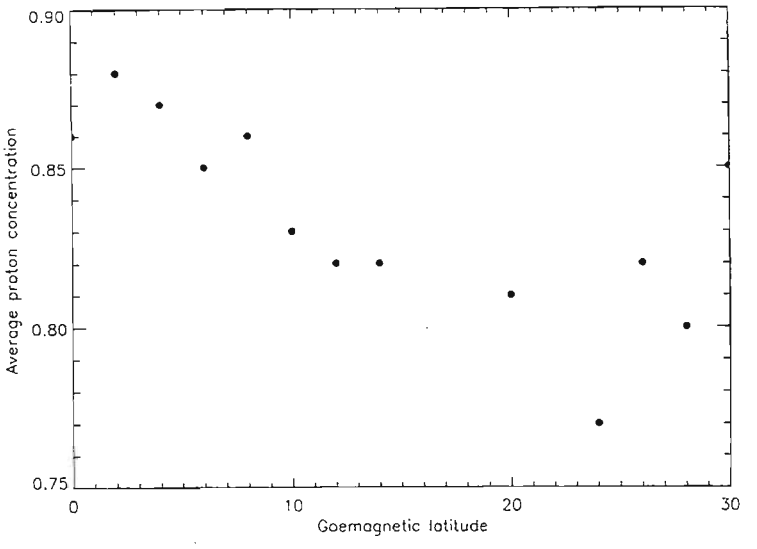

Figure 4.4: Average fractional proton concentration at $1400km$ at geomagnetic latitudes between 30^o and 0^o measured on ISIS2 during October 1976.

temperature model with a 1200 K temperature at the reference height and a temperature gradient of 1.85 K.km^{-1}. Using this non-isothermal temperature model means that equations (3.9) and (3.10) are used to determine the 'temperature modified geopotential height'.

The Chapman layer, used to model the ionosphere, is matched with the diffusive equilibrium model at an altitude of 500 km. Both the ion densities and their gradients are matched. As a result of quasi-neutrality, the electron density and its gradient are also matched once the ions are matched. To match the two models, it was assumed that the temperature in the ionosphere was isothermal and the actual temperature value was chosen such that matching was possible. This results in a discontinuous temperature model but does not introduce any significant errors. The ionospheric temperature was 843 K. The advantage of this technique is that by varying the ionospheric temperature, the height of maximum electron density, known as the$F2$ height, can be varied. An ionospheric temperature of 843 K gives an $F2$ height of about 290 km. Figure 3.5 shows an example of the ion and electron density profiles matched in the above way.

The only parameters that still need to be determined are the reference electron density and its latitudinal gradient. This was done by initially using reference electron densities with no latitudinal dependence. The value of the reference electron density was then varied until a 6 kHz signal, received by a satellite at the geomagnetic equator, had the expected dispersion ($\sim 12\ s^{\frac{1}{2}}$). This gave a first

guess at the electron density which had to be modified slightly on the introduction of latitudinal density gradients. Other satellite positions were also used to see how the dispersion varied with latitude. Frequencies other than 6 kHz were not considered.

4.6 No Latitudinal Gradients

The latitudinal gradients were ignored in order to get an idea of what reference electron density, and hence what actual density profile, should be used by the ray tracing model to give results similar to those obtained from analysis of the ISIS2 data. As described in section 4.4, the position of the impulse on the earth's surface is varied until a 6 kHz signal, started vertically, reaches the satellite at an altitude of 1400 km above the geomagnetic equator. Frequencies other than 6 kHz were not considered in this case. Analysis of the ISIS2 data gave a dispersion of about 12 $s^{\frac{1}{2}}$ for a satellite at the geomagnetic equator. To get the same dispersion using ray tracing it was found that a reference electron density of 1.48×10^5 cm^{-3} was needed. This reference electron density results in a $F2$ density of 5.8×10^5 cm^{-3} at an altitude of 290 km. Instead of referring to the electron density in terms of el.cm^{-3} the plasma frequency is often used. A $F2$ electron density of 5.8×10^5 cm^{-3} corresponds to a plasma frequency, known as f_oF2, of 6.8 MHz.

The above procedure is repeated for satellite latitudes of 30^o, 25^o, 20^o, 15^o, 10^o and 5^o, the dispersion being calculated at each latitude using $D = tf^{\frac{1}{2}}$. The procedure is again repeated using the same satellite latitudes but with impulses in the far hemisphere. In this case the signal has to propagate across the geomagnetic equator to reach the satellite.

Figure 4.5 shows the dispersion obtained using ray tracing, plotted against the geomagnetic latitude of the satellite. Although this looks remarkably similar to figure 4.2 it differs in that the dispersion of the signals originating in the near hemisphere (lower branch) and received by the satellite at the higher latitudes are greater than those obtained through analysis of the ISIS2 satellite data. This difference can by explained by the neglect of latitudinal gradients resulting in slightly greater electron densities, and hence refractive indices, at the higher latitudes than might be expected. The dispersions of the signals originating in the remote hemisphere are very close to those obtained by Hughes [1981] except for, once again, the higher satellite latitudes where the dispersion is slightly greater than expected. This can also be explained by the neglect of latitudinal density gradients.

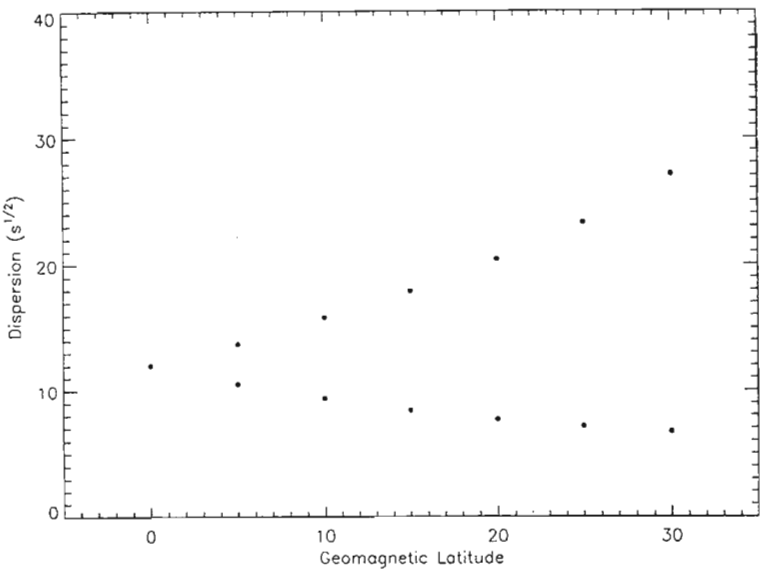

Figure 4.5: Whistler dispersion against latitude of the receiving satellite for a density model with no latitudinal gradients.

4.7 Latitudinal Gradients

Latitudinal gradients are introduced using equation (3.11) to model the reference electron densities. The actual gradient depends on the value chosen for E and on the reference latitude (θ_o'). A value for E of 0.5 was chosen with a reference latitude of 20^o. These are the same as the values used by Thomson [1987]. This results in the reference electron density varying from 1.1×10^5 cm^{-3} at a geomagnetic latitude of 20^o to 1.7×10^5 cm^{-3} at the geomagnetic equator. These reference densities give $F2$ densities of 4.4×10^5 cm^{-3} ($f_oF2 = 5.9$ MHz) at 20^o and 6.7×10^5 cm^{-3} ($f_oF2 = 7.3$ MHz) at the equator with an $F2$ height of 290 km. This is illustrated in figure 4.6 which shows electron density profiles against altitude for geomagnetic latitudes of 20^o and 0^o. The ion density profiles are as in figure 3.5. A contour plot showing the latitudinal variation of electron density is shown in figure 3.6.

In this case the dispersion was obtained by considering frequencies of 2 kHz, 4 kHz, 6 kHz, 8 kHz and 10 kHz. The actual whistler dispersion was obtained by plotting t vs $f^{-\frac{1}{2}}$ and determining the gradient. As discussed above, all the frequencies start at the same point on the earth's surface with different initial wave normal angles (β) and hence enter the ionosphere at different points and travel along different paths. Figure 4.7 shows the starting latitude against satellite

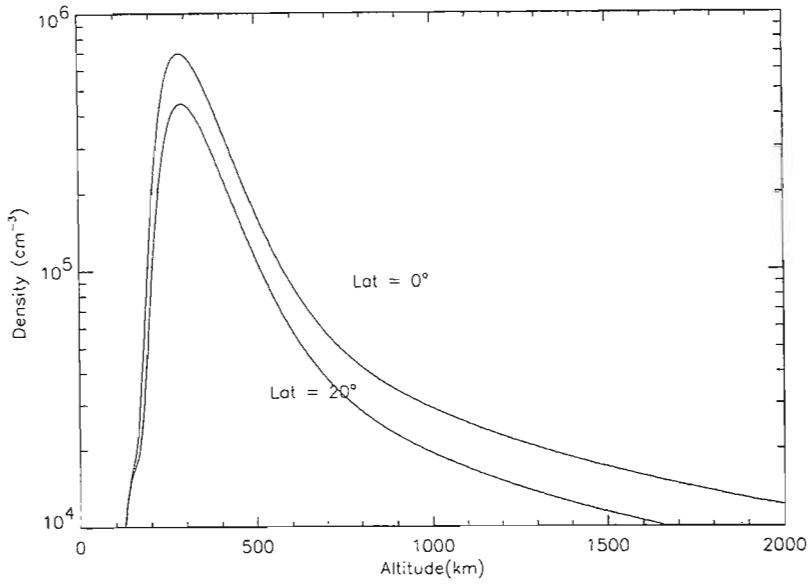

Figure 4.6: Density profiles at geomagnetic latitudes of 20^o and 0^o.

latitude for density models with and without latitudinal gradients. The crosses are for the case where latitudinal density gradients are ignored while the dots represent the case where latitudinal density gradients are included. As is shown in the figure, the rays traced through a density model without latitudinal gradients start at a slightly lower latitude (closer to the satellite latitude) than in the case where latitudinal density gradients are included. The inclusion of latitudinal density gradients therefore seems to increase the curvature of the ray paths.

The starting latitudes shown in figure 4.7, because of the initial conditions used in the ray tracing, are the same as the ionospheric entry point for the 6 kHz signal. For frequencies other than 6 kHz, the initial wave normal angle (β) is not vertical and hence the ionospheric entry latitude is not the same as the starting latitude. For signals originating in the same hemisphere as the satellite, the greatest initial wave normal angles occurred for a satellite at the equator with the 10 kHz signal having an initial wave normal angle of -5.6^o and the 2 kHz signal one of 5.7^o. This resulted in ionospheric entry points that varied by only 0.17^o. This is illustrated in figure 4.8 which shows ionospheric entry latitude against satellite latitude for signals originating in the same hemisphere as the satellite and for frequencies of 2 kHz (crosses) and 10 kHz (dots). The entry points for the two frequencies are barely distinguishable expect for low satellite latitudes.

For signals originating in the hemisphere remote from the satellite, the variation in initial wave normal angle, and hence ionospheric entry point is much greater.

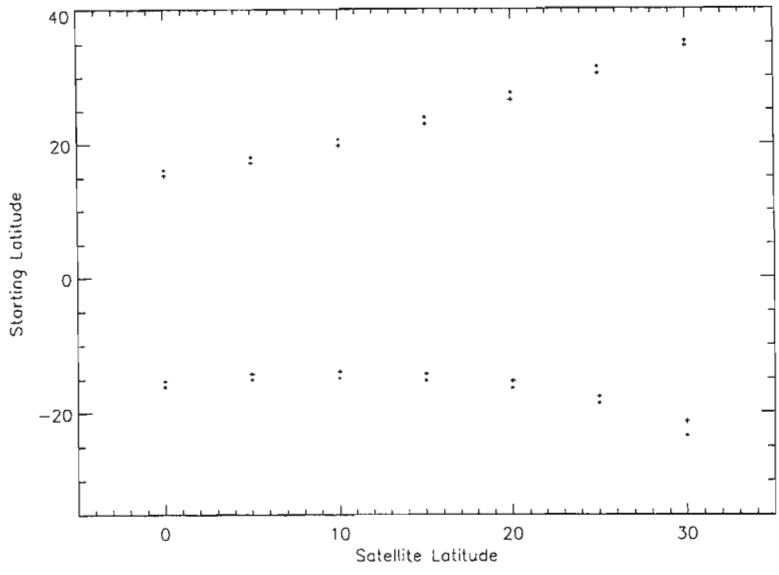

Figure 4.7: Starting latitude of signal versus latitude of receiving satellite for density models including and excluding latitudinal density gradients.

For a satellite at a geomagnetic latitude of 30° the initial wave normal angle varied from 42° for a frequency of 10 kHz to −70° for a frequency of 2 kHz. This results in ionospheric entry points that vary, in latitude, by 3° and, in distance, by over 300 km. This is illustrated in figure 4.9 which shows the ionospheric entry latitudes against satellite latitude for signals originating in the far hemisphere and for frequencies of 2 kHz (crosses) and 10 kHz (dots). The ionospheric entry latitudes for frequencies between 2 kHz and 10 kHz fall between these two limits. The difference is largest for a satellite at 30° and decreases as the satellite approaches the equator. The ionospheric entry points also decrease in latitude as the satellite moves from 30° to 10° but then start increasing again. This is because for satellite latitudes between 30° and 10°, the signals reach the satellite after having already crossed the satellite altitude. For satellite latitudes below 10° the signals reach the satellite without initially crossing the satellite latitude and hence start at slightly higher latitudes.

The different ionospheric entry points result in different path lengths for different frequencies. For a satellite at 30° and a source in the opposite hemisphere, the path length of the 2 kHz signal is 8084 km while that of the 10 kHz signal is 9278 km. This is illustrated in figure 4.10 which shows the ray paths for 2 kHz and 10 kHz signals received on a satellite at an altitude of 1400 km and a geomagnetic latitude of 30°. Both signals start at the same latitude (−23.4°) but enter the ionosphere at different latitudes. The figure also shows the ray paths for the

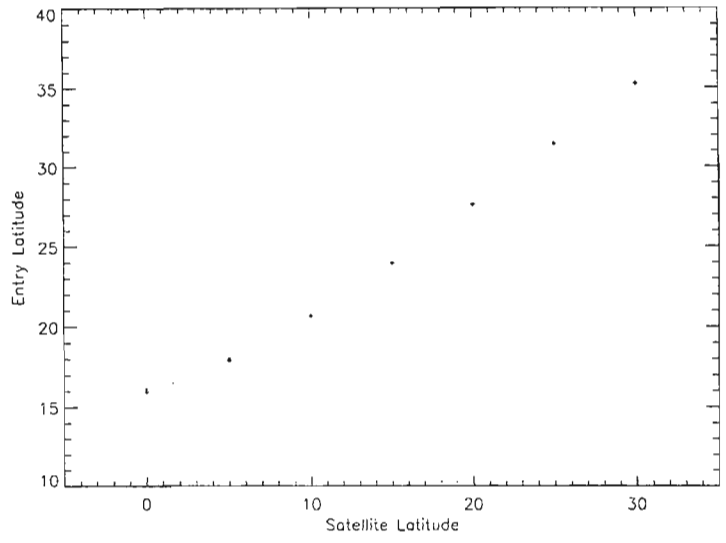

Figure 4.8: Ionospheric entry latitude against satellite latitude for signals originating in the same hemisphere as the satellite.

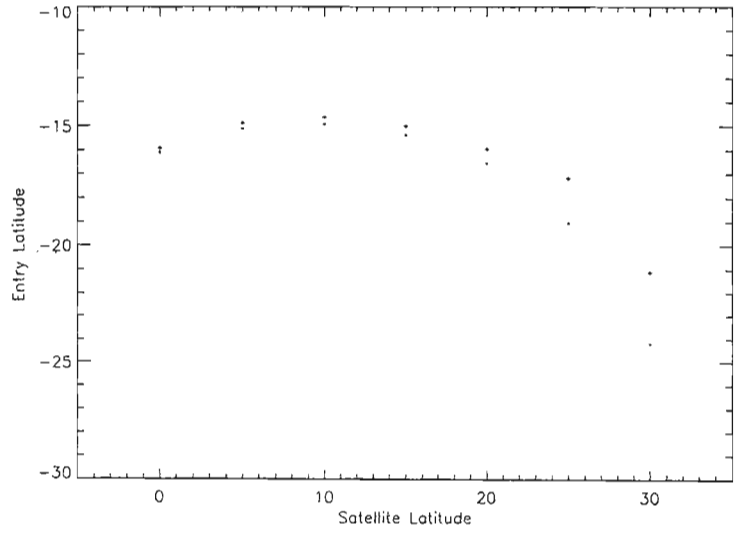

Figure 4.9: Ionospheric entry latitude against satellite latitude for signals originating in the hemisphere remote from the satellite.

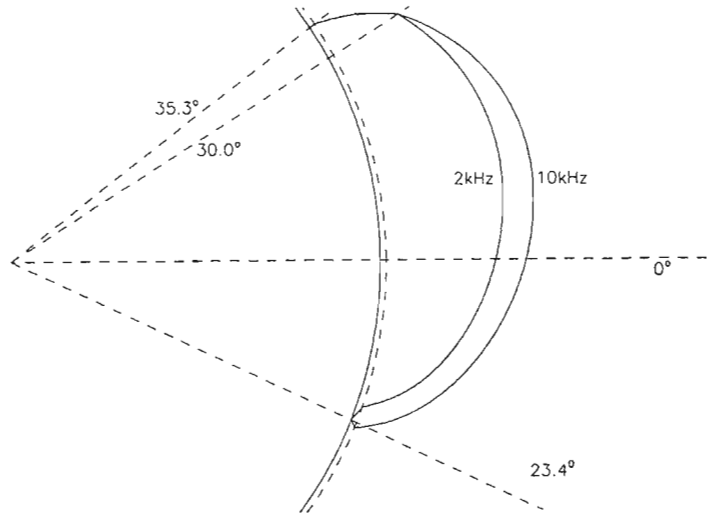

Figure 4.10: Ray paths of 2 kHz and 10 kHz signals starting at a latitude of -23.4^o and 32.3^o and reaching a satellite at an altitude of 1400 km and latitude of 30^o.

signals originating (at 35.3^o) in the same hemisphere as the source. The ray paths for both the 10 kHz and 2 kHz signals are drawn but are indistinguishable.

One of the assumptions of the Eckersley relation, discussed in section 4.2, is that the path is the same for all wave frequencies. As shown above, this is not the case in this study. The distance travelled by the 10 kHz signal originating in the far hemisphere and received on the satellite at a latitude of 30^o was 13% greater than the distance travelled by the 2 kHz signal. Despite this the dispersion of these whistlers still obeys the Eckersley relation fairly well. This is illustrated in figure 4.11 which shows a plot of travel time (t) against $f^{-\frac{1}{2}}$ for a satellite latitudes of 30^o, 20^o and 10^o and whistler sources in the far hemisphere.

The dispersion is the gradient of each straight line and as can be seen the points lie very close to the straight line. The reason for this is that although the higher frequencies travel greater distances than the lower frequencies, they propagate through regions of lower electron density and hence lower refractive indices. This increases their velocity and reduces their travel time giving dispersions that correspond to Eckersley's relation.

The results of the ray tracing, using the density model with latitudinal density gradients, are shown in figure 4.12. The dispersions of the signals originating in the near hemisphere were found to vary from 4.5 $s^{\frac{1}{2}}$ at 30^o to 11.7 $s^{\frac{1}{2}}$ at the

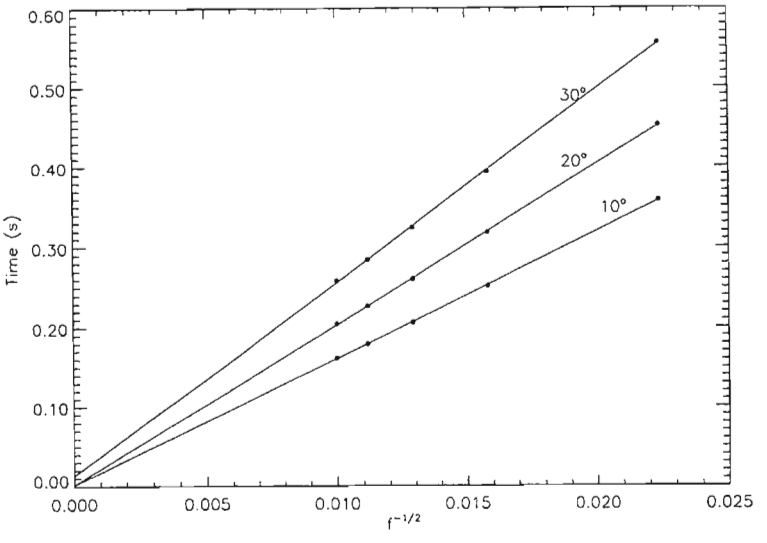

Figure 4.11: Plots of travel time against inverse square root of the wave frequency for satellite latitudes of 30°, 20° and 10° and signals generated in the remote hemisphere. The gradient of each straight line gives the dispersion.

equator. The dispersions of those originating in the far hemisphere varied from 25 $s^{\frac{1}{2}}$ at 30° to 11.7 $s^{\frac{1}{2}}$ at the equator. These results compare very well with those obtained by Hughes [1981] (discussed in section 4.3) and seem to indicate that the magnitude of the dispersion depends on the actual electron density while the gradient of the dispersion branches can be explained by the latitudinal gradient in electron density.

4.8 Whistler Echoes

A third group of whistlers with dispersion between 34 $s^{\frac{1}{2}}$ at the geomagnetic equator and 47 $s^{\frac{1}{2}}$ at a geomagnetic latitude of 30°, were also noticed by Hughes [1981]. Figure 4.13 shows an ISIS2 pass on 13 October 1976 between 1316 UT and 1328 UT in which these whistlers were observed. It also shows dispersions corresponding to one of the lower branches discussed above. The other lower dispersion branch is probably missing because there may have been no lightning activity in the opposite hemisphere.. The upper dispersion branch was interpreted as being whistlers which originate in the northern hemisphere and are received by the satellite after reflecting in the south. If the dispersions of the two lower branches are D_1 and D_2 (D_2 being the greater of the two dispersions) then the

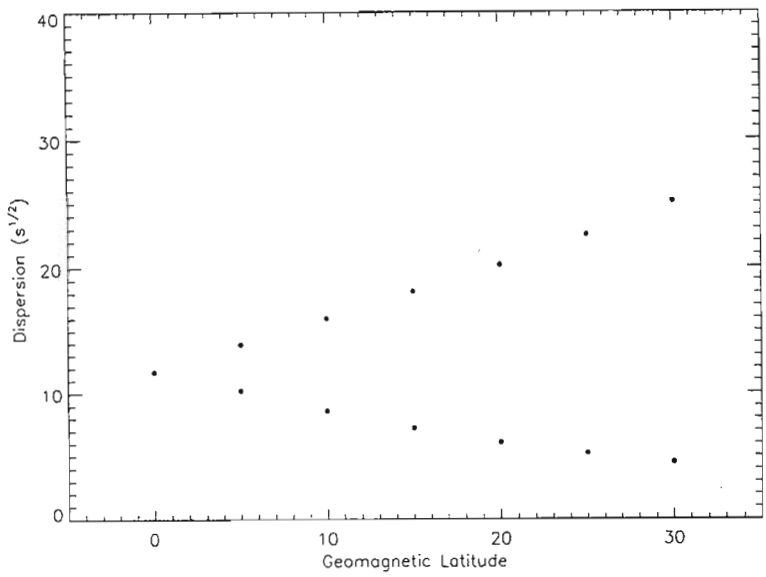

Figure 4.12: Whistler dispersion against geomagnetic latitude for a density model with latitudinal gradients.

dispersion of the upper branch, at the same satellite latitude, is very close to $D_1 + 2D_2$. This satisfies one of the criteria used by Smith and Angerami [1968] to test whether a signal has been ducted or not. The two lower dispersion branches have, however, already been shown to be almost certainly unducted signals and this study will attempt to see if the higher dispersions can be explained in the same way.

To model the whistlers with the higher dispersions, signals were traced, in an unducted mode, with initial conditions determined in the same way as before. The density and magnetic field models are identical to those used in the previous section. On reaching the lower border of the ionosphere in the opposite hemisphere the signals reflect and travel up until they reach the altitude of the satellite. The condition for reflection is that the component of the wave number $\left(\overrightarrow{k}\right)$ parallel to the boundary must be conserved and can be written as Snell's law

$$\mu(\chi_i)\sin(\chi_i) = \mu(\chi_r)\sin(\chi_r) \tag{4.8}$$

Equation (4.8) clearly shows that the refractive index for the reflected wave depends on the reflected wave normal (χ_r) and that of the incident waves depends on the incident wave normal angle (χ_i).

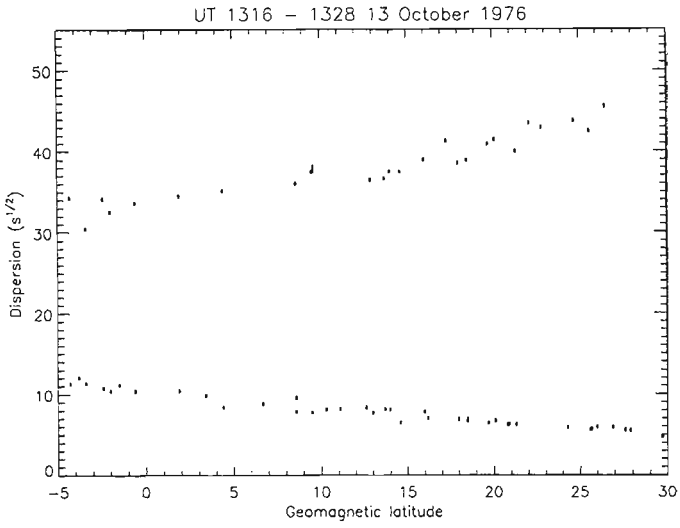

Figure 4.13: ISIS 2 pass showing whistler echoes.

If, once the signal has reached the satellite altitude, the final latitude is not the same as the predefined satellite latitude, the initial conditions are varied, in the same way as before, until this is satisfied. Frequencies of 2 kHz, 4 kHz, 6 kHz, 8 kHz and 10 kHz were used with the dispersion obtained by fitting a straight line to the plot of t vs $f^{-\frac{1}{2}}$ and determining the gradient.

Ray paths of signals received, after echoing, by satellites at 5^o and 30^o are shown in figure 4.14. The left hand frame shows 2 kHz and 10 kHz signals starting at 9.6^o, reflecting in the opposite hemisphere and being received by a satellite at 5^o. The 2 kHz signal is the one entering the ionosphere at the lower latitude. The right hand frame shows 4 kHz and 10 kHz signals starting at a latitude of 12^o, reflecting in the opposite hemisphere and being received by a satellite at 30^o. A 2 kHz signal is not shown in the right hand frame as it is magnetospherically reflected (MR) and doesn't reach the satellite.

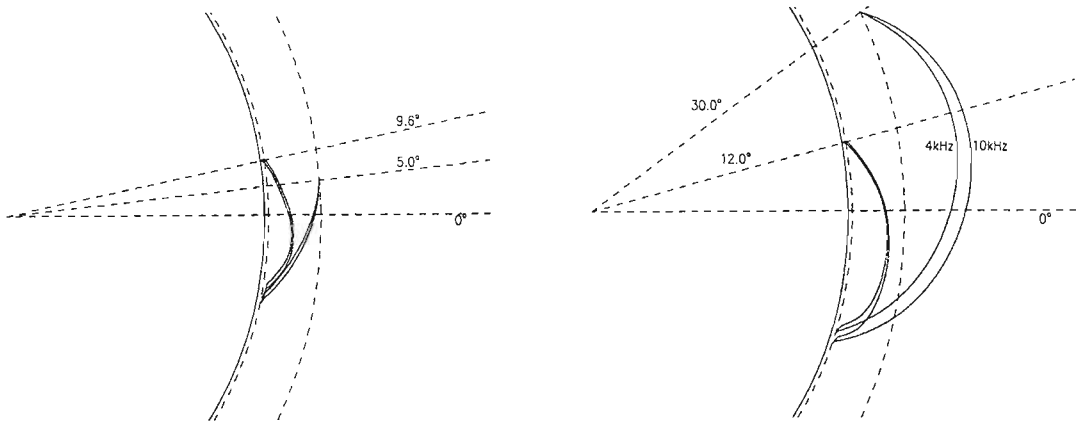

Figure 4.14: Whistler echo ray paths for a satellite at 5^o and at 30^o.

Figure 4.15 is a plot of travel time (t) against $f^{-\frac{1}{2}}$ for satellite latitudes of 30^o, 20^o and 10^o and shows that even though the different frequencies follow very different paths, the points all lie very close to a straight line, obeying Eckersley's relation. As discussed earlier, if the wave travel time is obtained experimentally and is measured relative to an arbitrary time origin, the time of the initiating spheric can be obtained by plotting t against $f^{-\frac{1}{2}}$ and extrapolating the best fit straight line to infinite frequency. The time is therefore given by the intercept on the time axis. When ray tracing, the travel time is measured relative to the initiating spheric. The straight lines should therefore all pass through the origin. Figure 4.15 shows that for satellite latitudes of 20^o and 10^o this is almost the case but for a satellite latitude of 30^o the straight line intersects the time axis at 50 ms. A similar result can be seen in figure 4.11 for a satellite latitude of 30^o except that intercept is at about 10 ms. This means that although the fractional hop whistlers seem to obey Eckersley's relation, the time of the initiating atmospheric obtained experimentally could be as much as 50 ms too small for whistler echoes and about 10 ms too small for direct signals from the remote hemisphere observed on the satellite at higher latitudes. This amounts to about an 8% error in travel time at 6 kHz in the case of whistler echoes but only a 3% error at 6 kHz in the case of the direct signal from the opposite hemisphere.

The whistler echo dispersions calculated using ray tracing varied from 33.5 $s^{\frac{1}{2}}$ at the equator to 47.0 $s^{\frac{1}{2}}$ at a latitude of 30^o. This is shown in figure 4.16 which also shows the lower dispersion branch as in figure 4.13. These results are very similar to those obtained by Hughes [1981].

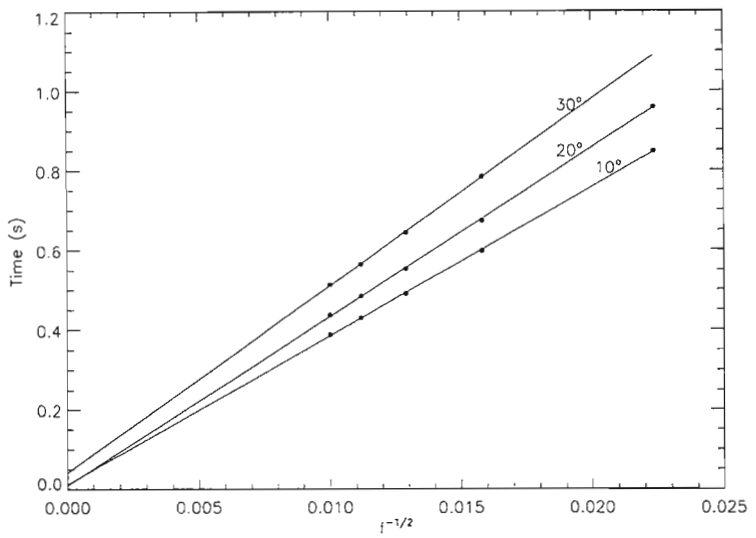

Figure 4.15: Plots of travel time against inverse square root of frequency for whistler echoes received on the satellite at latitudes of 30^o, 20^o and 10^o.

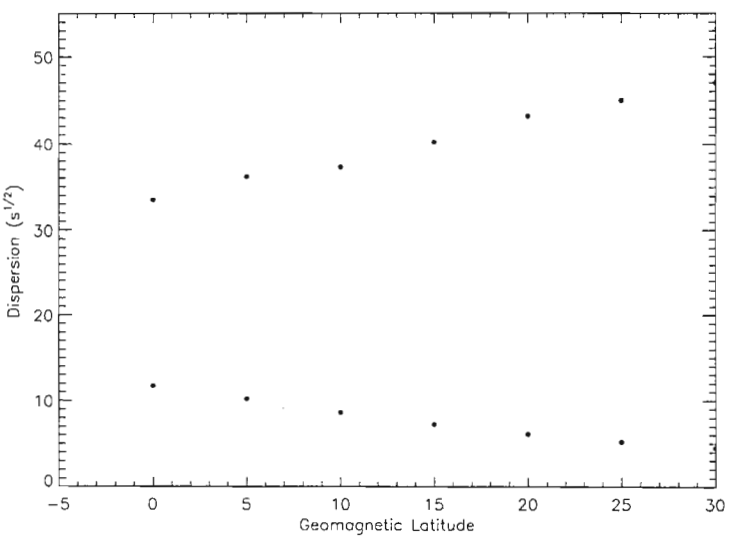

Figure 4.16: Whistler echo dispersions calculated by ray tracing.

4.9 Effect of Ions

The inclusion of ions in the density models means that transverse propagation is possible below the lower hybrid resonance frequency. If the wave normal angle of a downgoing wave rotates until perpendicular to the magnetic field direction, the signal will reflect. This is illustrated in figure 4.17. The left hand frame shows 10 kHz and 2 kHz signals starting at -27^o. The 10 kHz signal is received on the satellite at 33^o while the 2 kHz signal reflects above the satellite. It was found that all frequencies between 2 kHz and 10 kHz were able to reach a satellite in the remote hemisphere at geomagnetic latitudes less than 33^o. The data from the ISIS2 satellite was collected at geomagnetic latitudes between 0^o and 30^o. Whistlers from the remote hemisphere showed continuous frequency ranges between 2 kHz and 10 kHz at all of these latitudes. Data collected at latitudes above 33^o was not available and hence it wasn't possible to confirm that the lower frequencies would be reflect above the satellite at these latitudes.

The right hand frame shows 2 kHz and 10 kHz signals starting at 12^o and reflecting in the opposite hemisphere. Once again the 10 kHz signal is received on the satellite at 30^o while the 2 kHz signals reflects.

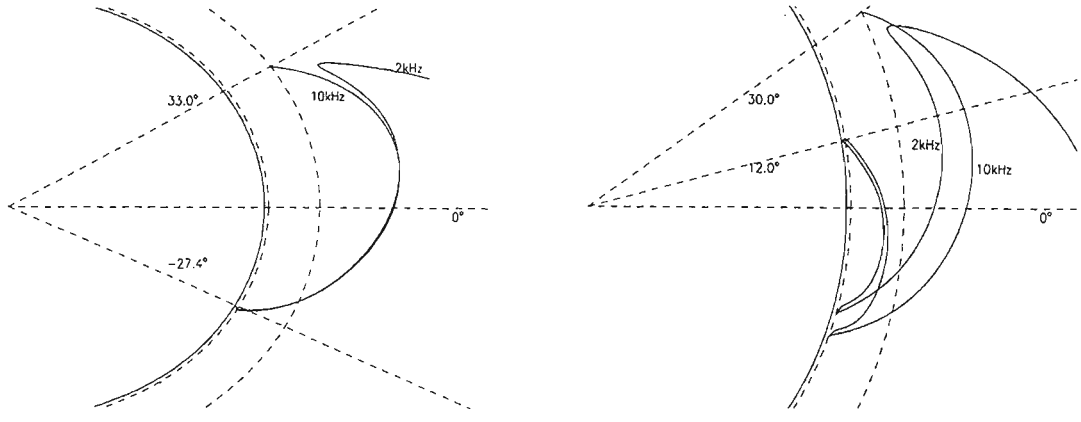

Figure 4.17: Ray paths showing Lower Hybrid Reflection of the 2kHz signal above the satellite

Figure 4.18 is a spectrogram showing whistlers observed on the ISIS2 satellite on 13 October 1976 when at a geomagnetic latitude of 30^o. The frequency range, on the y-axis, is 0 kHz -10 kHz and the time, on the x-axis is 5 s. Whistlers from both hemispheres and whistler echoes are present. The whistler echoes are clearly missing frequencies below about 4 kHz which may indicate, as discussed above, Lower Hybrid Resonance (LHR) reflection above the satellite. The whistlers from

the remote hemisphere, one on the left hand side of the frame and two on the right, show no signs of LHR reflection above the satellite as expected.

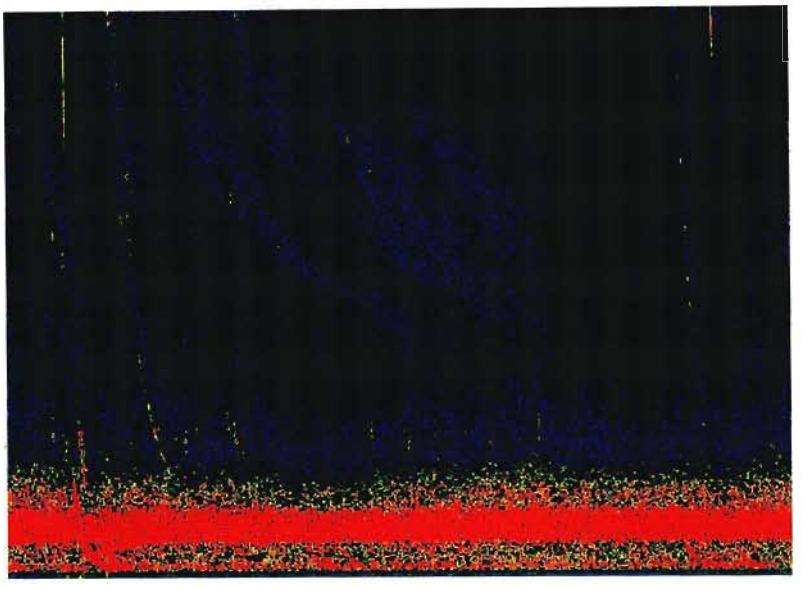

Figure 4.18: Spectrogram of whistlers received on the ISIS2 satellite on 13 October 1976 when at a geomagnetic latitude of 30^o. Whistlers from both hemispheres and echoes are present. The frequency scale, on the y-axis, is 0 - 5 kHz and the time scale, on the x-axis, is 2.5 s.

4.10 Source Position

The ray paths and travel times obtained in the previous sections were determined using a 6 kHz signal with a vertical wave normal. The position of the initiating atmospheric, or lightning strike, is therefore directly below the ionospheric entry point of the 6 kHz signal. The above restriction was made for simplicity and is certainly not a necessary condition for a signal to be received on the satellite. Figure 4.19 shows the variation in the ionospheric entry latitude with initial wave normal angle (β in figure 4.3) for a 6 kHz signal received on a satellite at 30^o (signals from both hemispheres) and at 0^o. An initial wave normal angle of 90^o means the signal is tangential to the earth's surface at the source position. An initial wave normal angle of greater than 90^o is therefore not possible. It has been assumed that the signal propagates directly from the source to the ionospheric entry point. It is, however, possible that the signal may reflect from the ionosphere and ground and may enter the ionosphere at a point that would

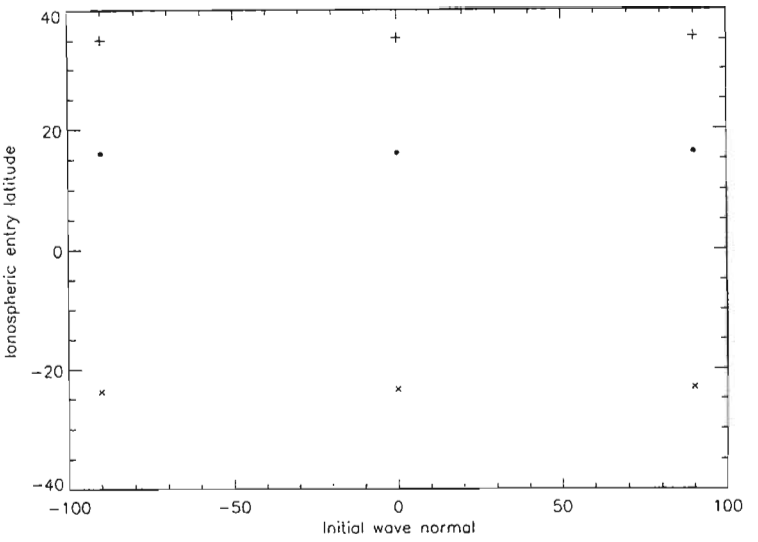

Figure 4.19: Variation of ionospheric entry point of a 6kHz signal started at different points on the earth's surface.

be below the horizon when viewed from the source position. This signal would however be considerably weaker than the direct signal as it will have travelled further and would have experienced losses on reflection.

In figure 4.19, the plus signs are for a satellite at 30^o and a source in the same hemisphere, the crosses are for a satellite at 30^o and a source in the opposite hemisphere and the dots are for a satellite at the equator. For an ionosphere height of 100 km, an initial wave normal angle of 0^o gives a source position directly below the ionospheric entry point, one of -90^o gives a source position 10^o (1110 km) closer to the equator and one of 90^o gives a source position 10^o further from the equator. It is clear from figure 4.19 that the ionospheric entry points are almost independent of source position. For a satellite at 30^o the ionospheric entry latitude of a wave, originating in the same hemisphere, with an initial wave normal of 90^o is 16.2^o with a source latitude of 26.3^o. For an initial wave normal angle of -90^o, the ionospheric entry latitude is 15.9^o with a source latitude of 5.8^o. Signals from a source between 26.3^o and 5.8^o will therefore be able to reach the satellite and will have ionospheric entry latitudes that vary by only 0.3^o. The greatest variation in entry latitude occurred for a satellite at 30^o and a source in the opposite hemisphere. The ionospheric entry points, in this case, varied by 0.7^o. The closeness of the ionospheric entry points can be explained by the fact that the wave normal angle, on entering the ionosphere, is refracted very close to the vertical in all cases. Even though the initial wave normal angles vary from

-90^o to 90^o the maximum variation in refracted wave normal angles is from 3.9^o to -5.4^o.

As seen in figure 4.8, the ionospheric entry latitude for signals in the same hemisphere as the satellite, varied by at most 0.2^o for frequencies between 2 kHz and 10 kHz. This would that seem to indicate that fractional hop whistlers, originating in the same hemisphere as the satellite, can be observed with a continuous frequency range between 2 kHz and 10 kHz as long as their source position is within 10^o of the ionospheric entry point.

For signals originating in the hemisphere remote from the satellite the situation is slightly different. Figure 4.9 shows that the ionospheric entry latitudes may vary by as much as 3^o for signals between 2 kHz and 10 kHz. This means that there may be a 3^o latitude range for which certain frequencies can illuminate their ionospheric entry point while others can not. The whistler trace would then be missing those frequencies that are unable to illuminate their entry point. This is illustrated in figure 4.10 which shows 2 kHz, 6 kHz and 10 kHz signals starting at a latitude of -13.0^o. The left hand frame shows the entire ray path. To reach a satellite at 30^o the 2 kHz signal must have an initial wave normal of 87.1^o while the 6 kHz signal must have one of 90^o. The maximum possible initial wave normal for the 10 kHz signal is also 90^o and as a result the 10 kHz signal intersects the satellite altitude at 29.2^o and hence cannot reach the satellite at 30^o. This is illustrated in the right hand frame. In this case the higher frequencies on the whistler trace would be missing. If the source were at a latitude 10^o greater than the entry latitude then the lower frequencies would be missing. This could, however, also occur through lower hybrid reflection.

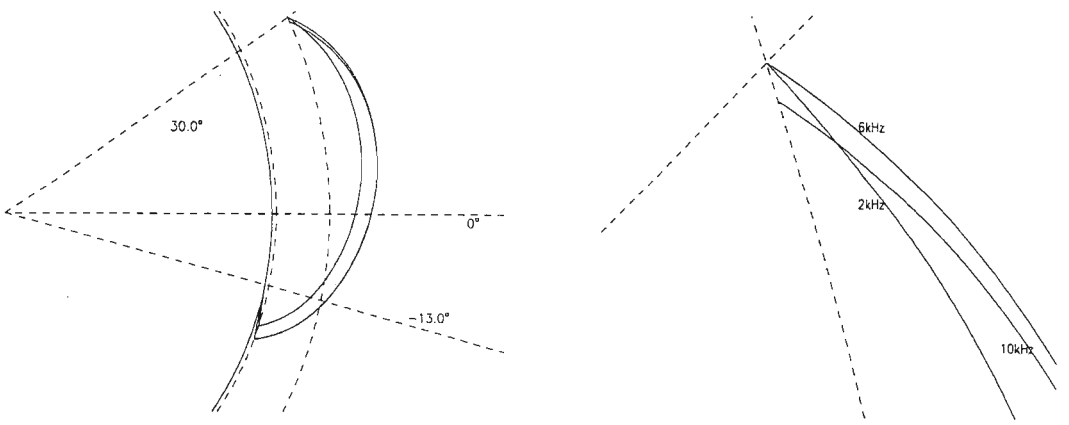

Figure 4.21 is a spectrogram showing fractional hop whistlers received on ISIS2 on 26 October 1976 at a geomagnetic latitude of 30^o. Whistlers with dispersions of about 5 $s^{\frac{1}{2}}$ and with dispersion of about 25 $s^{\frac{1}{2}}$ can be seen. The low dispersion

Figure 4.20: Ray paths for 2 kHz, 6 kHz and 10 kHz signals starting at a latitude of -13^o. The 2 kHz and 6 kHz signals are able to be received on a satellite at 30^o while the 10 kHz signal is not.

whistlers are interpreted as being from the same hemisphere as the satellite and those with the higher dispersions are from the opposite hemisphere. The whistlers from the near hemisphere all have a frequency range from 10 kHz down to a few hundred Hertz although frequencies between about 5 kHz and 2 kHz are weaker than the rest. the reason for this is not quite clear but it is thought that this could be due to propagation effects in the earth-ionosphere wave guide that occurred before the signal entered the ionosphere.

The whistlers from the opposite hemisphere have varying frequency ranges. One in the middle of the spectrogram has a frequency range from 10 kHz down to about 1 kHz while others in the spectrogram have maximum frequencies of between 4 kHz and 8 kHz. The higher dispersion whistler immediately to the left of the one with a frequency range from 10 kHz to 1 kHz actually looks stronger and yet has a maximum frequency of about 8 kHz. This is interpreted here as indicating that the whistlers that are missing the higher frequencies were generated by a lightning source that was unable to illuminate the higher frequency entry points. This would mean that the source position would be about 10^o equatorward of the ionospheric entry point.

If the above is correct then our ray tracing results show that fractional hop whistlers, generated in the opposite hemisphere, observed on a satellite at $30^o$with higher frequencies missing must have a source latitude between -14.1^o and -11.0^o. If the source latitude is greater than -14.1^o then all the frequencies between 10 kHz and 2 kHz would be able to reach their ionospheric entry points and if it is less than -11.0^o, none of the frequencies between 2 kHz and 10 kHz would be able to reach the satellite. Figure 4.21 shows fractional hop generated in the opposite hemisphere with varying frequency ranges and with one that has a continuous range from 10 kHz to 1 kHz. This would indicate that, if all the whistlers are from a common thunderstorm, the source position must be near a latitude of -14.1^o with some spherics at higher latitudes and others at lower.

4.11 Expected Electron Densities

The International Reference Ionosphere (IRI) model was used to determine the expected values for the ion and electron densities for the period of interest. To determine these densities using the IRI model, the average sunspot number is

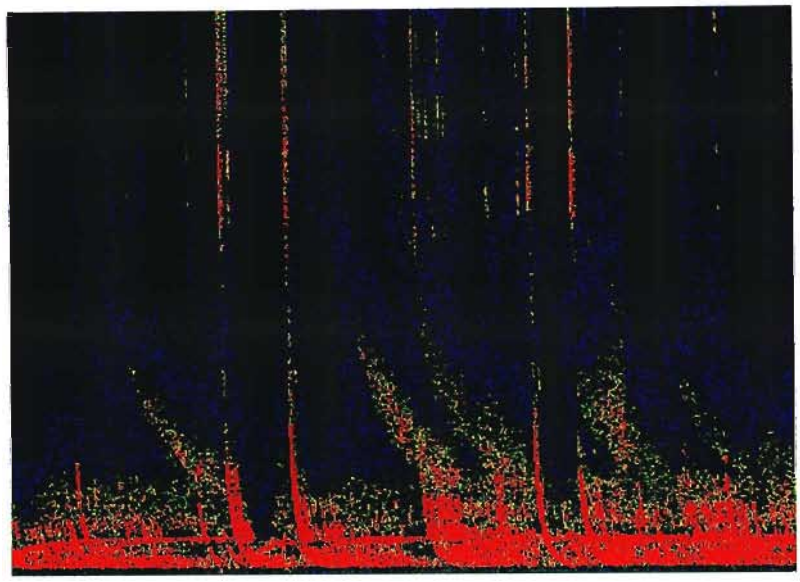

Figure 4.21: Spectrogram showing fractional hop whistlers from both hemispheres received on the ISIS2 satellite at a geomagnetic latitude of 30°. Frequency, on the y-axis, is from 0 - 5 kHz and time, on the x-axis, is 2.5 s.

required. For 1976 this was 12.6. This gives $F2$ densities of 6.7×10^5 cm^{-3} ($f_oF2 = 7.3$ MHz) at 20° and 9.0×10^5 cm^{-3} ($f_oF2 = 8.5$ MHz) at 0°. These values are somewhat higher than the f_oF2 values of 5.9 MHz at 20° and 7.3 MHz at 0° used in the ray tracing density models discussed above. Figures 4.22 and 4.23 show the electron densities given by the two models at geomagnetic latitudes of 20° and 0° respectively. As can be seen the values given by IRI are greater than those given by the models used for ray tracing at both latitudes and over the entire altitude range in both cases. When ray tracing using densities and density gradients that were more comparable to those given by IRI it was found that the dispersion was considerably greater than obtained from analysis of the ISIS2 data.

Fortunately ionosonde data was collected at Huancayo and Concepcion during October 1976. Huancayo and Concepcion are at geographic latitudes and longitudes of $12.02S$, $75.0W$ and $36.6S$, $73.0W$ respectively. These longitudes are close to the longitudes at which the satellite recorded the whistlers analysed in this study. The geomagnetic latitudes of these stations are $0.9S$ (Huancayo) and $22.4S$ (Concepcion). Figure 1 shows the dispersion of whistlers received on the ISIS2 satellite at a local time of about 07:30. At this local time, the f_oF2 values recorded at Huancayo and Concepcion respectively were 7.3 MHz and 5.2 MHz. The values of 7.3 MHz and 5.9 MHz used by our model are very close to those

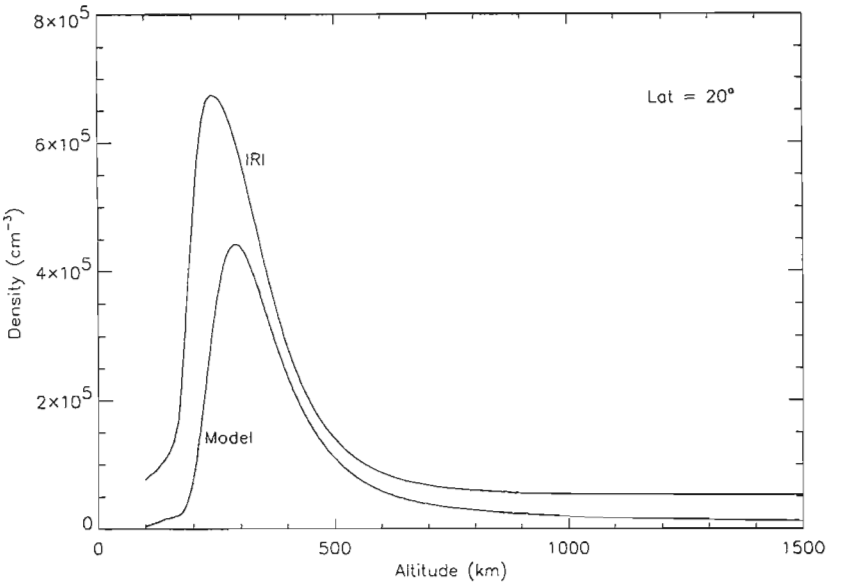

Figure 4.22: Comparison between IRI density values and those given by the model used for ray tracing at a geomagnetic latitude of 20°.

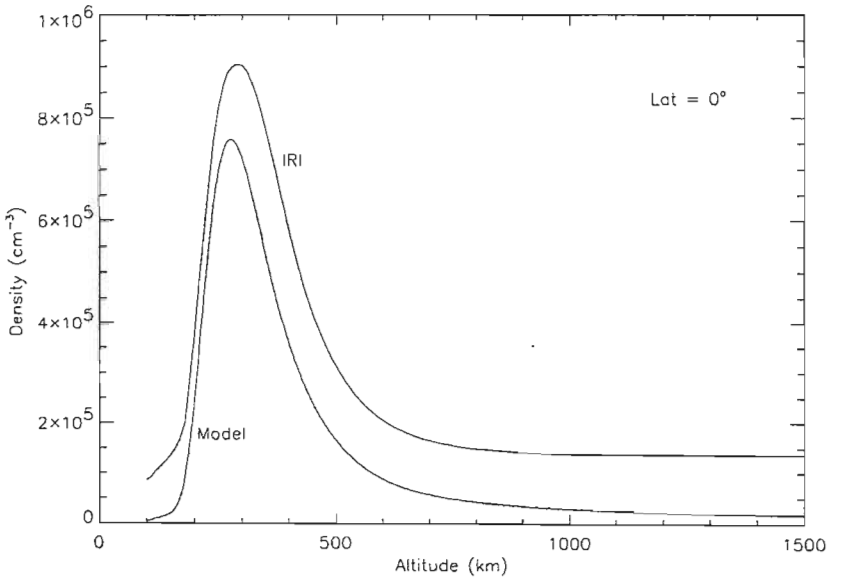

Figure 4.23: Comparison between the electron density given by IRI and that given by the models used in the ray tracing for a geomagnetic latitude of 0°.

recorded at Huancayo and Concepcion indicating that the values given by IRI may well be, for this period, 25% to 30% too high.

4.12 Conclusion

Dispersions obtained from analysis of fractional-hop whistlers received on the ISIS2 satellite during October 1976 while at geomagnetic latitudes less than 30^o are studied using ray-tracing. It is found that the observed dispersions can be explained by signals that propagate in an unducted mode and that the f_oF2 values needed to obtain the necessary dispersions are very similar to those determined from ionosonde recordings made at the same time and at similar latitudes and longitudes. It is also found that the change in dispersion with latitude can only be fully understood if latitudinal density gradients are introduced. The density model used can explain whistlers from both hemispheres and whistler echoes observed on the satellite.

The whistlers received on satellites are not necessarily confined to ducts of enhanced ionisation and hence as the satellite travels through the magnetosphere it can receive whistlers that have propagated through most parts of the magnetosphere which, using the above technique, can be used to determine, approximately, the variation of density with altitude and with latitude. The absence of lower frequency signals on whistlers echoes observed at magnetic latitudes of about 30^o is shown to be explained by Lower Hybrid Resonance reflection above the satellite.

Determining the position of the initiating atmospheric from low latitude whistler observations seems to be very inaccurate especially in the case where the source is in the same hemisphere as the satellite. When the source is in the opposite hemisphere, information about the source position can be obtained if certain frequencies are missing from the whistler trace although this gives a latitude range of about 4^o. It therefore seems that determining the source position from the fractional hop whistlers is very inaccurate at best.

Chapter 5

Wave-Particle Interactions

5.1 Introduction

Whistler mode waves propagating through the magnetosphere are, in some cases, able to resonate and exchange energy with energetic radiation belt electrons. These electrons are confined, on this time scale, to travel along the earth's magnetic field lines and hence it is often assumed that the resonance occurs with ducted whistlers. It has, however, been suggested (Inan and Bell [1991a], Friedel and Hughes [1990]) that unducted waves may undergo resonance with energetic electrons but this will not be considered in this study. A possible consequence of the resonance interaction is that electrons precipitate into the upper atmosphere. This precipitation causes secondary ionisation which can be observed as perturbations, known as Trimpi events, on sub-ionospheric VLF transmitter signals (Helliwell et al [1973], Lohrey and Kaiser [1979]).

During a campaign on Marion Island in May 1996 Trimpis and whistlers were almost simultaneously observed. To determine if the Trimpis were caused by whistler induced electron precipitation, the timing of the whistlers and Trimpis must be very accurately known and the precipitation times of the electrons must be calculated.

5.2 Dynamics of Energetic Charged Particles

A charged particle with charge q moving with a velocity $\overrightarrow{v}$ in a magnetic field, $\overrightarrow{B}$, experiences a force given by

$$\overrightarrow{F} = q\overrightarrow{v} \times \overrightarrow{B} \tag{5.1}$$

The form of equation (5.1) shows that the force is perpendicular to both $\overrightarrow{v}$ and $\overrightarrow{B}$. The particles will generally move in a spiral path along the magnetic field direction with electrons and protons gyrating in opposite directions. This is shown in figure 5.1.

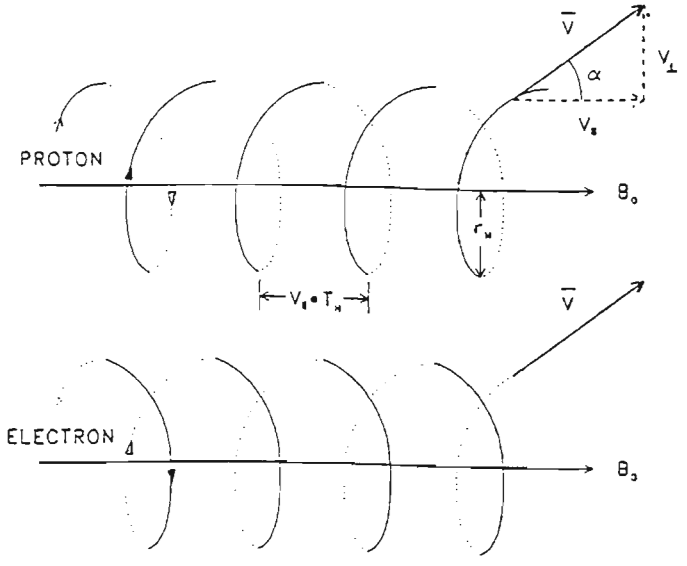

Figure 5.1: Particle motion in a magnetic field (taken from Friedel [1991]).

The only exceptions are when the velocity is purely parallel to $\overrightarrow{B}$, in which case the force is zero and the particle moves in a straight line, and when the velocity is purely perpendicular to $\overrightarrow{B}$, in which case the particle moves in a circle. The particle velocity can be divided into two components, one parallel to $\overrightarrow{B}$ ($v_{\|}$) and the other perpendicular to $\overrightarrow{B}$ ($v_{\perp}$). The angle between the velocity vector and the magnetic field direction is known as the pitch angle and is given by $\tan\alpha = \frac{v_{\perp}}{v_{\|}}$. Equation (5.1) can be rewritten, in scalar form, as $F = ev_{\perp}B = ev\sin\alpha B$. The centripetal force on a particle with mass m is $\frac{mv_{\perp}^2}{r_B} = \frac{mv^2\sin^2\alpha}{r_B}$ giving a gyroradius of

$$r_B = \frac{mv\sin\alpha}{Bq} \tag{5.2}$$

The period of a revolution is $\frac{2\pi r_B}{v\sin\alpha} = \frac{2\pi m}{Bq}$ giving an angular frequency of

$$\Omega_e = \frac{qB}{m} \tag{5.3}$$

known as the gyrofrequency.

If no work is done on the particle and if the magnetic field does not change significantly during one gyroradius then the magnetic flux through the particle's orbit is constant. This may be written as

$$\Phi_m = \pi r_B^2 B = \frac{2\pi m^2}{e^2} \frac{v^2 \sin^2 \alpha}{B} = const \tag{5.4}$$

From equation (5.4), using that energy is conserved, it can be seen that

$$\frac{\sin^2 \alpha}{B} = const \tag{5.5}$$

Equation (5.5) shows that the pitch angle of a particle in the earth's magnetic field, at a position where the field strength is B, depends its equatorial pitch angle (α_{eq}) and on the equatorial magnetic field strength (B_{eq}) in the following way

$$\frac{\sin^2 \alpha}{B} = \frac{\sin^2 \alpha_{eq}}{B_{eq}} = \frac{1}{B_m} \tag{5.6}$$

Since $B_{eq} < B$ the pitch angle always increase as the particle moves away from the equatorial plane and the particle will mirror, if the collision frequency is low, when the magnetic field strength is B_m. If B_m is at an altitude where the collision frequency is high the particle will collide with neutral atmospheric particles and will precipitate into the earth's atmosphere. The equatorial pitch angle above which all particles mirror and below which all particles precipitate is known as the *loss cone pitch angle* (α_{lc}). This can be represented (figure 5.2) as a cone about the magnetic field direction. Without outside influence the loss cone would contain no particles as they would have all precipitated.

If a centered dipole model is assumed for the earth's magnetic field, the equation of a field line, in polar co-ordinates, is given by equation (3.15). The geomagnetic latitude (θ_e) at which the field line intersects the earth's atmosphere can be found, assuming an atmospheric thickness of $100km$, by setting $r = r_e + 100km$ in equation (3.15) giving $\cos^2 \theta_e = \frac{r_e + 100km}{r_o}$. To find the mirror latitude (θ_m) of a particle with equatorial pitch angle α_{eq} equations (3.17) and (5.6) are combined, remembering that $\sin \alpha = 1$ at the mirror latitude, to give

$$\frac{\cos^6 \theta_m}{(4 - 3\cos^2 \theta_m)^{\frac{1}{2}}} = \sin^2 \alpha_{eq} \tag{5.7}$$

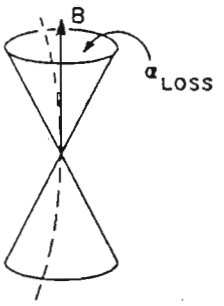

Figure 5.2: Diagram illustarting the loss cone (taken from Roederer [1970]).

Equation (5.7) must be solved numerically. It shows that for a given equatorial pitch angle the mirror latitude is independent of the field line. Using equations (3.15) and (3.16) with $r = r_e$ and $\theta_m = \theta_e$ gives

$$\sin^2 \alpha_{lc} \simeq \frac{1}{L^3 \left[4 - \frac{3}{L}\right]^{\frac{1}{2}}} \tag{5.8}$$

This equation is approximate because the precipitation would occur at an altitude of about 100 km and not at the earth's surface.

From equation (3.15), the length of a field line arc, ds, is

$$ds = (dr^2 + d\theta^2)^{\frac{1}{2}} = r_o \cos\theta \left(4 - 3\cos^2\theta\right)^{\frac{1}{2}} d\theta \tag{5.9}$$

The bounce period (time it takes for the particle to go from one mirror point to the other and back again) is $2\int_{\theta_m}^{-\theta_m} \frac{ds}{v_\parallel}$ which, using equations (5.6), (5.9), (3.17) and (5.7), can be shown to be given by (Roederer [1970])

$$\tau_B = \frac{4 r_e L}{v} f(\alpha_{eq}) \tag{5.10}$$

where $f(\alpha_{eq})$ is a function that depends on the equatorial pitch angle (α_{eq}) and on the mirror latitude (θ_m) and is given by

$$f(\alpha_{eq}) = \int_0^{\theta_m} \frac{\cos\theta \left(4 - 3\cos^2\theta\right)^{\frac{1}{2}}}{\left[1 - \frac{\sin^2 \alpha_{eq} (4 - 3\cos^2\theta)^{\frac{1}{2}}}{\cos^6 \theta}\right]} d\theta \tag{5.11}$$

Of most interest in this study is the interaction between whistler mode waves and energetic electrons, in which case $q = e$ and $m = m_e$.

5.3 Cyclotron Resonance Interaction

Whistler mode waves may, in certain circumstances, interact with and possibly exchange energy with charged particles in the earth's magnetosphere. Of particular interest is the cyclotron resonance interaction in which whistlers resonate with counterstreaming electrons. The electrons gyrate about the field line at the electron gyrofrequency (Ω_e), given by equation (5.3). The whistlers, travelling in the opposite direction in a duct of enhanced ionisation, are circularly polarised at a frequency lower than the electron gyrofrequency. Figure 5.3 (Hargreaves [1979]) shows the wave and electron motions about the geomagnetic field.

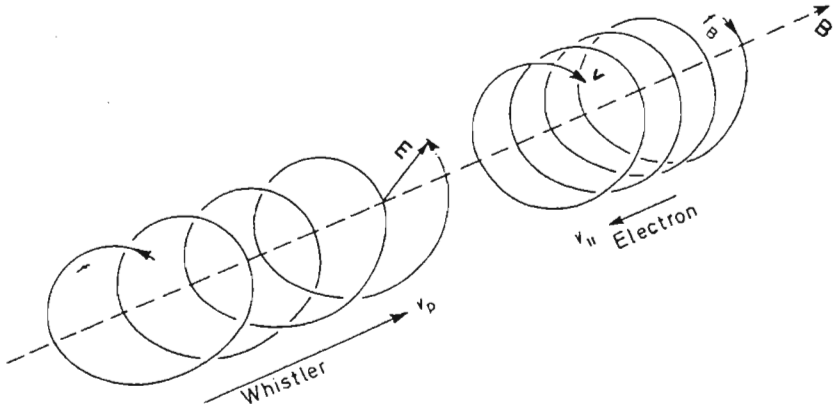

Figure 5.3: Wave and particle motions about the geomagnetic field.

For resonance, the wave frequency (ω) must be doppler shifted up to the electron gyrofrequency (Ω_e). This is expressed by

$$\omega - \overrightarrow{k} \cdot \overrightarrow{v} = \Omega_e \tag{5.12}$$

where $\overrightarrow{k}$ is the wave number and $\overrightarrow{v}$ is the particle velocity. $\overrightarrow{k}$ is given by $\frac{\omega\mu}{c}$ where μ is the phase refractive index given by equation (2.4). For longitudinal propagation, and considering only the R mode, this can be simplified and is given

by equation (4.1). From equation (5.12) it can be seen that the higher energy particles resonate with the lower wave frequencies. If the electron velocity is close to the speed of light then Ω_e must be divided by γ, the relativistic correction .

Since $\overrightarrow{k}$ and $\overrightarrow{B}$ are parallel, equation (5.12) shows that the resonance condition depends only on the electrons parallel velocity ($v_{\|}$). The electron's total velocity, and hence energy, can be determined if the pitch angle is known. During the interaction the electrons undergo pitch angle diffusion (Kennel and Petschek [1966]) with some electrons diffusing into the loss cone and precipitating into the upper atmosphere. The electrons diffuse along surfaces in velocity space defined by the resonance condition (Lyons and Williams [1984]). A decrease in the electron energy causes wave growth while an increase in electron energy causes wave damping. This depends on the form of the electron distribution function. A loss cone distribution, which is the most likely distribution in this case, results in cyclotron wave growth as the electrons diffuse into the loss cone (Lyons and Williams [1984]). The optimal region for the cyclotron resonance interaction is thought to be near the equatorial plane as this is where the magnetic field changes the slowest and hence the resonance condition is satisfied for the longest period. Liemohn [1967], however, showed that the optimum region may be a few degrees away from the equatorial plane due to enhanced pitch angle anisotropy.

5.4 The Trimpi Event

Trimpi events are amplitude and/or phase perturbations on sub-ionospheric VLF transmitter signals caused by interference between a direct signal, from the transmitter to the receiver, and one scattered from a patch of ionisation in the upper atmosphere (Dowden and Adams [1988]). The ionisation patch is thought to occur just below the D region, at an altitude of about 80 - 90 km, and probably has an horizontal extent of a few tens of kilometres. The transmitters are stable in both amplitude and phase and hence any variation must be caused by a modification of the earth ionosphere wave guide. Trimpis are characterised by a sudden change, referred to as the onset, in the amplitude and/or phase followed by a slower recovery to the original level. They are named after M.L.Trimpi who first observed them at Eights Station, Antarctica on a signal (NSS) from Annapolis, Maryland. Figure 5.4 shows an amplitude Trimpi observed on the 19.8kHz signal from Australia (NWC) received at Marion Island. It has an amplitude decrease of about 0.7dB followed by a 25 s to 30 s recovery. Each point is the mean signal strength in a 400 ms sample.

The duration of the Trimpi onset depends on the way in which the ionisation patch is created. Onset durations are very short (< 50 ms) if the ionisation

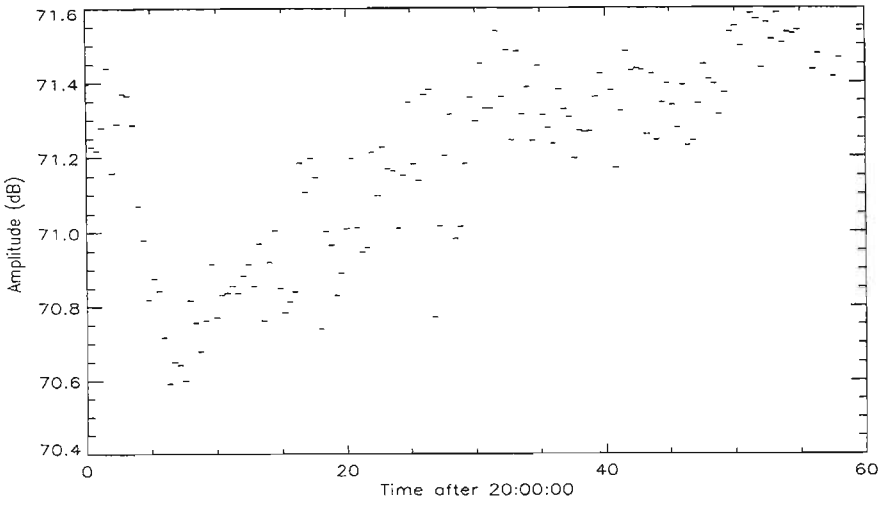

Figure 5.4: Amplitude Trimpi on NWC.

patch is the result of direct heating of the upper atmosphere by electromagnetic radiation (Inan et al [1991b]) or if it is the result of a cloud to ionosphere discharge (sprite) (Dowden et al [1996b]). Longer times (0.5 s−2 s), such as in figure 5.4, result if the ionisation patch is caused by the precipitation of energetic electrons into the upper atmosphere after a cyclotron resonance interaction with whistler mode waves (Helliwell et al [1973]). The onset duration is therefore thought to depend on the period during which ionisation takes place and hence, in the latter process, on the duration of the precipitation. The recovery time is related to the recombination rate which depends on the altitude of the ionisation patch. The lower the ionisation patch, the higher the collision frequency and the shorter the recovery time.

5.5 Omnipal Receiver

The omnipal is a PC based, narrowband VLF receiver that is used to record the amplitudes and phases of high power, land-based VLF transmitter signals. The system is able to receive one OMEGA signal (old land-based navigation system) and five MSK (Minimum Shift Keying) signals. The OMEGA signal was used largely for accurate timing. It consists of 5 frequencies transmitted in a pattern lasting exactly 10 seconds. When the OMEGA transmitters were first introduced, the start of each 10 second cycle occurred at exactly 0, 10, 20, 30, 40 and 50 seconds UTC (Co-ordinated Universal Time). UTC is kept to within

0.9 s of mean solar time by introducing or deleting exactly one second, known as a leap second, to UTC every 12 or 18 months. This "leap second" is not added to OMEGA time which means that after each "leap" second is added to UTC the start of the OMEGA 10 second cycle occurs exactly one second later than it did before the "leap second" was added. If the difference between OMEGA and UTC is known, and if the initial time is set to within a few seconds of UTC, the omnipal system is able to obtain the correct time using the OMEGA pulses. Being a PC based system the initial time is obtained from the PC clock which is set, to within 100 ms of UTC, using a Global Positioning System (GPS). With the introduction of GPS, the OMEGAs have become obsolete and were finally switched off at the end of September 1997.

The MSK transmissions are synthesised from 4 monochromatic sine waves, only one of which is transmitted at any time. Two of these are at the same frequency and are 180° out of phase and the other two are, if the baud rate is 200 baud, at a frequency 100 Hz lower or higher and are also 180° out of phase. For example, the signal from Australia (NWC) has an upper frequency of 19.85 kHz and a lower frequency of 19.75 kHz. We will generally refer to the signals by their centre frequency which, in the case of NWC, would be 19.8 kHz. The reason for having two phases per frequency is that the frequency can be changed every 5 ms (giving a baud rate of 200 baud) with continuity in phase and near continuity in slope. Figure 5.5, taken from Thomson [1981], illustrates the above. The four upper curves represent the four possible sine waves and the fifth curve represents a possible transmission. The diagram shows a time between frequency changes of 10 ms which is because it was originally drawn to represent a 100 baud signal. It is, however, exactly analagous for a 200 baud signal.

There are number of MSK transmitters. This study will consider signals received by an omnipal run during a campaign on Marion Island ($46°53'S$, $37°52'E$, $L = 2.63$) in May 1996. During this campaign the OMEGA signal was from Reunion. Only four MSK stations were strong enough to by received by the omnipal system and they are listed below together with their centre frequencies and their locations.

Station	Freq (kHz)	Latitude	Longitude
NWC	19.8	$24°48'S$	$114°09'E$
NAA	24.0	$44°39'N$	$67°17'W$
FRA	18.3	$46°42'N$	$1°15'E$
GBR	16.005	$52°22'N$	$1°11'W$

Figure 5.6 shows the transmitter-receiver great circle (TRGCP) paths for the above MSK stations and for OMEGA Reunion (REU) received at Marion Island. All are labelled except for GBR and FRA which come from Great Britain and France respectively.

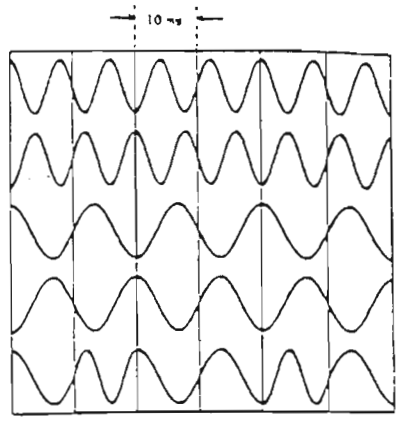

Figure 5.5: MSK signal synthesis.

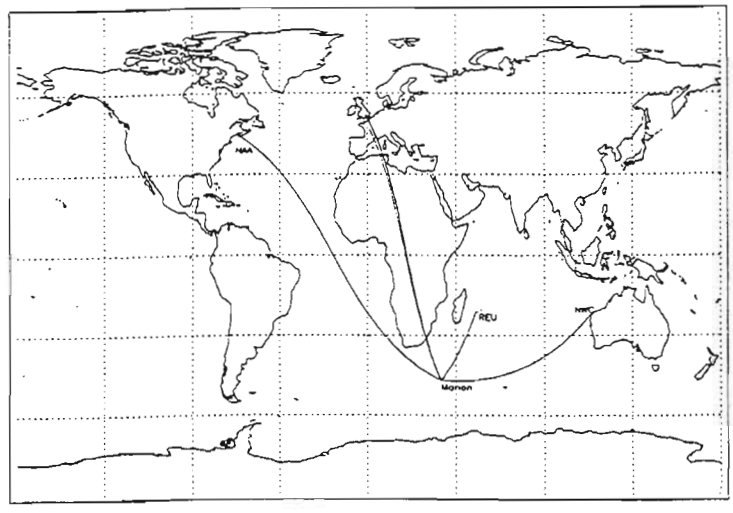

Figure 5.6: Great circle paths to Marion Island for the four MSK signals and OMEGA Reunion.

5.6 Summary

Using an omnipal receiver, the amplitudes and phases of sub-ionospheric VLF transmitter signals can be monitored. Amplitude and/or phase perturbation, known as Trimpi events, can indicate ionisation of the upper atmosphere. The duration of the Trimpi onset gives an idea of how the ionisation patch was formed. Of particular interest is ionisation caused by the precipitation of energetic electrons after a cyclotron resonance interaction with whistler mode waves. In this case the Trimpi onset should be 0.5 s -2 s long. The recovery time of the Trimpi gives an idea of the height of the ionisation patch.

Chapter 6

Whistler-Trimpi Correlations

6.1 Introduction

During a campaign on Marion Island in May 1996, an omnipal receiver was used to record the amplitudes and phases of OMEGA Reunion and 4 MSK stations (NAA, NWC, FRA and GBR). Another VLF receiver recorded broadband VLF data (0 – 20 kHz) with a 40 dB dynamic range. The initial omnipal time was obtained from a GPS system and was maintained using the OMEGA pulses. The time on the broadband VLF system was corrected using the OMEGA pulses. A Doppler receiver (Thomson [1981]) was also run by Dr M. Clilverd, British Antarctic Survey, and will be discussed in more detail later in this chapter. On the 11 May between 1740 UT and 2010 UT (2010 – 2240 Local Time) a total of 11 Trimpis were observed on NWC (19.8 kHz transmitter signal from Australia). During the same period, the signals from FRA (18.3 kHz signal from France) and GBR (16.0 kHz signal from Great Britain) were also strong and had good signal to noise ratios but showed no signs of Trimpis.

At the same time as each of the 11 Trimpis, whistlers were recorded on the broadband VLF system. During this period whistlers were received at the rate of about 10 per minute. In all 11 cases in which whistlers and Trimpis were simultaneously observed, the whistlers were considerably stronger than the average strength of whistlers during the period. This apparent amplification of the waves, together with the association of the whistlers with Trimpis, confirms the idea, discussed in the previous chapter, that during a cyclotron resonance interaction, between the whistlers and energetic electrons, electrons diffuse into the loss cone (Kennel and Petschek [1966]) and precipitate into the upper atmosphere. The precipitation causes secondary ionisation which scatters sub-ionospheric VLF transmitter signals (Dowden and Adams [1988]) causing the observed Trimpi.

Figure 6.1 shows a spectrogram (0 kHz −10 kHz) together with a plot of the phase of NWC. In both cases time is on the x-axis and runs from 19:37:10 to 19:37:50. Two whistlers, one at 19:37:19 and the other at 19:37:39, can be seen on the spectrogram and Trimpis can be seen on the phase of NWC at the same time.

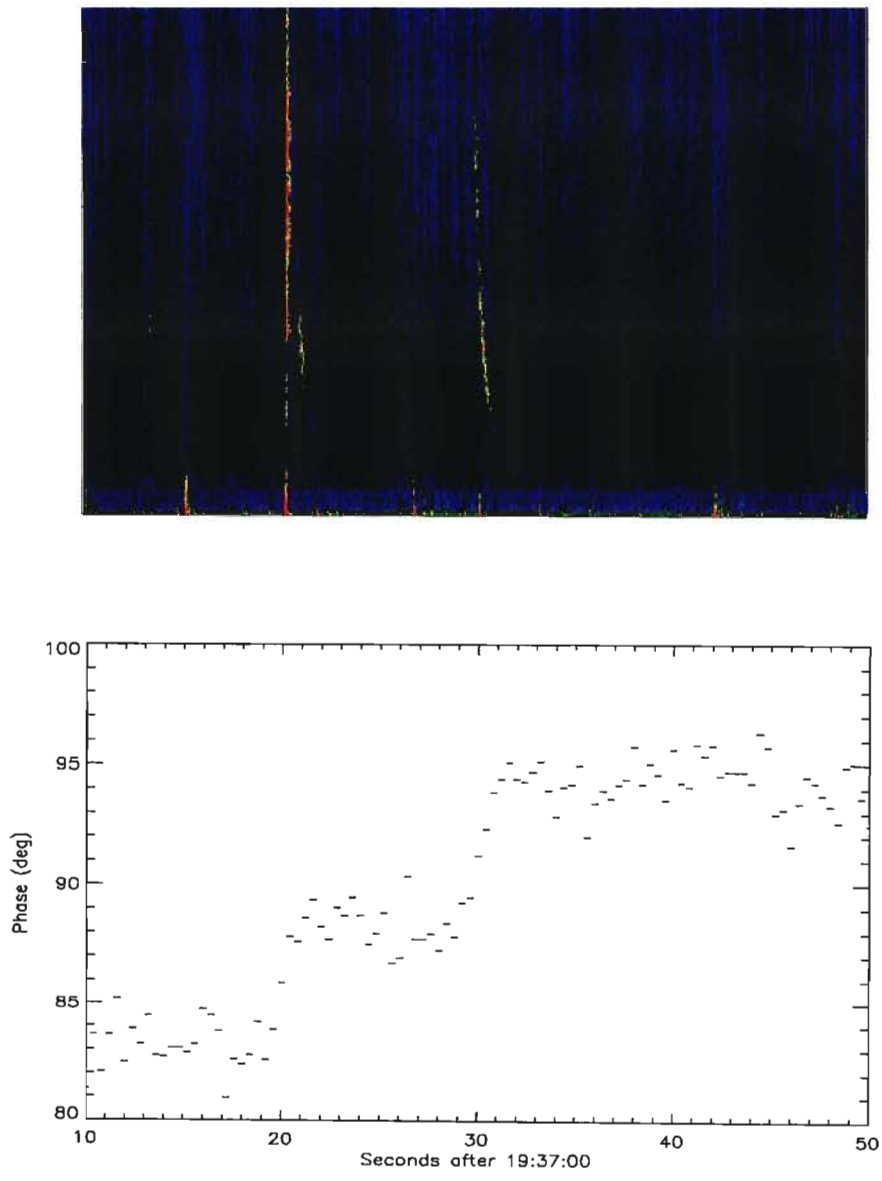

Figure 6.1: Whistlers and associated Trimpis. The upper frame shows a spectrogram (frequency scale of 0 - 10 kHz and a time of 40 s) with two whistler groups. The lower frame shows the phase of NWC with Trimpis at the same time as the whistlers in the spectrogram.

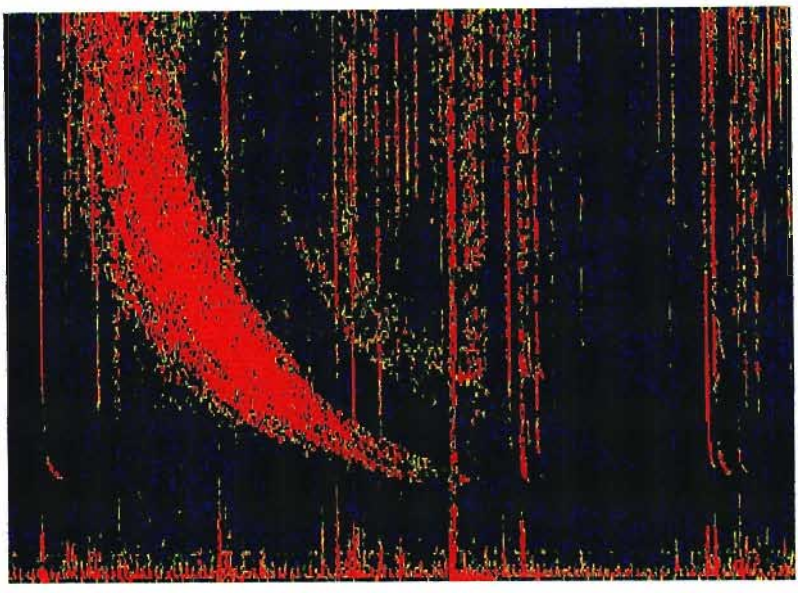

Figure 6.2: Trimpi associated whistler recorded at 20:07:08 at Marion Island. The frequency scale, on the y-axis, is 0 - 10 kHz and the time, on the x-axis, is 2.5 s.

6.2 Whistler Analysis

It is generally accepted that whistlers observed on the ground have travelled through ducts of enhanced ionisation (Smith [1961], Helliwell [1965]). Bernard [1973] developed a technique for determining the nose frequency (f_n), the nose travel time (t_n) and the L-value along which the whistler has travelled given the travel times at two other frequencies. This, however, necessitated identifying the time of the initiating atmospheric (T_z). Ho and Bernard [1973] further developed this technique for the case where the time of the initiating atmospheric is not known. Using an arbitrary time origin the technique uses three frequency-time ($f - t$) points on the whistler trace to determine the nose frequency, the nose travel time and the L-value. If a density model, normally Park's [1972] DE-1 model, is assumed then the equatorial electron density (n_{eq}) and the electron tube content (N_T) can also be determined. This technique was used to analyse the Trimpi associated whistlers observed on Marion Island.

Figure 6.2 shows a Trimpi associated whistler group received, on Marion Island, at 20:07:08 on the 11 May 1996. Other whistlers visible in the spectrogram are considerably weaker than the Trimpi associated whistler.

Due to the strength of the whistlers, the recordings were, in some cases, saturated making it difficult to distinguish individual traces within the whistler groups.

Determining the $f-t$ points for use with the Ho and Bernard's 3 point technique was, therefore, also difficult. As a result of this, the most clearly defined traces, in all eleven groups, were used to determine an upper and lower bound for the L-values and equatorial electron densities. This gave L-values of between 2.68 and 3.05 with an error of $\pm 2\%$. There was some evidence of propagation at slightly lower L-values, but these signals were very weak and hence were assumed not to have been involved in a wave-particle interaction. The equatorial electron density (n_{eq}) varied from $1680 \pm 80\,\mathrm{cm}^{-3}$ at $L = 2.68$ to $1300 \pm 65\,\mathrm{cm}^{-3}$ at $L = 3.05$. The time of the initiating atmospheric was such that the wave travel time, on $L = 2.68$, varied from 913 ms at 10 kHz to 1738 ms at 2 kHz.

With the above information and using the theory discussed in the previous chapter the energies of the resonant particles and their bounce periods were determined. The precipitation times were then be calculated and were compared with the start times of the observed Trimpis.

6.3 Resonant Energies and Bounce Periods

It is assumed that the wave-particle interaction took place at the equatorial plane. The background electron density is then the equatorial electron density determined from the whistler analysis and the magnetic field strength (B) can be determined from the L-value by assuming a dipole magnetic field model. B is used in equation (5.3) to determine the electron gyrofrequency. The phase refractive index for a wave frequency ω is calculated using equation (4.1) once the electron plasma frequency has been determined using n_{eq}. The wave number, $\overrightarrow{k}$, can now be determined and is used in equation (5.12) to determine the velocity of a particle resonant with a wave of frequency ω. This is repeated for all the wave frequencies (2 kHz$-$10 kHz) and for the different L-values ($2.68 - 3.05$).

The electron's total energy depends on its pitch angle. Since the particles under consideration are those that precipitate, the pitch angle must be less than the loss cone pitch angle given by equation (5.8). Using a dipole magnetic field model, the pitch angle on $L = 2.68$ is 10.2^{o} and on $L = 3.05$ is 8.2^{o}. The duration of the cyclotron resonance interaction is determined by the particle and wave velocities and by the width of the wave pulse and is consequently very short. The pitch angle used in this study has, therefore, been taken to be the loss cone pitch angle since the electrons would probably only diffuse by a few degrees (from just outside the loss cone to just inside the loss cone) during the interaction. It is possible for the whistler to phase bunch the electrons (Helliwell [1967]) which may continue resonating and can generate waves, known as triggered emissions (figure 1.2), that can be received on the ground. If this were to happen the electrons may diffuse

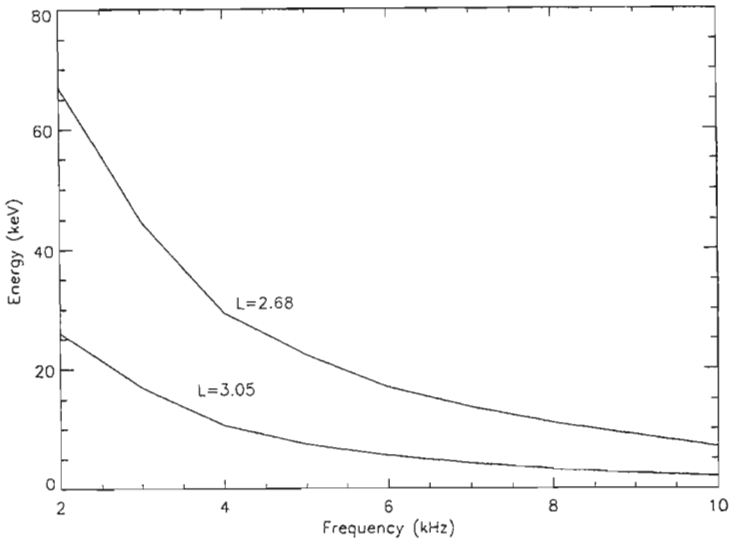

Figure 6.3: Resonant electron energies on L = 2.68 and L = 3.05

further into the loss cone. Triggered emissions were, however, not observed in this case.

Figure 6.3 shows the resonant energies for wave frequencies between $2kHz$ and $10kHz$ on $L = 2.68$ and $L = 3.05$. On $L = 2.68$ the energy goes from 68 keV to 7 keV and on $L = 3.05$ it goes from 26 keV to 2 keV.

Of particular interest is the precipitation times of the resonant electrons. Equations (5.10) and (5.11) are used to determine the bounce period of an electron on a field line with L-value L, equatorial pitch angle α_{eq} and mirror latitude θ_m (determined from α_{eq}). If an electron has an equatorial pitch angle less than the loss cone pitch angle ($\alpha_{eq} < \alpha_{lc}$) it will not mirror but will collide with atmospheric particles and precipitate. The precipitation time is then one quarter of the effective bounce period (the period it would have if it were to mirror at the latitude, θ_e, where the field line intersects the earth's atmosphere). The effective bounce period is given by equation (5.10) and equation (5.11) with $\alpha_{eq} \leq \alpha_{lc}$ and $\theta_m = \theta_e$. Figure 6.4 shows the bounce periods of electrons resonant with waves of frequencies between 2 kHz and 10 kHz on $L = 2.68$ and $L = 3.05$ and with equatorial pitch angle equal to the loss cone pitch angle. Since it has been assumed that the electrons only diffuse by a few degrees this will be very close to the effective bounce period of the electrons that precipitate.

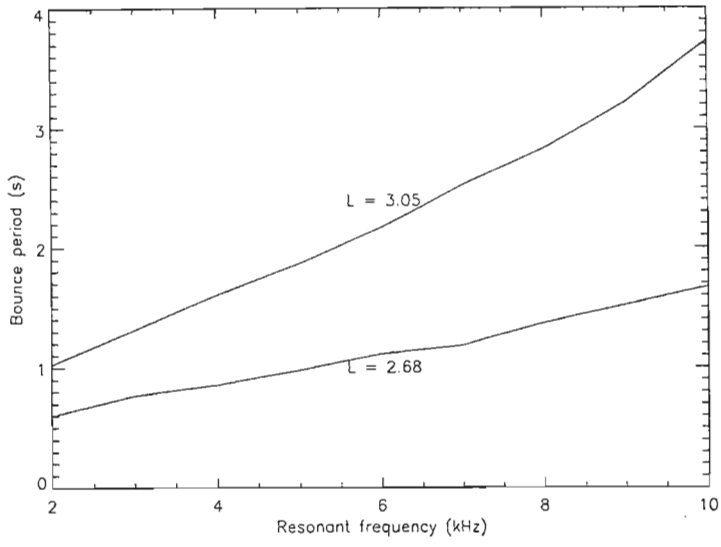

Figure 6.4: Bounce periods for particles resonant with wave frequencies between $2kHz$ and $10kHz$ on $L = 2.68$ and $L = 3.05$. The equatorial pitch angle is equal to the loss cone pitch angle.

6.4 Correlation with Trimpis

The apparent amplification of the Trimpi associated whistler groups observed on Marion Island indicates that the cyclotron resonance interaction probably took place before the whistlers were received and hence took place while the whistlers were travelling south. As shown by equation (5.12) the electrons and the waves must travel in opposite directions. The electrons must, therefore, have been travelling north. To have caused the Trimpi observed on Marion Island, the electrons must have mirrored in the north before precipitating in the south. This can be explained by the difference between the conjugate magnetic field strengths near the geomagnetic longitude of Marion Island. From the International Geomagnetic Reference Field (IGRF) magnetic field model, the magnetic field strength at an altitude of 100 km near Marion Island is 3.1×10^{-5} T and in the conjugate region, at the same altitude, it is 4.7×10^{-5} T. Using equation (5.6) it can be shown that for a given equatorial pitch angle, the mirror height in the north is greater the in the south. Electrons that mirror in the north may then precipitate in the south. The loss cone pitch angle for electrons travelling north near the geomagnetic longitude of Marion Island is 10.3^o and for electron travelling south it is 12.8^o. Thus electrons with equatorial pitch angles between 10.3^o and 12.8^o will mirror in the north and precipitate in the south near Marion Island.

The time between the interaction and the precipitation of electrons resonant with a wave frequency ω will then be $\frac{3}{4}\tau_B(\omega)$. The actual precipitation time depends on the interaction time. Whistler mode waves are dispersed and hence, if we assume that the interaction took place in the equatorial plane, the interaction time will differ for different frequencies. Relative to the atmospheric discharge that initiated the whistlers, the precipitation time is $\frac{1}{2}\tau_W(\omega) + \frac{3}{4}\tau_B(\omega)$ where $\tau_W(\omega)$ is the total travel time for a wave frequency ω. The whistler analysis determines the time of the initiating atmospheric and hence the actual precipitation time can be calculated.

Figure 6.5 shows four of the observed Trimpis (two amplitude Trimpis and two phase Trimpis) together with the arrival times of the whistlers and the calculated arrival times of the energetic electrons. The Trimpis can be identified by the sudden change in the amplitude or phase. The time scale is only $10s$ and is too short to see the recovery. The curves labelled **A** and **B** are the arrival times of the leading and trailing edges of the whistler groups. The curves labelled **C** and **D** are the arrivals times of the electrons resonant with the leading and trailing edges respectively. The electron arrival times are plotted against the resonant wave frequency and their energies can be determined from figure 6.3. The time of the initiating atmospheric is also given on each plot.

As figure 6.5 shows, the calculated precipitation times compare well with the Trimpi onset times. The Trimpi seems to start at about the same time as the precipitation of electrons resonant with the lower frequencies (2 kHz to 4 kHz) on $L = 2.68$. Figure 6.3 shows that this corresponds to particle energies of 40 keV -70 keV. The Trimpi onset seems to end at about the same time as the precipitation of electrons resonant with frequencies of between 5 kHz and 7 kHz on $L = 3.05$. This corresponds to energies between 15 keV and 2 keV. If the Trimpi onset corresponds to the ionisation of the upper atmosphere and the recovery to the recombination, the above would seem to indicate that energies of about 15 keV can cause secondary ionisation. This is lower than the 30 keV$-$40 keV predicted by Helliwell et al [1973] and Dowden and Adams [1988]. Determining exactly when the onset begins and ends is not possible since each data point is a 400 ms average of 5 ms samples giving, at best, an accuracy of $\pm$200 ms. It is also possible for the Trimpi to start during the previous sample but with the changes hidden in the noise. The Trimpis shown in figure 6.5 have noise levels of, at best, $\pm$0.2 dB and $\pm 1^o$ making this a possibility..

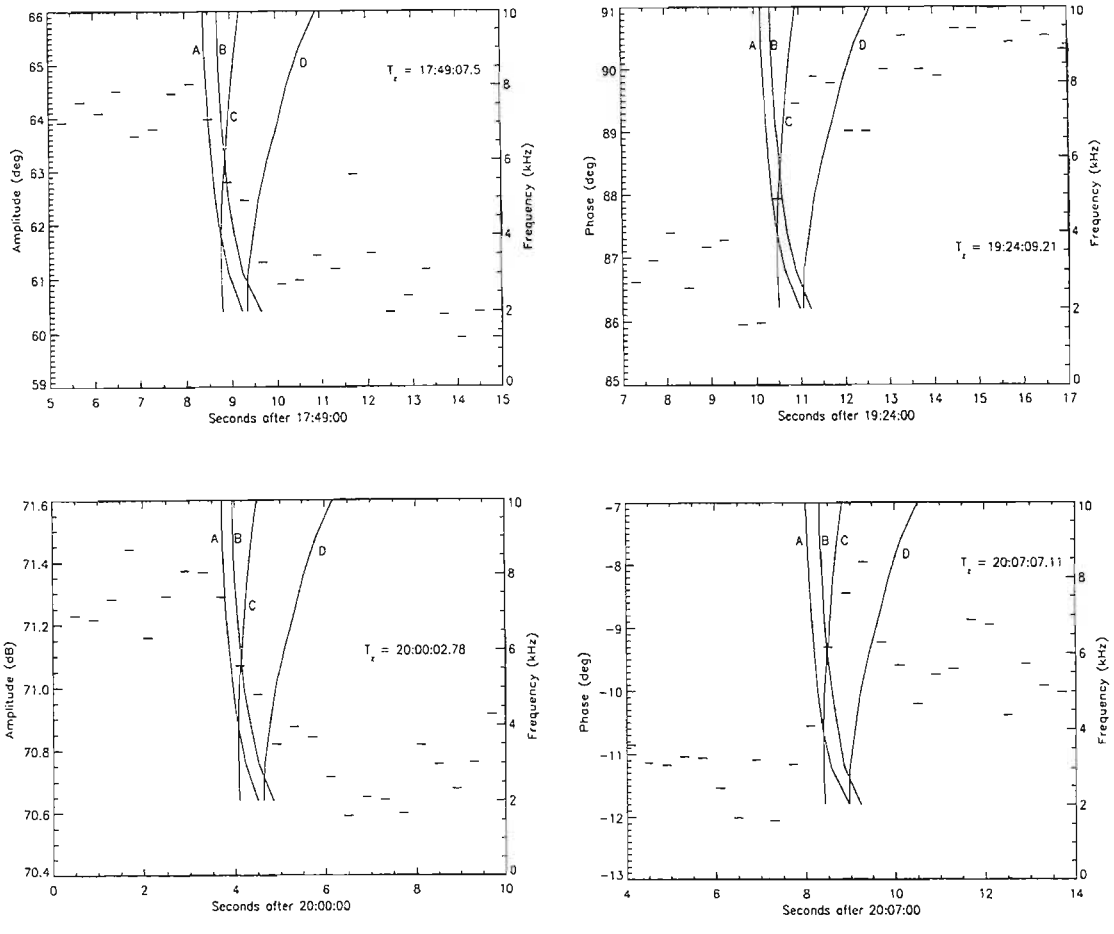

Figure 6.5: Trimpis together with whistler and particle arrival times

6.5 Precipitation Region

The magnetic field antenna used by the broadband VLF receiver consisted of two vertical, rhombic shaped loops, one aligned true North-South and the other true East-West. It should have been possible to determine the direction of arrival of the recorded whistlers by comparing the signals from the two loops. An estimate of the duct exit region could then be made by using the arrival bearing of the signal and the whistler L-shell. Unfortunately one of the pre-amplifier channels was faulty below 10 kHz during the period of interest and hence the bearings obtained were very inaccurate. It was however possible to get an idea of the bearings from the whistler-mode signals obtained from the VLF Doppler receiver (Thomson [1981]). The down going waves exit the duct before reaching the lower boundary of the ionosphere (Bernhardt [1977] and Strangeways [1981]). The

electrons on the other hand follow the field line to altitudes of typically 70 km -100 km. Their exit region is found by determining the point at which the field line, along which the whistlers travelled, intersects the lower boundary of the D-region.

Some or all of the whistlers in the group may produce ionisation patches giving complexity to the Trimpi structure.

6.5.1 Doppler Receiver

The VLF transmitter signals, received by the omnipal receiver, propagate directly from the transmitter to the receiver in the earth-ionosphere wave guide. Some of the signal energy, however, may enter the ionosphere and will propagate in the whistler mode. If these signals are trapped by ducts of enhanced ionisation they may propagate inter-hemispherically to be received on the ground by VLF receivers close to the conjugate region. The VLF Doppler receiver is used to determine the time delay between the direct sub-ionospheric signal and the whistler mode signal. The time delay is found by removing the direct sub-ionospheric signal from the received signal and cross-correlating this with what remains. Due to the low signal to noise ratio of the residual signal it takes 15 minutes to accumulate the correlation coefficients and obtain a significant result. Knowing the delay between the direct signal and the whistler mode signal allows one to determine the exact travel time of the whistler mode signal. Figure 6.6 shows the travel time of the whistler mode signal from GBR. Travel time is on the y-axis and has a range of 0 s$-$2 s. Time of day is on the x-axis and runs from 21:45 UT to 07:00 UT. Whistler mode was observed between 21:45 UT and 02:00 UT. The discrete features of the observed whistler mode signals indicates that a number of ducts were present. At 21:45 UT the travel time varied from 760 ms to 920 ms decreasing to between 840 ms and 760 ms at 02:00 UT.

If whistler mode signals are received from two VLF transmitters then the exact travel times of both frequencies can be determined. These travel times would be identical to the travel times of the same frequencies on a whistler (generated by a natural atmospheric discharge) that has travelled through the same ducts. Bernard's [1973] two point method can therefore be used to determine the effective nose frequency, the travel time of the effective nose frequency and the L-value of the duct through which the signals travelled. The 'effective nose frequency' is the nose frequency that the theoretical natural whistler would have.

The VLF Doppler receiver used the same antenna as used by the broadband VLF receiver. Fortunately the faulty channel on the pre-amplifier worked quite well at the VLF transmitter frequencies (> 15 kHz) which are somewhat higher than

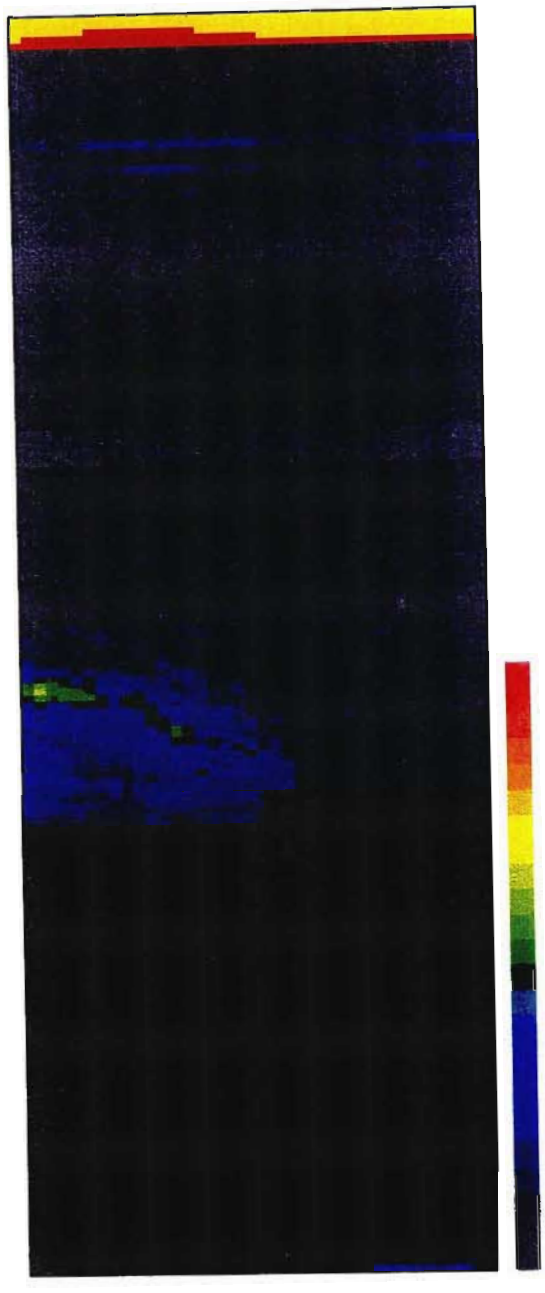

Figure 6.6: Doppler results showing the whistler mode travel time for signals from GBR. Travel times, on the y-axis, are from 0s - 2s and time of day, on the x-axis is from 21:45UT to 07:00UT.

the frequencies of the whistlers received by the broadband system. The Doppler system could also be calibrated using the known bearings of the sub-ionospheric transmitter signals. It also used the E-field antenna, used by the omnipal receiver, to remove the 180° ambiguity that would be obtained if only the loop antennas were used to determine the bearings.

6.5.2 Doppler Results

The first whistler-mode signals detected by the Doppler system began at 21:45 UT on the 11 May. This is just less than 2 hours after the last Trimpi was observed. Whistler mode signals were received from FRA and GBR. The results showed that there were five ducts at 22UT with L-values ranging from $L = 2.65$ to $L = 2.94$. The only accurate bearing was obtained from the strongest duct which had an L-value of $L = 2.86$ and a bearing of 300°. These ducts drifted equatorward to give L-values of between $L = 2.59$ and $L = 2.88$ at 00UT. The strongest duct at 00UT was at $L = 2.80$ and had a bearing of 330°. Saxton and Smith [1989] suggest that during geomagnetically quiet times and at these local times (~00 UT), the drift should be constant. This gives possible L-values of between $L = 2.76$ and $L = 3.05$ at 19UT. The strongest at 19UT should have been at $L = 2.94$ with a bearing of about 220°. These L-values are consistent with the values of between $L = 2.68$ and $L = 3.05$ obtained by analysis of the Trimpi associated whistlers. The Trimpi associated whistlers also showed the presence of a number of ducts (figure 6.2) although it wasn't possible to determine exactly the number of ducts.

If it is assumed that the whistlers exit the ducts at an altitude of 500 km (Bernhardt [1977] and Strangeways [1981]) and travel vertically down through the ionosphere to the waveguide, the ducted signal with $L = 2.94$ at 19UT would exit the ionosphere about 290 km west of Marion Island at a position approximately $48.98S$, $35.13E$. Since it was only possible to get an accurate bearing on the strongest duct an assumption about the position of the other ducts must be made. It was assumed that all the ducts lie on the same geomagnetic longitude. The ducts at $L = 2.68$ and $L = 3.05$ would then exit at $46.2S$, $33.1E$ and $49.9S$, $35.9E$ respectively. The precipitation regions are found by determining the position at which the field lines, along which the waves have travelled, intersect the earth's atmosphere. This gives precipitation regions of $47.7S$, $34.7E$ and $51.3S$, $37.8E$ for $L = 2.68$ and $L = 3.05$ respectively.

Figure 6.7 shows the transmitter signal paths to Marion Island together with the location of the calculated precipitation region (short line south-west of Marion Island). Madagascar and the eastern coast of South Africa can also be seen in the figure. The longitudinal width of the precipitation region is not known. It is clear

that the Trimpis on NWC must have been caused by interference between the direct signal and one scattered back to the receiver. Dowden et al [1996c] have shown that Trimpis can be caused by signals back scattered from sprite plasma. The lack of Trimpis on GBR and FRA would seem to indicate that the side lobes of the signal re-radiated by the ionisation must be very small. Dowden and Adams [1988] showed how the radiation pattern from a stalactite like ionisation patch contains no side lobes. The ionisation patch, in this case, could consist of a number of such stalactites, each one formed by precipitation from different ducts. This may explain why Trimpis were not observed on GBR and FRA even though their signals were strong and had good signal to noise ratios. Trimpis were probably not observed on NAA as it was weak and had a bad signal to noise ratio. If, instead of being aligned geomagnetically, the ducts were aligned along geographic lines of longitude, the interpretation would be the same.

Dowden and Adams [1988] showed that if the position of the ionisation patch is known to within a fraction of a wavelength, the Trimpi amplitude and phase perturbations could be explained by phasor addition of a direct signal and one scattered from the ionisation patch. This is not possible in this case as the error in the position of the ionisation patch is at least one wavelength. Dowden and Adams [1993] also showed that the position of the ionisation patch could also be determined if Trimpis were observed at a number of different sites. As only a single receiver was used in the Marion Island campaign, this was also not possible.

Tolstoy [1986] showed how the amplitude change on signals received at Palmer station varies with distance between the receiver and the ionisation patch. His results seemed to show that the effect is very small when the ionisation patch is very close to the receiver. The results from the VLF Doppler receiver show the ducts moving closer to and possibly directly over the receiver and may explain why no Trimpis were observed after 2007UT.

6.6 Summary and Conclusion

It has been shown, from the times of arrival of whistlers and their associated Trimpis, that the Trimpis are caused by scattering from ionisation patches formed by whistler induced electron precipitation. The apparent amplification of the observed whistler also confirm that a cyclotron resonance interaction has taken place and that the electrons must have mirrored in the northern hemisphere before precipitating near Marion Island. The energies of the precipitating electrons varied from 70 keV down to about 2 keV. Previous work (Helliwell et al [1973]) has suggested that Trimpi producing electron needs energies of 30 keV and greater.

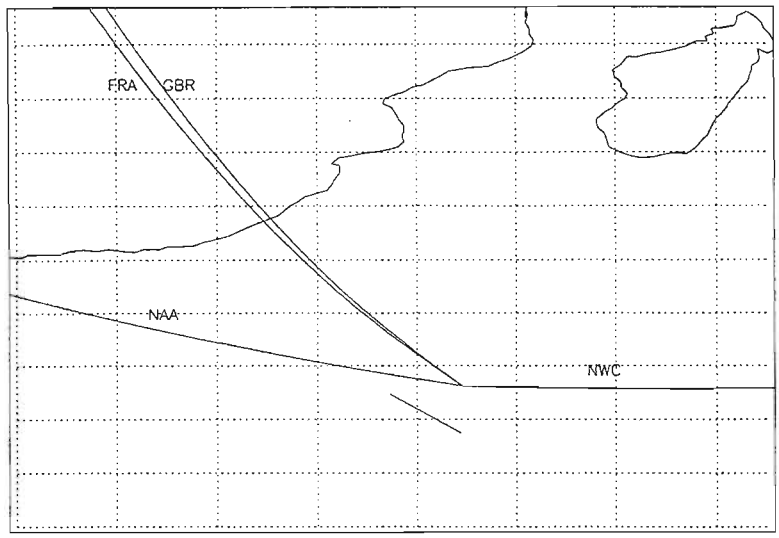

Figure 6.7: Map showing the transmitter paths to Marion Island together with the precipitation region. Madagascar and the eastern coast of South Africa can be seen.

Results obtained here suggest that energies as low as 5 keV may be able to sustain the ionisation patch.

Bearings obtained from whistler mode signals received by the VLF Doppler allow an approximate precipitation region to be determined. The Trimpis observed on NWC would have to be caused by a signal backscattered to the receiver. The lack of Trimpis on GBR and FRA can be understood if the radiation pattern of the scattered signal contains little or no side lobes.

Chapter 7

Whistler Ghosts

7.1 Introduction

During analysis of the Trimpi associated whistlers, discussed in the previous chapter, it was noticed that each whistler group was followed, after a time of between 500 ms −700 ms, by a second, fainter whistler group the components of which appear to correspond to those of the preceding group. We have called these whistler 'ghosts' from their appearance on the spectrograms. Figure 7.1 shows spectrograms of all eleven whistler groups and their 'ghosts'. Each spectrogram is 2.5 s long and has a frequency range of 0 kHz−10 kHz. The 'ghost' phenomenon can be clearly seen in frames 1, 3, 9, 10 and 11 but closer inspection reveals their presence in all eleven frames. Frames 4 and 5 contain additional whistler groups that are not involved in the 'ghost' phenomenon. The horizontal lines in frame 10 are calibration tones generated by the receiving equipment. At first glance it seems as though the initial whistler group and the 'ghost' group have the same dispersion. The two whistler groups also seem to have similar structure which could indicate that they have propagated through the same ducts. If this is indeed the case then the 'ghost' group would have to have been generated by an atmospheric discharge that occurred 500 ms−700 ms after the discharge that generated the initial whistler group.

7.2 'Ghost' Analysis

It wasn't possible to analyse the 'ghost' groups using the Ho and Bernard [1973] method as they were either too weak or the individual traces within the group

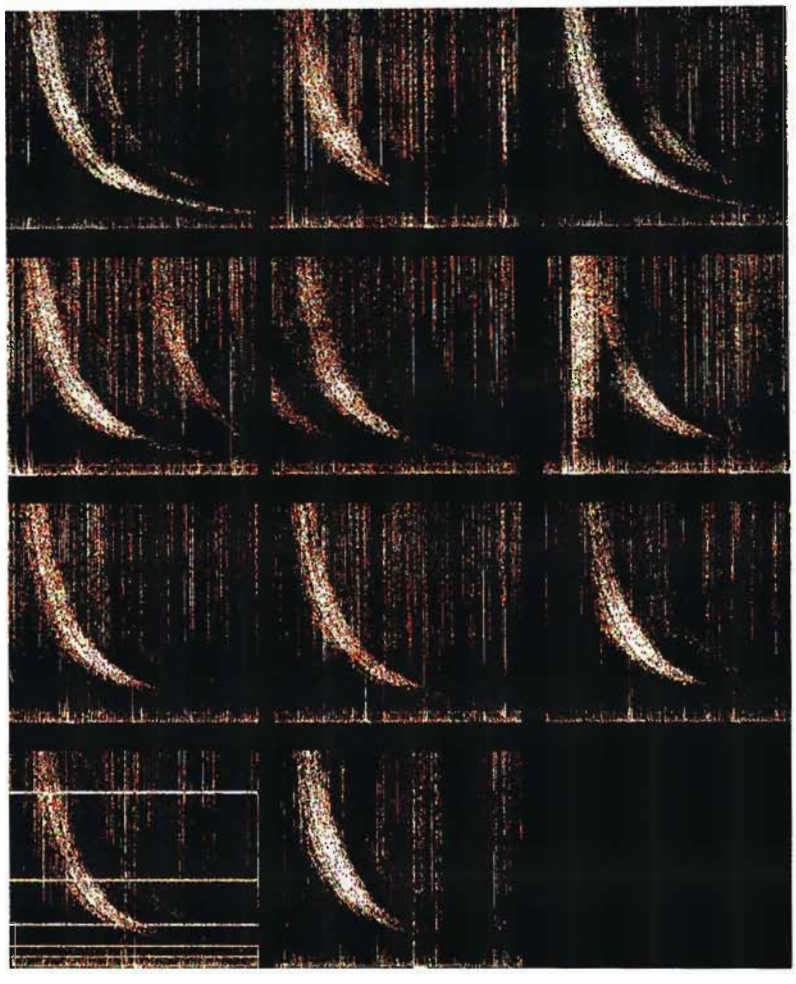

Figure 7.1: Spectrogram showing initial whistler groups and 'ghost' groups. Each spectrogram is 2.5s long and has a frequency range of 0 kHz to 10 kHz.

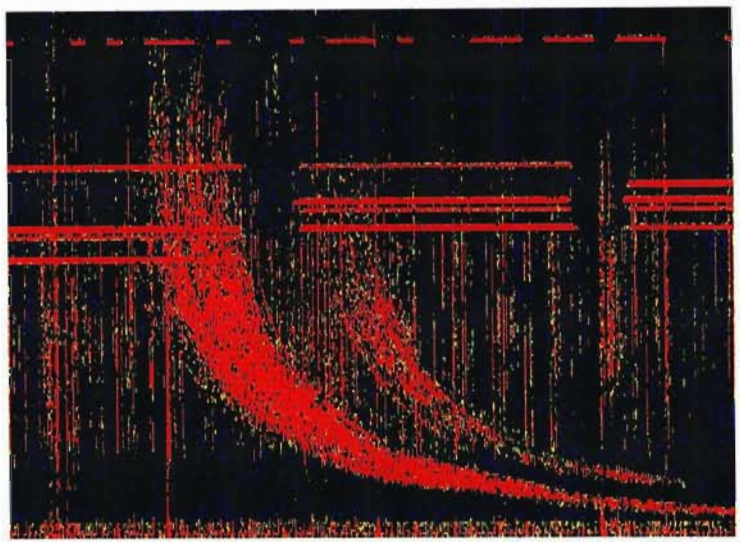

Figure 7.2: 0 kHz to 20 kHz spectrogram showing a whistler group and its 'ghost'.

were not clearly distinguishable over a long enough frequency range. Figure 7.2 shows the initial whistler group and 'ghost' group of frame 1 in figure 7.1 but with a frequency range of 0 kHz−20 kHz. The horizontal bars are the OMEGA pulses with the lowest at a frequency of 10.2 kHz and the highest at a frequency of 13.6 kHz. The continuous horizontal bands are MSK transmitters GBR (16.0 kHz) and FRA (18.3 kHz). The nose frequency of the trace on the leading edge of the initial whistler group is about 17.5 kHz while that of the trace on the trailing edge is 11.8 kHz. What is clear from the 'ghost' group is that the nose frequencies of traces within the group are certainly not less than 11.8 kHz and hence the whistlers can not have propagated through ducts with L-values higher than those of whistlers within the initial whistler group.

The 'ghost' group is certainly not a whistler echo as its dispersion would then be much greater than that of the initial whistler group. The delay between the two groups can also not be explained by sub-ionospheric propagation of the lightning energy. A possibility is that the 'ghost' group was generated by the same discharge as the initial whistler group but propagated through ducts with similar L-values but different electron tube content, resulting in a delayed arrival time. The dispersion of whistlers within the 'ghost' group would, if this was the case, be considerably different to the dispersion of whistlers within the initial whistler group.

The 'ghost' group was analysed by measuring the time between points, at the same frequency, on the initial whistler group and the 'ghost' group. This delay time was then measured for different frequencies. If the time between traces

within the two groups are the same at different frequencies then their dispersions must be the same. Initially the time difference between the leading edge and the trailing edge was measured. This gave an average delay time of 550 ms with a standard deviation of 55 ms. This was not an ideal method as it was not clear that the leading and trailing edges of the two groups corresponded to the same duct. Time differences were then measured between traces in the initial group and traces within the 'ghost' group that seemed to correspond. It was found that there were traces within the two groups whose delay times varied by only 20 ms over a 5 kHz frequency range (4 kHz−9 kHz). Since each spectra is 5 ms this gives a difference of only 4 spectra. Although not easy to determine an error for this technique this would probably fall within the expected error. This would seem to indicate that the dispersion of whistlers within the two groups are very similar and would seem to rule out the possibility of propagation through ducts with similar L-values but different electron tube content.

The delay time was also determined using cross correlation. Time series were generated by taking slices through the spectrograms at fixed frequencies. This was then divided into two time series each containing 128 points. The first covered the initial whistler group and the second the 'ghost' group. These two time series were then cross correlated. The start time of the time series containing the 'ghost' group was varied to maximise the correlation coefficient. The maximum correlation coefficients varied from 0.4 to 0.6. Although this correlation is not particularly good, the data was very noisy and the 'ghost' group was between 20 dB and 30 dB weaker than the initial whistler group. The duct structure also introduces problems with the correlation. As soon as the ducts overlap there will be some correlation. The maximum correlation coefficient would therefore be expected to be less than unity. The difference between the start times of the first and second time series gives the delay between the two whistler groups at that frequency. When possible, this process was repeated for different frequencies. The important point is that if the two signals have not propagated through the same ducts and hence do not have the same dispersion, the time shift that gives the best correlation should be different for different frequencies.

Figure 7.3 shows a spectrogram of an initial whistler group and its 'ghost' recorded at 17:49:10 UT. The horizontal red lines are the frequencies at which the above-mentioned cross correlation was performed. The frequencies are 4 kHz, 5.75 kHz and 7.5 kHz.

Figure 7.4 shows the results of the cross correlation. The top left frame is the result at a frequency of 4 kHz, the top right frame at 5.75 kHz and the bottom frame at 7.5 kHz. The correlation coefficients in the three cases are 0.47, 0.53 and 0.49 respectively. The time displacement on the x-axis indicates what shift the second time series needs, with respect to the first, to give the best correlation. A peak at zero therefore indicates that the best correlation occurs without any

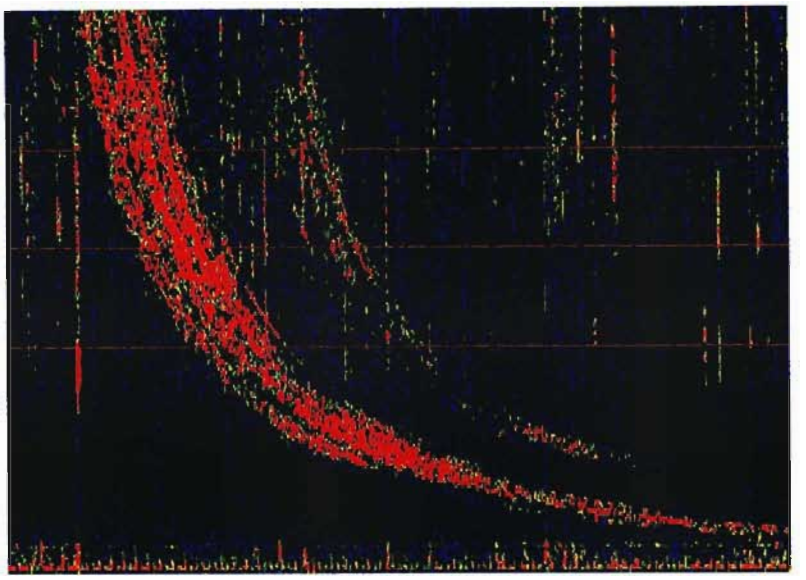

Figure 7.3: Spectrogram of whistler group and its associated 'ghost'. The horizontal lines are the frequencies at which the cross correllation was performed.

relative shift. In this case the start time of the second time series was varied to give a time displacement of zero. The difference between the start time of the two time series gives the delay time between the initial whistler group and the 'ghost' group. The time delays between the two time series were 508 ms at 4 kHz, 503 ms at 5.75 kHz and 498 ms at 7.5 kHz. Each spectra in the spectrogram of figure 7.3 is 5 ms and hence the time difference at 4 kHz differs from that at 7.5 kHz by only 2 spectra.

Figure 7.5 shows the time delays for all eleven events determined using cross correlation. The maximum is 669 ms, the minimum is 503 ms and the average is 565 ms. It was only possible in four of the events to obtain time delays at two frequencies that differed by more than 1 kHz. In these four cases the time delays at the different frequencies differed by a maximum of 14 ms (3 spectra).

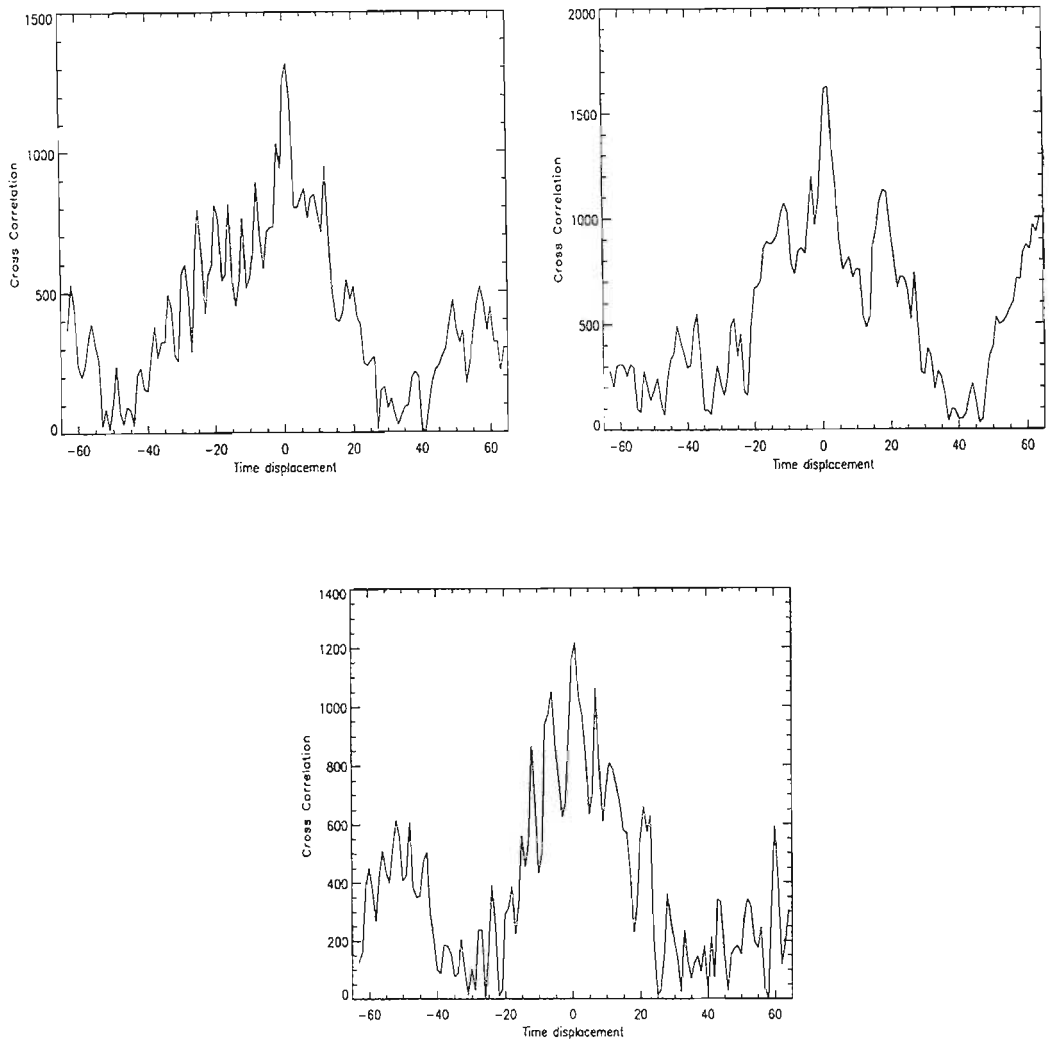

Figure 7.4: These three frames show the results of the correlation. The top left frame was performed at $4kHZ$, the top right frame at $5.75kHz$, and the bottom frame at $10kHz$.

These results seem to indicate that there are at least traces within the two whistler groups that have the same dispersion. If this is the case, then the two whistler groups must have been generated by different atmospheric discharges. As discussed in the previous chapter, the initial whistler group underwent a cyclotron resonance interaction with energetic electrons which precipitated near Marion Island causing a Trimpi observed on the VLF transmitter signal from Australia (NWC). These electrons mirrored in the north before precipitating in the south. It is thought that some of these electrons may have precipitated in the northern hemisphere, triggering an atmospheric discharge which is observed as the 'ghost' whistler group. Armstrong [1987] also suggested atmospheric discharges being

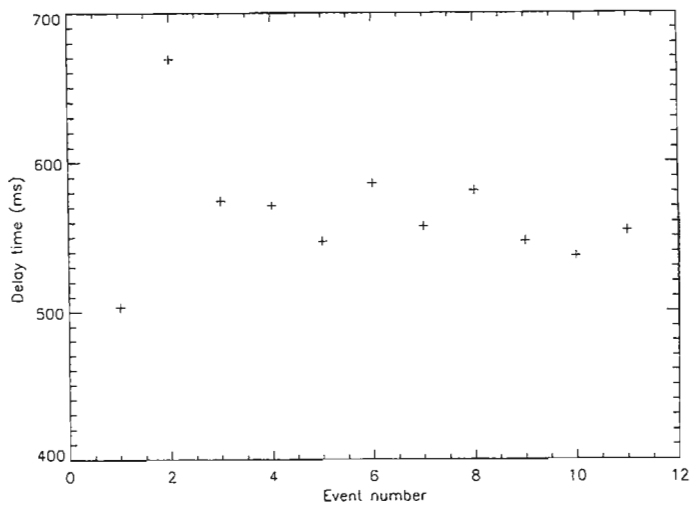

Figure 7.5: Time delays between the initial whistler group and the 'ghost' group for all eleven cases.

triggered by electron precipitation. His mechanism, however, involved whistler echoing and delay times between the first and second discharge of between 4 s and 5 s.

7.3 Expected Delay Times

If the wave-particle interaction region is near the geomagnetic equator, the time between the initiating atmospheric of the initial whistler group and the precipitation of energetic electrons, resonant with a wave of frequency ω, in the northern hemisphere would be $\frac{1}{4}\tau_B(\omega) + \frac{1}{2}\tau_W(\omega)$. Figure 7.6 shows this time against resonant frequency for an L-value of 2.68. Other L-values have not been considered as the electrons on $L = 2.68$ are the most energetic and hence would be the first to precipitate. The first electrons to precipitate would be those resonant with a wave frequency of 6 kHz and would precipitate 800 ms after the initiating atmospheric of the initial whistler group. If these electrons precipitate and trigger the atmospheric discharge associated with the whistler 'ghost', then this delay time should be approximately the same as the delay between the initial whistler group and the 'ghost' group.

The delay times obtained in the previous section were between 300 ms and 130 ms smaller than the 800 ms that would be expected if electrons precipitate after

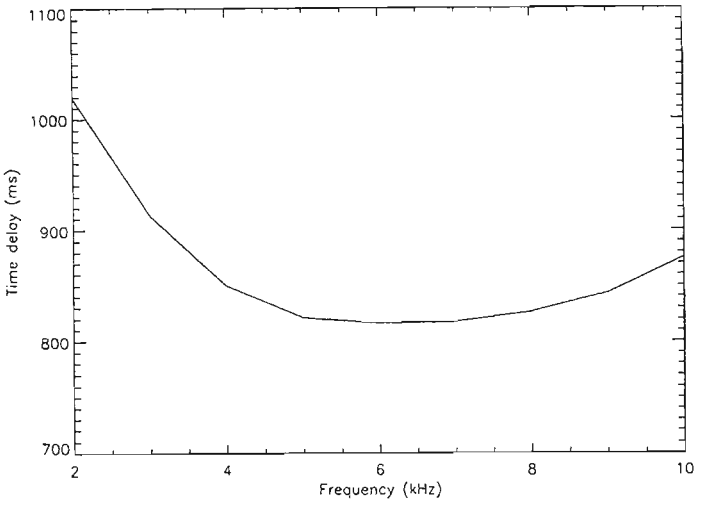

Figure 7.6: Predicted precipitation times, relative to the initiating atmospheric, in the northern hemisphere against resonant frequency.

a cyclotron resonance interaction near the geomagnetic equator. A possible explanation may be that the interaction region was actually north of the equatorial plane which would certainly reduce the delay time.

7.4 The Interaction Region

It has often been assumed that the optimum region for wave-particle resonance was near the geomagnetic equator. This is where the magnetic field changes slowly and the resonance condition can be maintained for the longest time. Kennel and Petscheck [1966] showed that wave growth through cyclotron resonance depends very strongly on the anisotropy of the electron pitch angle distribution. Liemohn [1967] subsequently showed that the optimum region for cyclotron resonance may be about 10^o from the equatorial plane due to enhanced pitch angle anisotropy. Hansen et al [1988] showed that correlated VLF wave emissions and auroral pulsations could be explained by a wave-particle interaction region 8000 km north of the equatorial plane on $L = 4$.

It is thought that the difference between the measured delay (between the initial whistler group and its 'ghost') and the delay calculated by assuming an interaction region near the geomagnetic equator, could also be explained if the interaction region was actually north of the equatorial plane. To determine the delay time

for an interaction region away from the equatorial plane, the wave and particles times must be calculated.

The wave travel times are calculated by ray tracing (using Haselgrove's [1954] ray tracing equations) through ducts superimposed on Park's [1972] DE1 density model. A dipole magnetic field model was assumed with a duct of width $W = 50$ km and enhancement $E = 0.15$ superimposed on $L = 2.68$. The electron travel times were calculated, as before, using equations (5.10) and (5.11) except that the integration limits in equation (5.11) now go from the latitude of the interaction region to the latitude at which the field line intersects the earth's atmosphere. The resonant velocity is calculated using equation (5.12), the electron cyclotron and plasma frequencies having been calculated using the density and magnetic field strength at the interaction region. These values are found from the density and magnetic field models used in the ray tracing.

Figure 7.7 shows the wave and resonant electron travel times for frequencies of 2 kHz, 4 kHz, 6 kHz and 8 kHz plotted against the geomagnetic co-latitude of the interaction region. The wave travel time is the time it takes for the wave to reach the interaction region and the electron travel time is the time it takes the electrons to get from the interaction region to the precipitation region. The delay time is therefore the sum of these two travel times and is also shown in figure 7.4. It is clear that the delay time decreases as the interaction region moves away from the geomagnetic equator and that the first electrons that would precipitate are those resonant with wave frequencies between 6 kHz and 8 kHz with those resonant with 4 kHz arriving only slightly later. The electrons resonant with a wave frequency of 2 kHz would precipitate between 200 ms and 100 ms later depending on the latitude of the interaction region. It can also be seen that the wave travel time is the major contribution to the precipitation delay at lower frequencies and makes a smaller contribution as the frequency increases. This is due to the whistler dispersion.

A minimum delay time of 500 ms (electrons resonant with wave frequencies between 6 kHz and 8 kHz) is obtained for an interaction region about 14^o from the geomagnetic equator. The delay time increases to 600 ms for an interaction region 10^o from the geomagnetic equator. An interaction region away from the equatorial plane agrees with the results obtained by Liemohn [1967] and Hansen et al [1988]. The delay between the initial whistler group and the 'ghost' group could then possibly be explained by an interaction region about 10^o to 15^o north of the equatorial plane.

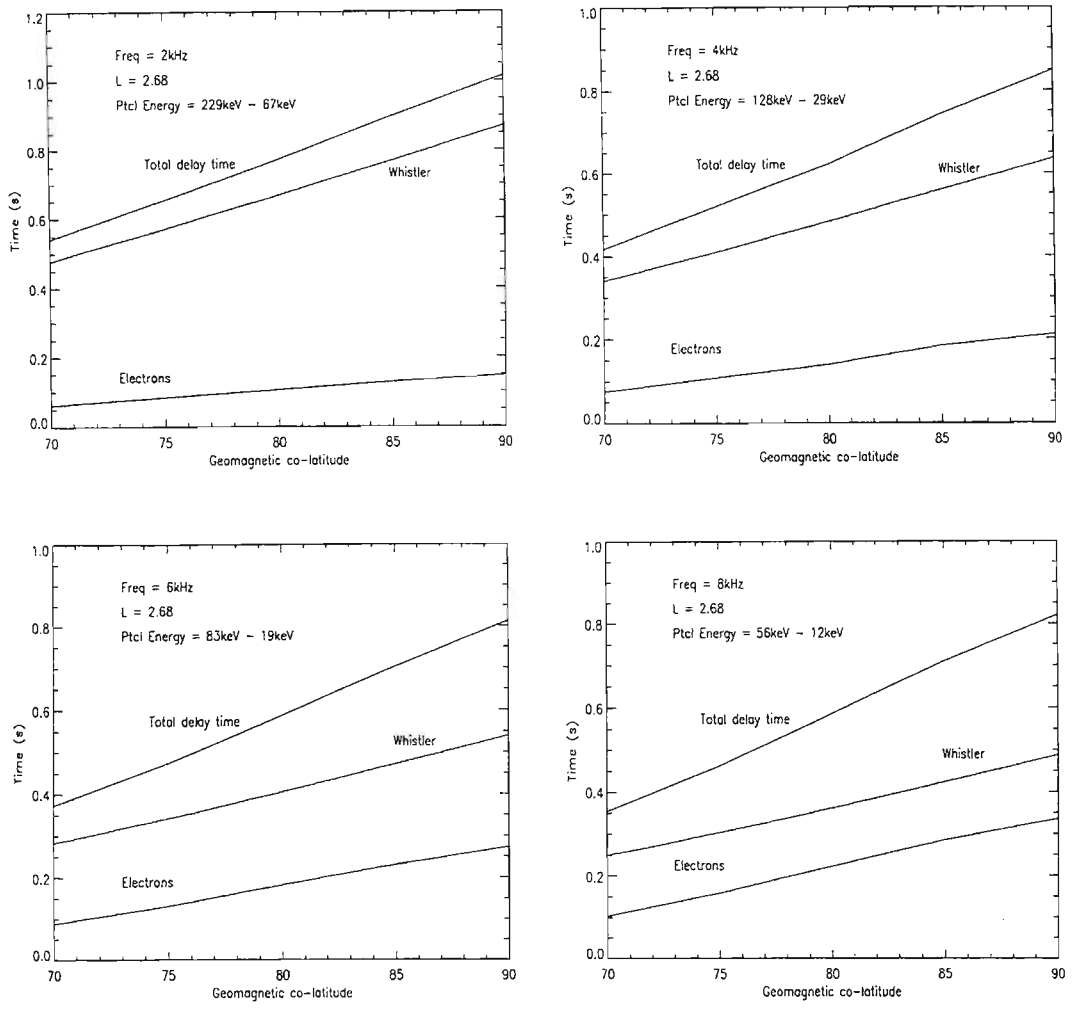

Figure 7.7: Wave and particle travel times for interaction regions away from the geomagnetic equator.

The above results have been obtained by assuming the equatorial pitch angle of the precipitating electrons is equal to the loss cone pitch angle. The justification for this is that the interaction between the whistlers and counterstreaming electrons will be very short and hence the change in pitch angle will be very small. If, however, the electrons were to diffuse further into the loss cone then the bounce period would be shorter and the electrons would precipitate slightly earlier. The only dependence on pitch angle appears in equation (5.11) which, for an equatorial pitch angle equal to the loss cone pitch angle on $L = 2.68$, returns a value of 1.2. The shortest bounce period will occur if the equatorial pitch angle becomes 0 in which case equation (5.11) returns a value of 1.0. From equation (5.10) it is clear that this would reduce the bounce period by 20% which, for electrons resonant with a wave frequency of 6 kHz on $L = 2.68$, would reduce the precipitation

time in the northern hemisphere by at most 60 ms. This is quite small and from figure 7.4 it can be inferred that even if the equatorial pitch angle were 0, the interaction region would still have to be almost 10^o north of the equatorial plane in order to explain the delay between the initial whistler group and the 'ghost' group.

The results obtained in the previous chapter were determined using an interaction region near the equatorial plane. An interaction 10^o north of the equatorial plane would reduce the precipitation time in both the northern and southern hemisphere by about 200 ms. This is half an omnipal sampling period and hence does not significantly change the results obtained in the previous chapter. For a given wave frequency, the resonant energy increases as the interaction region moves away from the equatorial plane. At the equatorial plane the resonant energy for an 8 kHz wave is about 5 keV. 10^o from the equatorial plane, the resonant energy increases to about 17 keV. In the previous chapter it was shown that the Trimpi onset continued until the precipitation of particles resonant with wave frequencies between 7 kHz and 8 kHz. This seemed to imply that electrons with energies down to about 5 keV could sustain an ionisation patch. This energy is lower than expected. If the interaction was, however, 10^o from the equatorial plane, the energies resonant with those wave frequencies would be closer to the expected energy.

7.5 Discussion and Conclusion

It is fairly clear that the Trimpis observed on the 19.8 kHz signal from Australia (NWC) were caused by the precipitation of energetic electrons into the upper atmosphere near Marion Island after mirroring in the northern hemisphere. Each Trimpi associated whistler group is followed, after a time of between 500 ms and 700 ms, by a second, fainter whistler group. It seems that the dispersion of whistlers within the two groups are the same and hence the two groups must have been generated by different atmospheric discharges. The time interval is such that the second discharge could have been triggered by electrons precipitated by the first whistlers. The delay could be more accurately explained if the wave-particle interaction occurred approximately 10^o north of the equatorial plane.

It was initially thought that the atmospheric discharge that produced the 'ghost' whistler group could be a cloud to ionosphere discharge (CID) such as a sprite. Dowden et al [1996a] suggested that sprites could be triggered by a meteor or cosmic ray shower after a cloud to ground discharge has set up a static electric field. In principle whistler induced electron precipitation could also be a mechanism for the triggering of sprites. Sprites have, however, been shown to occur within a

few milliseconds of their associated cloud to ground stroke (Lyons [1996]) which is not consistent with the 500 ms −700 ms delays observed in this case. Dowden et al [1996a] observed some cases in which the delay between the sprite and the parent lightning was $\sim$ 300 ms but assumed it was due to misidentification of the parent stroke.

Due to the length of a sprite discharge one would expect the radiated power to peak at a longer wavelength compared to a cloud to ground discharge. The 'ghost' whistler groups, although weaker than the initial whistler groups, had their maximum power in the same frequency band. This would also seem to indicate the 'ghost' whistlers were not generated by a sprite discharge unless the frequency profile of a ducted whistler mode signal depends more on the structure of the duct and propagation path than on the radiation source.

An obvious condition for the triggering of atmospheric discharges is that there must be thunderstorm conditions in the region of precipitation. Data obtained from both the Danish and Swedish lightning detection networks show thunderstorm activity near Marion Island's conjugate point. Figure 7.8 shows the positions of the lightning strikes detected by the Swedish detection system. The asterisk is the approximate position of Marion Island's conjugate point. There is, however, some doubt about this data as the results obtained by the Swedish and Danish detection systems for the same time and area show no common strikes. It is, however, fairly clear that there was thunderstorm activity in that region during the period of interest.

It has been shown (Hargreaves [1979] from Stringfellow [1974]) that there is a good correlation between solar activity and lightning activity with the minimum in lightning activity occurring near sunspot minimum. At sunspot minimum the energetic particle population is also less than at sunspot maximum and hence the chance of energetic particle precipitation is lowered. Although lightning activity may not be related to particle precipitation, this is at least not inconsistent with our results.

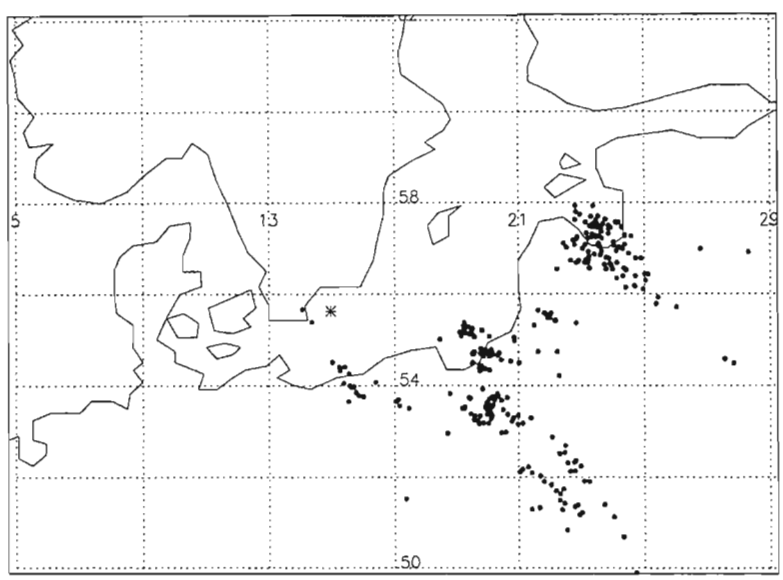

Figure 7.8: Map showing the positions of the lightning strikes detected by the Swedish detection network. Denmark and the lower portions of Sweden and Norway are visible.

Chapter 8

Conclusion and Suggestions for Future Work

8.1 Conclusion

This study has considered both fractional-hop whistlers, received on the ISIS2 satellite, and wave particle interactions observed as perturbations, known as Trimpis, on sub-ionospheric VLF transmitter signals. The Trimpi associated whistler groups were all followed by a second, fainter whistler group, which we have called a whistler 'ghost'. This is thought to indicate that energetic particle precipitation may trigger atmospheric discharges. Ray tracing is used to study the fractional-hop whistlers and is also used to model the Trimpis associated whistlers.

8.1.1 Low Latitude Fractional-Hop Whistlers

The dispersion of fractional-hop whistlers observed on the ISIS2 satellite at geomagnetic latitudes between 30^o and 0^o, was determined by Hughes [1981] and Hughes and Rice [1997]. Their results show dispersions that vary with latitude and shows dispersion branches that suggest that whistlers from both hemispheres and whistler echoes are present. This is studied by ray tracing signals, in an unducted mode, through realistic density and magnetic field models using Haselgrove's [1954] ray tracing equations.

The magnetic field is modelled using a centered dipole approximation. The density is modelled by matching a Chapman layer with a diffusive equilibrium model

(Angerami and Thomas [1964]) at an altitude of 500km. The proton concentration at the satellite altitude was determined (Hughes [1981] and Hughes and Rice [1997]) using the technique of Gurnett et al [1965] by measuring the cross-over frequency. The ion concentrations in the density model were then chosen to give, approximately, this proton concentration at the satellite altitude.

The latitudinal density gradient and the reference electron density were chosen such that the dispersions obtained through ray tracing unducted signals was the same as those obtained from the ISIS2 data. This condition was satisfied for signals from both hemisphere and for whistler echoes. The required density values at the F2 peak were found to be very similar to those recorded by ionosondes at the same time and at similar latitudes and longitudes. The model predicted that, at the higher satellite latitudes, the lower frequencies of the whistler echoes should undergo lower hybrid resonance reflection. Spectrograms of the satellite data show that the lower frequencies are indeed missing.

Determining the location of the initiating lightning strike was found to be very inaccurate although the frequency range of the signals from the far hemisphere may give some information regarding the thunderstorm region. If the higher frequencies are missing then the lightning region must be about 10^o equatorward of the ionospheric entry region. At best the lightning region can be determined to within about 4^o of latitude.

8.1.2 Whistlers and Trimpis

Whistlers and associated Trimpis were recorded on Marion Island during May 1996. The timing between the whistlers and Trimpis indicates that the whistlers underwent a cyclotron resonance interaction with counterstreaming electrons that must have mirrored in the north before precipitating near Marion Island. It is shown that the precipitation time of the energetic electrons and the onset of the Trimpis coincide. Assuming that the interaction region is near the equatorial plane, the Trimpi onset is shown to start at about the same time as the precipitation of electrons with energies of about $70keV$ and end at the same time as the precipitation of electrons with energies of about $15keV$ or lower. It was later shown that the interaction region may in fact be about 10^o north of the equatorial plane giving an energy range of between about $95keV$ and about $26keV$.

Using data obtained from the VLF Doppler (Thomson [1981]) an approximate precipitation region was determined. This showed that the Trimpis, all of which were observed on NWC, must have been caused by interference between the direct signal and one backscattered from the ionisation patch. The lack of Trimpis on GBR and FRA would indicate that the side lobes of the scattered signal must be very small.

8.1.3 Whistler 'Ghosts'

All of the Trimpi associated whistlers were followed, after a time of between $500ms-700ms$, by a second fainter whistler group which we have called a whistler 'ghost'. The timing between these two whistlers groups is such that if they have the same dispersion they must have been generated by different atmospheric discharges. Cross correlating time series containing the two whistler groups at different frequencies shows that there must be at least some components within the two whistler groups that have the same dispersion. The timing between the Trimpis and their associated whistlers showed that the energetic electrons must have mirrored in the north before precipitating near Marion Island. It is thought that some of these electrons could have precipitated in the northern hemisphere triggering the atmospheric discharge that is observed as a 'ghost'.

The delay between the two whistler groups was found to be smaller than expected if the interaction took place near the equatorial plane. By ray tracing signal through ducts of enhanced ionisation, using Park's [1972] DE-1 density model, it was found that the delay could be explained by an interaction region 10° north of the equatorial plane. Liemohn [1967] and Hansen [1988] have also suggested that the optimum region for wave particle interactions may be away from the equatorial plane.

Armstrong [1987] showed that almost in phase whistler echoes could also be explained by atmospheric discharges triggered by energetic particle precipitation. This mechanism, however, had a time constant of about $4s - 5s$. Dowden et al [1996c], in their study of RORD-Trimpi combinations, found that the whistler induced electron precipitation occurred above the sprite plasma. They suggested that the ducts may have been formed by the thunderstorm electric fields but didn't rule out the possibility that lightning may be triggered by whistler induced electron precipitation.

8.2 Suggestions for Future Work

8.2.1 Low Latitude Fractional-Hop Whistlers

The ray tracing was all done by assuming azimuthal symmetry and was therefore effectively in two dimensions. This could be extended to three dimensions and in fact a three dimensional ray tracing programme was written and tested. There was, however, no time to produce any results. The three dimensional ray tracing programme was also modified to use an IGRF field line model. This magnetic

model is more realistic than the centred dipole model and uses a geographic rather than a geomagnetic co-ordinate system. Initial results, however, indicate that the two magnetic models give very similar results. This could be more thoroughly explored.

8.2.2 Whistlers, Trimpis and Whistler 'Ghosts'

Although our results suggest that whistler induced electron precipitation may trigger atmospheric discharges, we have no mechanism for the triggering. It is clear that the electron precipitation, causing secondary ionisation, will increase the conductivity of the upper atmosphere and would modify any atmospheric electric fields. How this would trigger a discharge is not clear. Dowden et al [1996a] suggested that sprites could be triggered by a meteor or cosmic ray showers. We are, however, not suggesting that the discharge observed as a ghost is a sprite. Future work could include a study of how the precipitation and subsequent ionisation can trigger a discharge and what kind of discharge is triggered.

Appendix A

Fortran Programme for Ray Tracing

A.1 Introduction

This appendix contains the Fortran code used in the ray tracing calculations. The initial conditions are defined by the user in subroutine para. The ionospheric entry point and refracted wave normal angle are then determined. The four first order differential equations are defined in subroutine DYBDX. These are called by subroutine RKG which uses a fourth order Runge-Kutta technique to solve the differential equations. At each point in space the phase refractive index and derivatives are determined in subroutine Setup which uses subroutines Refind and Density (electron and ion densities). The programme stops when it has reached the satellite height a predefined number of times or if a certain number of steps has passed.

A.2 Fortran Code

```
      Program TwoDraytra
C*****************************************************************
C  This programme computes the path of a whistler mode wave through
C  the ionosphere and magnetosphere.  It uses Stix's [1962] equations
C  for the phase refractive index. A Chapman layer and a diffusive
C  equilibrium model, matched at 500km, are used for the ionosphere
C  and magnetosphere. A dipole field is used to model the earth's
C  magnetic field.
C
C  Updated : 2 October 1996
C*****************************************************************
      Real*8 mu,DmuBDpsi,DmuBDw,DmuBDr,DmuBDO
      Real*8 freq,omega,xi,alpha,thetao,hbi
      Real*8 Me,Mp,MHe,MO,MO2,MNO
      Real*8 Pi,Eps,QQ,k,c,Re
      Real*8 Ro,To,go,om,m
      Real*8 theta,beta,P,inc
      Real*8 degconv,radconv,dS,S,Y1,Y2
      Real*8 Y,Q,xx,yy
      Real*8 ne,np,nHe,nO
      Real*8 Local_strat
      Real*8 Dip,phi,psi,mu1
      External DyBDx
      Dimension Y(4),Q(4)
      Integer NumCross,Npts,done
      Common /cm2/ Me,Mp,MHe,MO,MO2,MNO
      Common /cm3/ Pi,Eps,QQ,k,c,Re
      Common /cm4/ Ro,To,go,om,m
C *****************************************************************
C  Relevant parameters:
C  -------------------
C  R         :  Starting height (m)
C  theta       :  latitude
C  psi          :  angle between wave normal and magnetic field
C  xi           :  angle between wave normal and radial vector
C  freq         :  freq of wave (Hz)
C  omega        :  angular frequency (rad/sec)
C  inc          :  increment (km)
C  degconv    :  conversion degrees to radians
C  radconv     :  conversion radians to degrees
```

```
C ***************************************************************
C
C ***************************************************************
C  Constants.
C ***************************************************************
      Pi = DACos(0.0D0)*2.0D0
      Eps = 8.854D-12           !  epsilon
      QQ = 1.602D-19      !  electron charge
      k = 1.38D-23           !  Boltzmann's constant
      c = 3.0D8                !  speed of light
      Re = 6371200.0D0    !  Radius of earth
      Me = 9.1D-31          !  electron mass
      Mp = 1.67D-27        !  proton mass
      MHe= 6.7D-27        !  Helium mass
      MO = 26.7D-27       !  Oxygen mass
      MO2=53.4D-27       !  O2+ mass
      MNO=50.1D-27             !  NO+ mass
C ***************************************************************
C  Reference values
C ***************************************************************
      Ro=6870000.0D0     !  Reference altitude
      To=1200.0D0          !  Reference Temperatures
      go=8.45D0             !  Reference gravitational force
      om=7.27D-5            !  Angular velocity of earth
      m=1.85D-3            !  Temperature gradient
C ***************************************************************
C  Initial Parameters
C ***************************************************************
      Call Para(theta,beta,P,inc,freq)
C ***************************************************************
C  Conversion of degrees to radians and Hz to rad/sec
C ***************************************************************
      degconv = Pi/180.0D0
      radconv = 1.0D0/degconv
      theta = theta*degconv
      theta = Pi/2.0D0-theta
      beta = beta*degconv
      omega = 2.0D0*Pi*freq
C ***************************************************************
C  Initial conditions for Runge-Kutta routine.
C ***************************************************************
      Open(10,File='2k30echo.dat')    ! Open output files
      Open(11,File='rthet.dat')
```

```
      Open(12,File='theta.dat')
C
      hbi = 100000.0D0                        !  height of ionosphere base
      thetao = theta                          !  initial latitude
      xx=6371.2D0*DCos(Pi/2.0D0 - thetao)     !  Cartesian co-ords of initial
      yy=6371.2D0*DSin(Pi/2.0D0 - thetao)     !  point.
      NumCross = 0                            !  no. of crossings of  satellite
C                                             !  altitude
      If (beta .LT. 0.0D0) then
        alpha=-1.0D0*DACos((Re*DSin(-1.0D0*beta)*DSin(-1.0D0*beta)+
     *        DCos(-1.0*beta)*DSqrt((Re+hbi)*(Re+hbi)-Re*Re*
     *        DSin(-1.0D0*beta)*DSin(-1.0D0*beta)))/(Re+hbi))
      Else
        alpha=DACos((Re*DSin(beta)*DSin(beta)+DCos(beta)*
     *        DSqrt((Re+hbi)*(Re+hbi)-Re*Re*DSin(beta)*DSin(beta)))/
     *        (Re+hbi))
      End If
      theta = thetao + alpha
      Write(6,*) alpha,alpha*180.0D0/Pi
      xi = beta-alpha
C
      Y(1)=Re + hbi         !  radial distance at base of ionosphere.
      Y(2)=theta            !  latitude.
      Y(3)=xi               !  angle between wave norm and rad direction.
      Y(4)=0.0D0            !  distance travelled at c (P).
C
      Q(1)=0.0D0
      Q(2)=0.0D0
      Q(3)=0.0D0
      Q(4)=0.0D0
C
      Write(6,*) Y(1) - Re
      Write(6,*) xi,90.0D0-Y(2)*180.0D0/3.14159D0
      Write(6,*) xi,Local_strat
      Call Init_conds(omega,Y,xi) ! Determine initial conditions on
      Write(6,*) xi,Y(3),'   x'    ! refraction.
C
      S=0.0D0
      Y1=Y(1)
      Y2=Y(2)
      Npts=0
      xx=Y(1)*DCos(Y(2))/1000.0D0
      yy=Y(1)*DSin(Y(2))/1000.0D0
```

```
C
      Write(6,*) Y(1),Y(2)*180.0D0/3.14159
      done = 0
      Do While (NumCross .LT. 2)          ! Continue until signal has crossed
        If (NumCross .EQ. 0) Then         ! satellite altitude twice.
          If (Y(1) .GT. 7770000.0D0) Then
             NumCross = NumCross + 1
          End If
        End If
        If (NumCross .EQ. 1) Then
          If (Y(1) .LT. 7770000.0D0) Then
            NumCross = NumCross + 1
          End If
        End If
        If (NumCross .EQ. 2) Then
          If (Y(1) .GT. 7770000.0D0) Then
            NumCross = NumCross + 1
          End If
        End If
        If (NumCross .EQ. 3) Then
          If (Y(1) .LT. 7770000.0D0) Then
            NumCross = NumCross + 1
          End If
        End If
        If (Y(1) .LT. 6471000.0D0) Then  !  Reflection of signal.
          If (Npts .GT. 500) Then
             Write(6,*) Y(3), mu
             xi = Y(3)
             mu1 = mu
             Call Reflect_conds(mu1,omega,Y,xi)
             Write(6,*) Y(3)
             Npts = 0
          End If
        End If
        If ((Y(1) .GT. 7760000.0D0) .AND. (Y(1) .LT. 7780000.0D0)) Then
           Inc = 250.0D0
        EndIf
        If (Y(1) .GT. 7780000.0D0) Then
           Inc = 2000.0D0
        EndIf
        If (Y(1) .LT. 6490000.0D0) Then
           Inc = 250.0D0
        EndIf
```

```
        If ((Y(1) .GT. 6490000.0D0) .AND. (Y(1) .LT. 7760000.0D0)) Then
           Inc = 2000.0D0
        EndIf
        Npts=Npts+1
        Call RKG(Y,4,DyBDx,inc,Q,omega)
        dS=Y1*Y1+Y(1)*Y(1)-2.0D0*Y1*Y(1)*DCos(ABS(Y(2)-Y2))
        S=S+DSqrt(dS)
        Y1=Y(1)
        Y2=Y(2)
        If (Mod(Npts,150) .EQ. 0) Then
          Call Setup(omega,Y,mu,DmuBDpsi,DmuBDw,DmuBDr,DmuBD0)
          Call Density(Y(1),Pi/2.0D0 - Y(2),ne,np,nHe,n0)
          Dip=DAtan(2.0D0*DTan(Pi/2.0D0 - Y(2)))
          phi = 3.0D0*Pi/2.0D0-Dip
          psi=  Y(3) - phi
          xx = Y(1)*DSin(Y(2))/1000.0D0
          yy = Y(1)*DCos(Y(2))/1000.0D0
          Write(10,*) xx,yy
          Write(6,*) Y(1),Y(2),Y(3),psi
          Write(11,*) Y(1),Y(2),Y(3), Y(4)
          Write(6,*) NumCross,inc, Npts
        End If
        If (Npts .GT. 200000) Then
           NumCross = 2
        EndIf
      End Do
      xx = Y(1)*DCos(Y(2))/1000.0D0
      yy = Y(1)*DSin(Y(2))/1000.0D0
      Write(10,*) xx,yy
      Write(11,*) Y(1),Y(2)*180.0D0/Pi,Y(3),Y(4)/3.0D8,S,psi
      Write(10,*) Y(1),Y(2),Y(3),S
C
      Close(12)
      Close(11)
      Close(10)
C
      End
C*********************************************************************
C   Subroutine Para: Sets the initial conditions.
C*********************************************************************
C
      Subroutine Para(theta,beta,P,inc,freq)
      Real*8 theta,beta,P,inc,freq
```

```
C
      theta = -24.688D0     !  Initial latitude.
      beta=-60.0D0 !  Initial wave normal angle.
      P=0.0D0 !  Initial equivalent distance.
      freq=2000.0D0 !  Frequency in Hertz.
      inc=2000.0D0 !  Increment
C
      Return
      End
C
C*********************************************************************
C  Common data block
C*********************************************************************
C
      Block Data Sub
      Real*8 FOe,FOp,FOHe,FOO,Fhe,Fhp,FhHe,FhO
      Real*8 Me,Mp,MHe,MO,MO2,MNO
      Real*8 Pi,Eps,QQ,k,c,Re
      Real*8 Ro,To,go,om,m
C
      Common /cm1/ FOe,FOp,FOHe,FOO,Fhe,Fhp,FhHe,FhO
      Common /cm2/ Me,Mp,MHe,MO,MO2,MNO
      Common /cm3/ Pi,Eps,QQ,k,c,Re
      Common /cm4/ Ro,To,go,om,m
C
      End
C
C ****************************************************************
C  Subroutine Init_conds:  Determines refracted wave normal angle
C    on entering the ionosphere.
C ****************************************************************
C
      Subroutine Init_conds(omega,Y,xi)
C
      Real*8 omega,Y,xi
      Real*8 q,temp,temp_init
      Real*8 mu,DmuBDpsi,DmuBDw,DmuBDr,DmuBDO
      Dimension Y(4)
C
      Y(3) = Y(3) + 0.9D0
      Call Setup(omega,Y,mu,DmuBDpsi,DmuBDw,DmuBDr,DmuBDO)
      q = mu*DCos(Y(3)-local_strat)
      temp = mu*mu-1.0D0+DCos(xi)*DCos(xi)-q*q
```

```
      Write(6,*) temp,mu,xi,'   mu'
      Write(6,*) DSin(xi),mu*DSin(Y(3))
      temp_init = temp
      If (temp_init .LT. 0.0D0) temp = -temp
      Do While (temp .GT. 0.00D0)
        If (xi .GT. 0.0D0) Then
          Y(3) = Y(3) - 0.00001D0
        Else
          Y(3) = Y(3) + 0.00001D0
        End If
        Write(6,*) xi,Y(3),temp
        Call Setup(omega,Y,mu,DmuBDpsi,DmuBDw,DmuBDr,DmuBD0)
        q = mu*DCos(Y(3)-Local_strat)
        temp = mu*mu-1.0D0+DCos(xi)*DCos(xi)-q*q
        If (temp_init .LT. 0.0D0) temp = -temp
      End Do
      Write(6,*) Y(3)
C
      Return
      End
C
C ***********************************************************************
C     Subroutine Reflect_conds(mu1,omega,Y,xi) : Determines the
C       reflected wave normal angle when the signal reaches the
C       base of the ionosphere.
C ***********************************************************************
C
      Real*8 mu1,omega,Y,xi
      Real*8 mu,DmuBDpsi,DmuBDw,DmuBDr,DmuBD0
      Dimension Y(4)
C
      Y(3) = 0.45D0
      Write(6,*) Y(3), xi
      Call Setup(omega,Y,mu,DmuBDpsi,DmuBDw,DmuBDr,DmuBD0)
      Do While (mu1*DSin(xi) - mu*DSin(Y(3)) .GT. 0.0D0)
          Y(3) = Y(3) + 0.00001D0
          Write(6,*) mu1*DSin(xi), mu*DSin(Y(3)), Y(3), mu
          Call Setup(omega,Y,mu,DmuBDpsi,DmuBDw,DmuBDr,DmuBD0)
      End Do
      Write(6,*) Y(3), xi
C
      Return
      End
```

```
C
C ***********************************************************************
C  Subroutine DyBDx:  The array F is equal to the RHS of the
C    raytracing equations.  F(1) is dr/dt, F(2) is dtheta/dt,
C    F(3) is dxi/dt and F(4) is dP/dt.  The array Y is the array of
C    dependent variables where Y(1) is r, Y(2) is theta, Y(3) is xi
C    and Y(4) is P.
C ***********************************************************************
C
      Subroutine DyBDx(Y,F,omega)
      Real*8 Y,F,omega
      Real*8 mu,DmuBDpsi,DmuBDw,DmuBDr,DmuBD0
      Real*8 Pi,Eps,QQ,k,c,Re
      Common /cm3/ Pi,Eps,QQ,k,c,Re
      Dimension Y(4),F(4)
C
      Call Setup(omega,Y,mu,DmuBDpsi,DmuBDw,DmuBDr,DmuBD0)
      F(1) = 1.0/(mu*mu)*(mu*DCos(Y(3)) + DSin(Y(3))*DmuBDpsi)
      F(2) = 1.0/(Y(1)*mu*mu)*(mu*DSin(Y(3))-DCos(Y(3))*DmuBDpsi)
      F(3) = 1.0/(Y(1)*mu*mu)*(DmuBD0*DCos(Y(3)) -
     *       (Y(1)*DmuBDr+mu)*DSin(Y(3)))
      F(4) = 1.0 + omega/mu*DmuBDw
C
      Return
      End
C
C ***********************************************************************
C  Subroutine setup:  This routine determines the phase refractive
C   index and its derivatives which are used by the ray tracing
C   equations.
C ***********************************************************************
C
      Subroutine Setup(omega,Y,mu,DmuBDpsi,DmuBDw,DmuBDr,DmuBD0)
C
      Real*8 ne,np,n0,nHe,mu
      Real*8 DmuBDpsi,DmuBDw,DmuBDr,DmuBD0
      Real*8 B,omega,Dip,phi,psi
      Real*8 F0e,F0p,F0He,F00,Fhe,Fhp,FhHe,Fh0
      Real*8 Me,Mp,MHe,M0,M02,MN0
      Real*8 Pi,Eps,QQ,k,c,Re
      Real*8 dx
      Real*8 Y,fx
      Dimension fx(2),Y(4)
```

```
      Integer I
      Common /cm1/ F0e,F0p,F0He,F00,Fhe,Fhp,FhHe,Fh0
      Common /cm2/ Me,Mp,MHe,M0,M02,MN0
      Common /cm3/ Pi,Eps,QQ,k,c,Re
C
      dx=1.0D-3
      Do I=1,2
        Dip=DAtan(2.0D0*DTan(Pi/2.0D0 - Y(2)))     !  Dip angle
        phi = 3.0D0*Pi/2.0D0-Dip
        psi=  Y(3) - phi !  Angle between wave normal and
        If (I .EQ. 1) Then !  magnetic field.
          Call MagField(Y(1)+dx/2.0D0,Pi/2.0D0 - Y(2),B) ! Mag field and
          Call Density(Y(1)+dx/2.0D0,Pi/2.0D0 - Y(2),ne,np,nHe,n0) ! density at
        Else                                                       ! r, theta
          Call MagField(Y(1)-dx/2.0D0,Pi/2.0D0 - Y(2),B)
          Call Density(Y(1)-dx/2.0D0,Pi/2.0D0 - Y(2),ne,np,nHe,n0)
        EndIf
        F0e = ne*QQ*QQ/(Me*Eps)
        F0e = DSqrt(F0e) !  Electron plasmafrequency.
        F0p = np*QQ*QQ/(Mp*Eps)
        F0p = DSqrt(F0p) !  Proton plasmafrequency.
        F0He = nHe*QQ*QQ/(MHe*Eps)
        F0He = DSqrt(F0He) !  Helium plasmafrequency.
        F00 = n0*QQ*QQ/(M0*Eps)
        F00 = DSqrt(F00) !  Oxygen plasmafrequency.
        Fhe = QQ*B/Me !  Electron gyrofrequency.
        Fhp = QQ*B/Mp !  Proton gyrofrequency.
        Fh0 = QQ*B/M0 !  Oxygen gyrofrequency.
        FhHe = QQ*B/MHe !  Helium gyrofrequency.
        Call Refind(omega,psi,mu,DmuBDpsi,DmuBDw)   ! Refractive index
        fx(I)=mu                                    ! r, theta.
      End Do
      DMuBDr=(fx(1)-fx(2))/dx !  Derivative of refractive index w.r.t. r.
C
      dx=1.0D-3
      Do I=1,2
        If (I .EQ. 1) Then
          Dip=DAtan(2.0D0*DTan(Pi/2.0D0 - (Y(2)+dx/2.0D0)))
        Else
          Dip=DAtan(2.0D0*DTan(Pi/2.0D0 - (Y(2)-dx/2.0D0)))
        EndIf
        phi = 3.0D0*Pi/2.0D0-Dip
        psi=  Y(3) - phi
```

```
        If (I .EQ. 1) Then
          Call MagField(Y(1),Pi/2.0D0-(Y(2)+dx/2.0D0),B)
          Call Density(Y(1),Pi/2.0D0-(Y(2)+dx/2.0D0),ne,np,nHe,nO)
        Else
          Call MagField(Y(1),Pi/2.0D0-(Y(2)-dx/2.0D0),B)
          Call Density(Y(1),Pi/2.0D0-(Y(2)-dx/2.0D0),ne,np,nHe,nO)
        EndIf
        FOe = ne*QQ*QQ/(Me*Eps)
        FOe = DSqrt(FOe)
        FOp = np*QQ*QQ/(Mp*Eps)
        FOp = DSqrt(FOp)
        FOHe = nHe*QQ*QQ/(MHe*Eps)
        FOHe = DSqrt(FOHe)
        FOO = nO*QQ*QQ/(MO*Eps)
        FOO = DSqrt(FOO)
        Fhe = QQ*B/Me
        Fhp = QQ*B/Mp
        FhO = QQ*B/MO
        FhHe = QQ*B/MHe
        Call Refind(omega,psi,mu,DmuBDpsi,DmuBDw)
        fx(I)=mu
      End Do
      DMuBDO=(fx(1)-fx(2))/dx    !  Derivative of refractive index w.r.t.
C                                !  theta.
      Dip=DAtan(2.0D0*DTan(Pi/2.0D0-Y(2)))
      phi = 3.0D0*Pi/2.0D0-Dip
      psi=  Y(3) - phi
      Call MagField(Y(1),Pi/2.0D0-Y(2),B)
      Call Density(Y(1),Pi/2.0D0-Y(2),ne,np,nHe,nO)
      FOe = ne*QQ*QQ/(Me*Eps)
      FOe = DSqrt(FOe)
      FOp = np*QQ*QQ/(Mp*Eps)
      FOp = DSqrt(FOp)
      FOHe = nHe*QQ*QQ/(MHe*Eps)
      FOHe = DSqrt(FOHe)
      FOO = nO*QQ*QQ/(MO*Eps)
      FOO = DSqrt(FOO)
      Fhe = QQ*B/Me
      Fhp = QQ*B/Mp
      FhO = QQ*B/MO
      FhHe = QQ*B/MHe
      Call Refind(omega,psi,mu,DmuBDpsi,DmuBDw)       ! Refractive index.
C
```

```
      Return
      End
C
C*********************************************************************
C  Subroutine density :  Gives ion and electron densities as function
C    of altitude and latitude.
C *********************************************************************
C
      Subroutine Density(R,theta,ne,np,nHe,nO)
      Real*8 R,theta,ne,np,nHe,nO
      Real*8 Pi,Eps,QQ,k,c,Re
      Common /cm3/ Pi,Eps,QQ,k,c,Re
C
      If ((R-Re) .LT. 500000.0D0) Then
        Call Chapman(R,theta,ne,np,nHe,nO)  !  Chapman layer below 500km.
      Else
        Call Diffeq(R,theta,ne,np,nHe,nO)   !  Diffusive equilibrium above 500k
      End If
C
      Return
      End
C
C *********************************************************************
C  This subroutine determines the temperature.
C *********************************************************************
      Real*8 Function Temperature(R)
      Real*8 R
      Real*8 Ro,To,go,om,m
      Common /cm4/ Ro,To,go,om,m
C
      Temperature=To+m*(R-Ro)          !  Linearly increasing temperature
C
      Return
      End
C
C *********************************************************************
C  Function Findz : Determines the z value used to matching the two
C    density models.
C *********************************************************************
      Real*8 Function Findz(z,ni,DniBDr,Hi,temp)
      Real*8 z,ni,DniBDr,Hi,temp
      Real*8 temp1
C
```

```
      temp1 = 1.0D0/Hi-(z/Hi)*temp
      Findz = 0.5D0*ni*(DExp(-z)-1.0D0)*temp1 - DniBDr
C
      Return
      End
C
C ***********************************************************************
C  Subroutine chapman : Determines the ion and electron densities using
C    Chapman's production function.
C ***********************************************************************
      Subroutine Chapman(R,theta,ne,np,nHe,nO)
C
      Real*8 R,theta,ne,np,nHe,nO,nO2,nNO
      Real*8 h,hmO,hmp,hmHe,hmO2,hmNO,HO,Hp,HHe,HO2,HNO
      Real*8 Hp500,HHe500,HO500,RRo
      Real*8 T,T500,a,g,g500
      Real*8 nmO,nmp,nmHe,nmO2,nmNO
      Real*8 DnpBDr,DnHeBDr,DnOBDr,DneBDr
      Real*8 Me,Mp,MHe,MO,MO2,MNO
      Real*8 Pi,Eps,QQ,k,c,Re
      Real*8 Ro,To,go,om,m
      Real*8 z,temp,fx,dx
      Real*8 ZBrent,Findz,Temperature
      Integer I
      External ZBrent,Findz,Temperature
      Dimension fx(2)
      Common /cm2/ Me,Mp,MHe,MO,MO2,MNO
      Common /cm3/ Pi,Eps,QQ,k,c,Re
      Common /cm4/ Ro,To,go,om,m
C
      h=R-Re
      g=6.670D-11*5.98D24/(R*R)
      g500=6.670D-11*5.98D24/(6870000.0D0*6870000.0D0)  ! gravit force at
      RRo=R/Ro                                          ! matching height.
      T=843.0D !  Isothermal Chapman temperature.
      T500=843.0D0
      HO=k*T/(MO*g) !  Oxygen scale height.
      HO500 = k*T500/(MO*g500)
      Hp=k*T/(Mp*g) !  Proton scale height.
      Hp500 = k*T500/(Mp*g500)
      HHe=k*T/(MHe*g) !  Helium scale height.
      HHe500 = k*T500/(MHe*g500)
      HO2=k*T/(MO2*g) !  O2 scale height.
```

```
      HNO=k*T/(MNO*g) !  NO scale height
C
      dx = 1.0D0
C
      Call Diffeq(Ro+dx/2.0D0,theta,ne,np,nHe,nO)
      fx(1) = ne
      Call Diffeq(Ro-dx/2.0D0,theta,ne,np,nHe,nO)
      fx(2) = ne
      DneBDR = (fx(1)-fx(2))/dx   !  Rate of change of electron density with
C                                 !  height.
      Call Diffeq(Ro+dx/2.0D0,theta,ne,np,nHe,nO)
      fx(1) = np
      Call Diffeq(Ro-dx/2.0D0,theta,ne,np,nHe,nO)
      fx(2) = np
      DnpBDR = (fx(1) - fx(2))/dx
      temp = T500*k/(Mp*g500*g500)*6.670D-11*5.98D24/(Ro*Ro*Ro)
c      Do I = 0,50
c       Write(6,*) Findz(-0.1D0*I,np,DnpBDR,Hp500,temp),0.1D0*I
c      End Do
      z = ZBrent(Findz,np,DnpBDr,Hp500,temp,-3.0D0,-1.5D0,1.0D-12)
      hmp = 500000.0D0 - z*Hp500           !  Height of maximum proton conc.
      nmp = np/DSqrt(DExp(1.0D0-z-exp(-z)))!  Maximum proton density.
C      Write(6,*) hmp,nmp
C
      Call Diffeq(Ro+dx/2.0D0,theta,ne,np,nHe,nO)
      fx(1) = nHe
      Call Diffeq(Ro-dx/2.0D0,theta,ne,np,nHe,nO)
      fx(2) = nHe
      DnHeBDR = (fx(1) - fx(2))/dx
      temp = T500*k/(MHe*g500*g500)*6.67D-11*5.98D24/(Ro*Ro*Ro)
c      Do I = 0,50
c       Write(6,*) Findz(-0.1D0*I,nHe,DnHeBDR,HHe500,temp),0.1D0*I
c      End Do
      z = ZBrent(Findz,nHe,DnHeBDr,HHe500,temp,-1.5D0,0.0D0,1.0D-12)
      hmHe = 500000.0D0 - z*HHe500        !  Height of maximum helium conc.
      nmHe = nHe/DSqrt(DExp(1-z-exp(-z))) !  Maximum helium density.
C      Write(6,*) hmHe,nmHe
C
      Call Diffeq(Ro+dx/2.0D0,theta,ne,np,nHe,nO)
      fx(1) = nO
      Call Diffeq(Ro-dx/2.0D0,theta,ne,np,nHe,nO)
      fx(2) = nO
      DnOBDR = (fx(1) - fx(2))/dx
```

```
      temp = T500*k/(M0*g500*g500)*6.67D-11*5.98D24/(Ro*Ro*Ro)
c      Do I = 0,50
c       Write(6,*) Findz(0.2D0*I,n0,Dn0BDR,H0500,temp),0.2D0*I
c      End Do
      z = ZBrent(Findz,n0,Dn0BDr,H0500,temp,3.0D0,5.0D0,1.0D-12)
      hm0 = 500000.0D0 - z*H0500        !  Height of maximum oxygen conc.
      nm0 = n0/DSqrt(DExp(1-z-exp(-z))) !  Maximum oxygen density.
C      Write(6,*) hm0,nm0
C
      hm02=135000.0D0 !  Height of maximum 02 conc.
      nm02=7.5D9                !  Maximum 02 density.
C
      hmN0=170000.0D0 !  Height of maximum N0 conc.
      nmN0=1.0D10               !  Maximum N0 density.
C
      n0=nm0*DSqrt(DExp(1.0D0-(h-hm0)/H0-DExp(-(h-hm0)/H0)))
      np=nmp*DSqrt(DExp(1.0D0-(h-hmp)/Hp-DExp(-(h-hmp)/Hp)))
      nHe=nmHe*DSqrt(DExp(1.0D0-(h-hmHe)/HHe-DExp(-(h-hmHe)/HHe)))
      n02=nm02*DSqrt(DExp(1.0D0-(h-hm02)/H02-DExp(-(h-hm02)/H02)))
      nN0=nmN0*DSqrt(DExp(1.0D0-(h-hmN0)/HN0-DExp(-(h-hmN0)/HN0)))
C
      ne=n0+np+nHe+n02+nN0  !  Electron density through quasi neutrality.
C
      Return
      End
C
C*********************************************************************
C  Function zgravit : This function determines the gravitational force
C    term of the temperature modified geopotential height.
C*********************************************************************
      Real*8 Function zgravit(R)
      Real*8 R
      Real*8 term1,term2
      Real*8 T,Temperature
      Real*8 Ro,To,go,om,m
      External Temperature
      common /cm4/ Ro,To,go,om,m
C
      T=Temperature(R)
C
      term1=DLog(T*Ro/(To*R))*m
      term1=term1/((To-m*Ro)*(To-m*Ro))
C
```

```
      term2=(R-Ro)/(R*Ro)
      term2=term2/(To-m*Ro)
C
      zgravit=To*Ro*Ro*(term1+term2)
C
      Return
      End
C
C ***********************************************************************
C  Function Dzcent :  This function is the derivative of the centrifugal
C    force term of the temperature modified geopotential height.  This
C    is needed because the centrifugal terms must be found be integrating
C    along the field line.
C ***********************************************************************
      Real*8 Function Dzcent(theta,thetao)
      Real*8 theta,thetao
      Real*8 temp,R
      Real*8 T,Temperature
      Real*8 Ro,To,go,om,m

      External Temperature
      Common /cm4/ Ro,To,go,om,m
C
      R=DCos(theta)*DCos(theta)*Ro/(DCos(thetao)*DCos(thetao))
      T=Temperature(R)
C
      temp=-3.0D0*To*om*om*Ro*Ro
      temp=temp*DSin(theta)*DCos(theta)*DCos(theta)*DCos(theta)
      temp=temp*DCos(theta)*DCos(theta)
      temp=temp/(DCos(thetao)*DCos(thetao)*DCos(thetao)*DCos(thetao))
      temp=temp/go
C
      Dzcent=temp/T
C
      Return
      End
C
C***********************************************************************
C  Subroutine Diffeq :  Determines density values for given R and theta.
C     Note that at the reference height of 500km, np=0.09neo, n0=0.84neo
C     and nHe=0.07*neo. The reference electron density is modified for
C     different latitudes by a formula from Thomson [1987].
C***********************************************************************
```

```
      Subroutine Diffeq(R,theta,ne,np,nHe,nO)
C
      Real*8 R,theta,ne,np,nHe,nO
      Real*8 neo,npo,nHeo,nOo
      Real*8 Hp,HO,HHe
      Real*8 RRo,h,T,thetao,reftheta
      Real*8 z,zg,zcent
      Real*8 temp,E,a
      Real*8 Me,Mp,MHe,MO,MO2,MNO
      Real*8 Pi,Eps,QQ,k,c,Re
      Real*8 Ro,To,go,om,m
      Real*8 zgravit,zcentrif,Dzcent,Temperature
      Real*8 Enh,W,L,Lo,f
      External zgravit,zcentrif,Dzcent,Temperature
      common /cm2/ Me,Mp,MHe,MO,MO2,MNO
      Common /cm3/ Pi,Eps,QQ,k,c,Re
      Common /cm4/ Ro,To,go,om,m
C
      thetao=Ro*DCos(theta)*DCos(theta)/R  ! Reference latitude for
      thetao=DACos(DSqrt(thetao))          ! determining temperature modified
C                                          ! geopotential height.
      E=0.5D0          ! Enhancement factor.
      reftheta=0.35D0  ! Reference latitude for latitudonal elec. dens. grad.
      neo=1.1D11       !  Reference electron density.
      neo=neo*(1.0D0+E*DCos(1.5708D0*theta/reftheta)) !  modified reference
C                                                     !  electron density.
      npo=0.09D0*neo      !  reference proton density
      nHeo=0.07D0*neo     !  reference helium density
      nOo=(1.0D0-nHeo/neo-npo/neo)*neo    !  reference oxygen density
      Hp=k*To/(Mp*go)     !  proton scale height
      HO=k*To/(MO*go)     !  oxygen scale height
      HHe=k*To/(MHe*go)   !  helium scale height
C
      RRo = R/Ro
      T=Temperature(R)
      h=R-Re
C
      Call Qtrap(Dzcent,thetao,thetao,theta,zcent)!  Determines cent. term.
      zg=zgravit(R)                !   Determines gravitational force term.
      z=zg-zcent         !  Total temperature modified geopotential height.
      temp=npo*To*DExp(-z/Hp)+nOo*To*DExp(-z/HO)+nHeo*To*DExp(-z/HHe)
      ne=1.0D0/T*DSqrt(neo*To*(temp))
      np=1.0D0/(T*T)*neo*To*npo*To*DExp(-z/Hp)/ne
```

```
      nHe=1.0D0/(T*T)*neo*To*nHeo*To*DExp(-z/HHe)/ne
      nO=1.0D0/(T*T)*neo*To*nOo*To*DExp(-z/HO)/ne
C
      Return
      End
C
C ***********************************************************************
C  Subroutine Refind: Determines the refractive index given the
C   wave normal angle and frequency.
C ***********************************************************************
C
      Subroutine Refind(omega,psi,mu,DmuBDpsi,DmuBDw)
      Real*8 omega,psi,mu,DmuBDpsi,DmuBDw
      Real*8 Ri,Li,Pi,Si,Di,Bi,Fi,Ai
      Real*8 niplus,niminus,polplus,polminus
      Real*8 F0e,F0p,F0He,F00,Fhe,Fhp,FhHe,Fh0
      Common /cm1/ F0e,F0p,F0He,F00,Fhe,Fhp,FhHe,Fh0
C
      Ri = 1.0D0 - F0e*F0e/(omega*(omega - Fhe)) -
     *     F0p*F0p/(omega*(omega + Fhp)) -
     *     F00*F00/(omega*(omega + Fh0)) -
     *     F0He*F0He/(omega*(omega + FhHe))
      Li = 1.0D0 - F0e*F0e/(omega*(omega + Fhe)) -
     *     F0p*F0p/(omega*(omega - Fhp)) -
     *     F00*F00/(omega*(omega - Fh0)) -
     *     F0He*F0He/(omega*(omega - FhHe))
      Pi = 1.0D0 - F0e*F0e/(omega*omega) - F0p*F0p/(omega*omega) -
     *     F00*F00/(omega*omega) - F0He*F0He/(omega*omega)
      Si = 0.5D0*(Ri + Li)
      Di = 0.5D0*(Ri - Li)
      Bi = Ri*Li*DSin(psi)*DSin(psi)+Pi*Si*(1.0D0+DCos(psi)*DCos(psi))
      Fi = (Ri*Li - Pi*Si)*(Ri*Li - Pi*Si)*DSin(psi)*DSin(psi)*
     *     DSin(psi)*DSin(psi) + 4.0D0*Pi*Pi*Di*Di*DCos(psi)*DCos(psi)
      Fi = DSqrt(Fi)
      If (Fi .LT. 0.0D0) Then
        Fi = -1.0D0*Fi
      End If
      Ai = Si*DSin(psi)*DSin(psi) + Pi*DCos(psi)*DCos(psi)
C
      niplus = (Bi + Fi)/(2.0D0*Ai)
      niminus = (Bi - Fi)/(2.0D0*Ai)
      polplus = Di/(niplus - Si)
      polminus = Di/(niminus - Si)
```

```
      If (polplus .GT. 0.0D0) Then
        If (niplus .GT. 0.0D0) Then
          mu = DSqrt(niplus)
        Else
          mu = 0.0D0
        End If
      End If
      If (polminus .GT. 0.0D0) Then
        If (niminus .GT. 0.0D0) Then
          mu = DSqrt(niminus)
        Else
          mu = 0.0D0
        End If
        Fi=-1.0D0*Fi
      End If
      If (polplus .LT. 0.0D0) Then
        If (polminus .LT. 0.0D0) Then
          mu = 0.0D0
        End If
      End If
      If (mu .NE. 0.0D0) Then
         Call Diffpsi(omega,psi,mu,DmuBDpsi,Si,
     *             Ri,Li,Pi,Fi,Di,Ai,Bi)
         Call DiffW(omega,psi,mu,DmuBDw,Si,
     *             Ri,Li,Pi,Fi,Di,Ai,Bi)
      End If
C
      Return
      End
C
C***********************************************************************
C  Subroutine Diffpsi: Determines the derivative of the phase refractive
C    index w.r.t the wave normal angle.
C***********************************************************************
C
      Subroutine Diffpsi(omega,psi,mu,DmuBDpsi,Si,
     *                   Ri,Li,Pi,Fi,Di,Ai,Bi)
      Real*8 omega,psi,mu,DmuBDpsi,Si,Ri,Li,Pi,Fi,Di,Ai,Bi
      Real*8 DABDpsi,DFBDpsi,DBBDpsi
C
      DABDpsi = 2.0D0*Si*DSin(psi)*DCos(psi) -
     *          2.0D0*Pi*DCos(psi)*DSin(psi)
      DFBDpsi = 1.0D0/(2.0D0*Fi)*((Ri*Li-Pi*Si)*(Ri*Li-Pi*Si)*
```

```
     *          4.0D0*DSin(psi)*DSin(psi)*DSin(psi)*DCos(psi)-
     *          8.0D0*Pi*Pi*Di*Di*DCos(psi)*DSin(psi))
      DBBDpsi = 2.0D0*Ri*Li*DSin(psi)*DCos(psi) -
     *           2.0D0*Pi*Si*DCos(psi)*DSin(psi)
      DmuBDpsi = -1.0D0/(2.0D0*mu)*((Bi + Fi)/(2.0D0*Ai*Ai)*
     *            DABDpsi - 1.0D0/(2.0D0*Ai)*(DBBDpsi + DFBDpsi))
      Return
      End
C
C ***************************************************************
C  Subroutine DiffW: Determines the derivative of the phase refractive
C    index w.r.t. frequency.
C ***************************************************************
C
      Subroutine DiffW(omega,psi,mu,DmuBDw,Si,
     *                 Ri,Li,Pi,Fi,Di,Ai,Bi)
      Real*8 omega,psi,mu,DmuBDw,Si,Ri,Li,Pi,Fi,Di,Ai,Bi
      Real*8 F0e,F0p,F0He,F00,Fhe,Fhp,FhHe,Fh0
      Real*8 DRBDw,DLBDw,DPBDw,DSBDw,DDBDw,DABDw,DFBDw,DBBDw
      Common /cm1/ F0e,F0p,F0He,F00,Fhe,Fhp,FhHe,Fh0
C
      DRBDw = (2.0D0*F0e*F0e*omega - F0e*F0e*Fhe)/
     *        (omega*omega*(omega - Fhe)*(omega - Fhe)) +
     *        (2.0D0*F0p*F0p*omega + F0p*F0p*Fhp)/
     *        (omega*omega*(omega + Fhp)*(omega + Fhp)) +
     *        (2.0D0*F00*F00*omega + F00*F00*Fh0)/
     *        (omega*omega*(omega + Fh0)*(omega + Fh0)) +
     *        (2.0D0*F0He*F0He*omega + F0He*F0He*FhHe)/
     *        (omega*omega*(omega + FhHe)*(omega + FhHe))
      DLBDw = (2.0D0*F0e*F0e*omega + F0e*F0e*Fhe)/
     *        (omega*omega*(omega + Fhe)*(omega + Fhe)) +
     *        (2.0D0*F0p*F0p*omega - F0p*F0p*Fhp)/
     *        (omega*omega*(omega - Fhp)*(omega - Fhp)) +
     *        (2.0D0*F00*F00*omega - F00*F00*Fh0)/
     *        (omega*omega*(omega - Fh0)*(omega - Fh0)) +
     *        (2.0D0*F0He*F0He*omega - F0He*F0He*FhHe)/
     *        (omega*omega*(omega - FhHe)*(omega - FhHe))
      DPBDw = 2.0D0*(F0e*F0e/(omega*omega*omega)) +
     *        2.0D0*(F0p*F0p/(omega*omega*omega)) +
     *        2.0D0*(F00*F00/(omega*omega*omega)) +
     *        2.0D0*(F0He*F0He/(omega*omega*omega))
      DSBDw = 0.5D0*(DRBDw + DLBDw)
      DDBDw = 0.5D0*(DRBDw - DLBDw)
```

```
      DABDw = DSBDw*DSin(psi)*DSin(psi) +
     *        DPBDw*DCos(psi)*DCos(psi)
      DFBDw = 1.0D0/(2.0D0*Fi)*(2.0D0*(Ri*Li - Pi*Si)*
     *        DSin(psi)*DSin(psi)*DSin(psi)*DSin(psi)*
     *        (Ri*DLBDw + Li*DRBDw - Pi*DSBDw - Si*DPBDw) +
     *        8.0D0*Pi*Di*DCos(psi)*DCos(psi)*(Pi*DDBDw + Di*DPBDw))
      DBBDw = Ri*DLBDw*DSin(psi)*DSin(psi) + Li*DRBDw*DSin(psi)*
     *         DSin(psi) + Pi*DSBDw*(1.0 + DCos(psi)*DCos(psi)) +
     *         Si*DPBDw*(1.0D0+DCos(psi)*DCos(psi))
      DmuBDw = -1.0D0/(2.0D0*mu)*((Bi + Fi)/(2.0D0*Ai*Ai)*DABDw -
     *          1.0D0/(2.0D0*Ai)*(DBBDw + DFBDw))
C
      Return
      End
C
C*********************************************************************
C  Subroutine Magfield :  Determines the magnetic field strength at
C     r,theta using a dipole field model.
C*********************************************************************
      Subroutine Magfield(R,theta,B)
      Real*8 R,Re,B,theta
C
      Re = 6371200.0D0
      B = 3.0696381D-5*Re*Re*Re/(R*R*R)*DSqrt(1.0D0 +
     *    3.0D0*DSin(theta)*DSin(theta))
C
      Return
      End
C
C*********************************************************************
C  Subroutine RKG(Y,N,H,DyBDx,Q):  Gill modification of Runge
C   Kutta routine.  Y is an array of N elements representing the
C   dependent variables.  The routine advances a set of equations
C   by one step.  F is an N-element in which each element is equal to a
C   first order differential equation.  In this case F contains the
C   ray tracing equations. Q is a N-element  array carrying error
C   information.  It must be set to zero on first entry and left
C   undisturbed thereafter.
C*********************************************************************
C
      Subroutine RKG(Y,N,DyBDx,H,Q,omega)
      Real*8 omega,Y,F,H,Q,A,B,C,D,E
      Integer I,J,N
```

```
      Dimension Y(4),F(4),Q(4)
      External DyBDx
C
21    Do 28 J=1,4
      Call DyBDx(Y,F,omega)
      Do 28 I=1,N
      A=Y(I)
      B=H*F(I)
      C=Q(I)
      Go to (22,23,25,26),J
22    D=0.5D0
      E=D*B-C
      Go to 27
23    D=0.292893219D0
C     Const is 1-1/Sqrt(2) to digital accuracy of machine
24    E=D*(B-C)
      Go to 27
25    D=1.70710678D0
C     Const is 1+1/Sqrt(2) to digital accuracy of machine
      Go to 24
26    D=0.5D0
      E=0.166666667D0*(B-C-C)
C     Const is 1/6 to digital accuracy of machine
27    Y(I)=A+E
28    Q(I)=3.0D0*E-D*B+C
      Return
      End
C
C *********************************************************************
C  The next two subroutines integrate a given function between two limits.
C *********************************************************************
      Subroutine Qtrap(Func,theta,A,B,S)
      Real*8 Func,theta,A,B,S
      Real*8 OldS,Epsil
      External Func
      Integer J,Jmax
      Parameter (Epsil=1.0D-1, Jmax=20)
      OldS=-1.0D30
      DO 11 J=1,Jmax
        Call Trapzd(Func,theta,A,B,S,J)
        IF (DABS(S-OldS).LE.Epsil*DABS(OldS)) Return
        OldS=S
11    Continue
```

```
      Pause 'Too many steps.'
      Return
      End
C
C*********************************************************************
C  Trapezoidal integration
C*********************************************************************
      Subroutine Trapzd(Func,theta,A,B,S,N)
      Real*8 Func,theta,A,B,S
      Real*8 Del,TNM,X,Sum
      External Func
      Integer J,IT
      Integer N
      If (N.EQ.1) Then
        S=0.5D0*(B-A)*(Func(A,theta)+Func(B,theta))
        IT=1
      Else
        TNM=IT
        Del=(B-A)/TNM
        X=A+0.5D0*Del
        Sum=0.0D0
        Do 11 J=1,IT
          Sum=Sum+Func(X,theta)
          X=X+Del
11      Continue
        S=0.5D0*(S+(B-A)*Sum/TNM)
        IT=2*IT
      ENDIF
      RETURN
      END
C
C*********************************************************************
C  Function Zbrent:  Determines the root of a function.
C*********************************************************************
      Real*8 Function ZBRENT(Func,ni,DniBDr,Hi,temp,X1,X2,Tol)
      Real*8 Func,ni,DniBDr,Hi,temp,X1,X2,Tol
      Real*8 Tol1,Eps,ITmax,Iter,P,XM,S,R,Q
      Real*8 A,B,C,D,E,FA,FB,FC
      External Func
      PARAMETER (ITmax=100,Eps=3.0D-12)
      A=X1
      B=X2
      FA=Func(A,ni,DniBDr,Hi,temp)
```

```
FB=Func(B,ni,DniBDr,Hi,temp)
If (FB*FA .GT. 0.0D0) PAUSE 'Root must be bracketed for ZBRENT.'
FC=FB
Do 11 Iter=1,ITmax
  If (FB*FC.GT.0.0D0) Then
    C=A
    FC=FA
    D=B-A
    E=D
  EndIf
  If (DABS(FC).LT.DABS(FB)) Then
    A=B
    B=C
    C=A
    FA=FB
    FB=FC
    FC=FA
  EndIf
  Tol1=2.0D0*Eps*DABS(B)+0.5D0*Tol
  XM=0.5D0*(C-B)
  If (DABS(XM).LE.Tol1 .OR. FB.EQ.0.0D0) Then
    ZBRENT=B
    Return
  EndIf
  If (DABS(E).GE.Tol1 .AND. DABS(FA).GT.DABS(FB)) Then
    S=FB/FA
    If (A.EQ.C) Then
      P=2.0D0*XM*S
      Q=1.0D0-S
    Else
      Q=FA/FC
      R=FB/FC
      P=S*(2.0D0*XM*Q*(Q-R)-(B-A)*(R-1.0D0))
      Q=(Q-1.0D0)*(R-1.0D0)*(S-1.0D0)
    EndIf
    If (P .GT. 0.0D0) Q=-Q
    P=DABS(P)
    If (2.0D0*P .LT. MIN(3.0D0*XM*Q-DABS(TOL1*Q),DABS(E*Q))) Then
      E=D
      D=P/Q
    Else
      D=XM
      E=D
```

```
          EndIf
        Else
          D=XM
          E=D
        EndIf
        A=B
        FA=FB
        If (DABS(D) .GT. Tol1) Then
          B=B+D
        Else
          B=B+SIGN(TOL1,XM)
        EndIf
        FB=func(B,ni,DniBDr,Hi,temp)
11    Continue
      PAUSE 'ZBRENT exceeding maximum iterations.'
      ZBRENT=B
      Return
      End
C*********************************************************************
```

Bibliography

Andrews, M.K., Non-ducted whistler mode signals at low latitudes, *J. Atmos. Terrs. Phys.*, **42**, 1-20, 1978

Angerami, J.J. and Thomas, J.O., Studies of planetary atmospheres, *J. Geophys. Res.*, **69**, 4537-4559, 1964.

Armstrong, W.C., Lightning triggered from the earth's magnetosphere as the source of synchronised whistlers, *Nature*, **327**, 405-408, 1987.

Barkhausen, H., Zwei mit hilfe der neuen verstarker entdeckte erscheinungen, *Physik. Z.*, **20**, 401-403, 1919.

Bernard, L.C., A new nose extension method for whistlers, *J. Atmos. Terrs. Phys.*, **35**, 871-880, 1973.

Bernhardt, P.A. and Park, C.G., Protonospheric-ionospheric modelling of VLF ducts, *J. Geophys. Res.*, **82**, 5222-5230, 1977.

Budden, K.G., *Radio Waves in the Ionosphere*, Cambridge University Press, 1961.

Budden, K.G., *The Propagation of Radio Waves*, Cambridge University Press, 1985.

Carpenter, D.L., Whistler evidence of a "knee" in the magnetospheric ionisation density profile, *J. Geophys. Res.*, **68**, 1675-1682, 1963.

Carpenter, D.L., Stone, K., Siren J.C. and Crystal, T.L., Magnetospheric electric fields deduced from drifting whistler paths, *J. Geophys. Res.*, **77**, 2819-2834, 1972.

Carpenter, D.L., Inan, U.S., Trimpi, M.L., Helliwell, R.A. and Katsufrakis, J.P., Perturbations of subionospheric LF and MF signals due to whistler-induced electron precipitation bursts, *J. Geophys. Res.*, **89**, A11, 705-708, 1984.

Cerisier, J.C., A theoretical and experimental study of non-ducted VLF waves after propagation through the magnetosphere, *J. Atmos. Terrs. Phys.*, **35**, 77-94, 1973.

Dowden, R.L. and Adams, C.D.D., Phase and amplitude perturbations on sub-ionospheric signals explained as echoes from lightning induced electron precipitation ionisation patches, *J. Geophys. Res.*, **93**, 11543-11550, 1988.

Dowden, R.L. and Adams, C.D.D., Size and location of lightning-induced ionisation enhancements from measurement of VLF phase and amplitude perturbations on multiple antennas, *J. Atmos. Terrs. Phys.*, **55**, 1335-1359, 1993.

Dowden, R.L., Brundell, J., Rodger, C., Mochanov, O., Lyons, W. and Nelson, T., The structure of red sprites determined by VLF scattering, *Antennas and Propagation*, **38**, 7-15, 1996a.

Dowden, R.L., Brundell, J.B., Lyons, W.A. and Nelson, T., Detection and location of red sprites by VLF scattering of sub-ionospheric transmissions, *Geophys. Res. Letts.*, **23**, 1737-1740, 1996b.

Dowden, R.L., Brundell, J.B. and Lyons, W.A., Are VLF rapid onset, rapid decay perturbations produced by scattering off sprite plasma?, *J. Geophys. Res.*, **101**, D14, 19175-19183, 1996c.

Eckersley, T.L., Musical Atmospherics, *Nature*, **135**, 104-105, 1935.

Friedel, R.H.W. and Hughes, A.R.W., Characteristics and frequency of occurrence of Trimpi events recorded during 1982 at SANAE, Antarctica, *J. Atmos. Terrs. Phys.*, **52**, 329-339, 1990.

Friedel, R.H.W., A Study of Wave Induced Electron Precipitation at Low and Middle Latitudes, Ph.D. Thesis submitted at University of Natal, Durban, 1991.

Gurnett, D.A., Shawhan, S.D., Brice, N.M. and Smith, R.L., Ion cyclotron whistlers, *J. Geophys. Res.*, **70**, 1665-1688 , 1965.

Hansen, H.J., Mravlag, E., Scourfield, M.W.J., Coupled 3- and 1.3-Hz components in auroral pulsations, *J. Geophys. Res.*, **93**, 10029-10034, 1988.

Hargreaves, J.K., *The Upper Atmosphere and Solar-Terrestrial Relations*, Van Nostrand Reinhold, 1978.

Haselgrove, J., Ray theory and a new method for ray tracing, *Report on the Conference on the Physics of the Ionosphere*, 355-364, Physical Society of London, London, 1954.

Hayakawa, M. and Iwai, A, Magnetospheric ducting of low-latitude whistlers as deduced from the rocket measurements of their wave normal directions, *J. Atmos. Terrs. Phys.*, **37**, 1211-1218, 1975.

Hayakawa, M. and Tanaka, Y., On the propagation of low-latitude whistlers, *Rev. Geophys. Space Phys.*, **16**, 111-123, 1978.

Hayakawa, M., Tanaka, Y. and Ohta, K., Further direction finding evidence on ducted propagation of low latitude daytime whistlers, *Res. Letts. Atmos. Electr.*, **5**, 35-46, 1985

Helliwell, R.A., The "nose" whistler - a new high latitude phenomena, *J. Geophys. Res.*, **61(1)**, 139-142, 1956.

Helliwell, R.A., *Whistlers and Related Ionospheric Phenomena*, Stanford University Press, 1965.

Helliwell, R.A., A theory of discrete VLF emissions from the magnetosphere, *J. Geophys. Res.*, **72**, 4773-4790, 1967.

Helliwell, R.A., Katsufrakis, J.P. and Trimpi, M.L., Whistler-induced amplitude perturbation in VLF propagation, *J. Geophys. Res.*, **78**, 4579-4688, 1973.

Hines, C.O., Heavy-ion effects in audio-frequency radio propagation, *J. Atmos. Terrs. Phys.*, **11**, 36-42, 1957.

Ho, D. and Bernard, L.C., A fast method to determine the nose frequency and minimum group delay of a whistler when the causative spheric is unknown, *J. Atmos. Terrs. Phys.*, **35**, 881-887, 1973.

Hughes, A.R.W., Satellite measurements of whistler dispersion at low latitudes, *Adv. Space Res.*, **1**, 377-380, 1981.

Hughes, A.R.W. and Rice, W.K., A satellite study of low latitude electron and proton whistlers, *J. Atmos. Sol. Terrs. Phys.*, **59**, 1217-1222, 1997.

Inan, U.S. and Carpenter, D.L., Lightning-induced electron precipitation events observed at $L = 2.4$ as phase and amplitude perturbations on subionospheric VLF signals, *J. Geophys. Res.*, **92**, 3293-3303, 1987.

Inan, U.S. and Bell, T.F., Pitch angle scattering of energetic particles by oblique whistler waves, *Geophys. Res. Letts.*, **18**, 49-52, 1991a.

Inan, U.S., Bell, T.F. and Rodriguez, J.V., Heating and ionisation of the lower ionosphere by lightning, *Geophys. Res. Letts.*, **18**, 705-708, 1991b.

Jones, D., Recent work on ion-cyclotron whistlers, *Ann. Geophys.*, **28**, 527-540, 1972.

Kennel, C.F. and Petschek, H.E., Limit on stably trapped particle fluxes, *J. Geophys. Res.*, **71**, 1-28, 1972.

Kimura, I., Effect of ions on whistler-mode ray tracing, *Radio Science*, **1**, 269-283, 1966.

Kimura, I., Whistler mode propagation in the earth and planetary magnetospheres and ray tracing techniques, *Space Sci. Revs.*, **42**, 449-466, 1985.

Liemohn, H.B., Cyclotron resonance amplification of VLF and ULF whistlers, *J. Geophys. Res.*, **32**, 39-55, 1967.

Lohrey, B. and Kaiser, A.B., Whistler induced anomalies in VLF propagation, *J. Geophys. Res.*, **84**, 5211-5130, 1979.

Lyons, L.R. and Williams, D.J., *Quantitative Aspects of Magnetospheric Physics,* D. Reidel Publishing Company, 1984.

Lyons, W.A., Sprite observations above the U.S. High Plains in relation to their parent thunderstorm systems, *J. Geophys. Res.*, (in press), 1996.

Ondoh, T., Kotaki, M., Murakami, T., Watanabe, S. and Nakamura, Y., Propagation characteristics of low latitude whistlers, *J. Geophys. Res.*, **84**, 2099-2104, 1979.

Park, C.G., Methods of Determining Electron Concentrations in the Magnetosphere from Nose Whistlers, *Tech. Rep. 3454-1 Radio Science Lab.*, Radio-Science labs., Stanford University, 1972.

Poeverlein, H., Strahlwege von radiowellen in der ionosphare, *Sitz. Bayerischen Akad. Wiss.*, **1**, 175-201, 1948.

Preece, W.H., Earth currents, *Nature*, **49**(1276), 554, 1894.

Press, W.H., Flannery, B.P., Teukolsky, S.A. and Vetterling, W.T., *Numerical Recipes - The Art of Scientific Computing*, Cambridge University Press, Cambridge, United Kingdom, 1st edition, 1986.

Roederer, J.G., *Dynamics of Geomagnetically Trapped Radiation*, Springer-Verlag, 55-56, 1970.

Sagredo, J.L., Smith, I.L. and Bullough, K., The determination of whistler nose-frequency and minimum group delay and its implication for the measurement of east-west electric field and tube content in the magnetosphere, *J. Atmos. Terrs. Phys.*, **35**, 2035-2046, 1973.

Singh, B. and Tantry, B.A.P., On ducting of whistlers at low latitudes, *Ann. Geophys.*, **29**, 561-568, 1973.

Smith, R.L., Propagation characteristics of whistlers trapped in field-aligned columns of enhanced ionisation, *J. Geophys. Res.*, **66(11)**, 3699-3707, 1961.

Smith, R.L. and Angerami, J.J., Magnetospheric properties deduced from OGO-1 observations of ducted and non-ducted whistlers, *J. Geophys. Res.*, **73**, 1, 1968.

Sonwalker, V.S., Bell, T.F., Helliwell, R.A. and Inan, U.S., Direct multiple path magnetospheric propagation: a fundamental property of non-ducted waves, *J. Geophys. Res.*, **89**, 2823-2830, 1984.

Stix, T.H., *The Theory of Plasma Waves*, McGraw Hill Book Co., New York, 1962.

Stix, T.H., *Waves in Plasmas*, American Institute of Physics, New York, 1992.

Storey, L.R.O., An investigation of whistling atmospherics, Phil. Trans. Roy. Soc. (London), **A**, **246**, 113-141, 1953.

Strangeways, H., Trapping of whistler-mode waves in ducts with tapered ends, *J. Atmos. Terrs. Phys.*, **43**, 1071-1079, 1981.

Stringfellow, M.F., Lightning incidence in Britain and the solar cycle, *Nature*, **249**, 332-333, 1974.

Tanaka, Y. and Hayakawa, M., The effect of geomagnetic disturbances on duct propagation of low latitude whistlers, *J. Atmos. Terrs. Phys.*, **35**, 1699-1703, 1973.

Tanaka, Y. and Cairo, L., Propagation of VLF waves through the equatorial anomaly, *Ann. Geophys.*, **36**, 555-575, 1980.

Tanaka, Y. and Hayakawa, M., On the propagation of daytime whistlers at low latitudes, *J. Geophys. Res.*, **90**, 3457-3464, 1985.

Thomson, R.J. and Dowden, R.L., Simultaneous ground and satellite reception of whistlers-2. PL whistlers, *J. Atmos. Terrs. Phys.*, **39**, 879-890, 1977.

Thomson, N.R., Whistler mode signals, spectrographic group delays, *J. Geophys. Res.*, **86**, 4795-4802, 1981.

Thomson, N.R., Ray-tracing the paths of very low latitude whistler-mode signals, *J. Atmos. Terr. Phys.*, **49**, 321-338, 1987.

Tolstoy, A., Rosenberg, T.J., Inan, U.S. and Carpenter, D.L., Model predictions of subionospheric VLF signal perturbations resulting from localised electron precipitation-induced enhancement regions, *J. Geophys. Res.*, **91**, 13437-13482, 1986.

Tsuruda, K., Penetration and reflection of VLF waves through the ionosphere: Full wave calculations with ground effect, *J. Atmos. Terrs. Phys.*, **35**, 1377-1405, 1972.

Van Allen, J.A., The geomagnetically trapped corpuscular radiation, *J. Geophys. Res.*, **64**, 1683-1689, 1959.

Yabroff, I., Computation of whistler ray paths, *J. Res. NBS*, **65D**(5), 485-505, 1961.